The journey from structure to function: multiscale mechanical models and experiments reveal how collagen organization influences passive muscle mechanics

---

A
Dissertation
Presented to
the faculty of the School of Engineering and Applied Science
University of Virginia

---

in partial fulfillment
of the requirements for the degree

Doctor of Philosophy

by

Ridhi Sahani

December 2023

APPROVAL SHEET

This

Dissertation

is submitted in partial fulfillment of the requirements
for the degree of

Doctor of Philosophy

Author: Ridhi Sahani

This Dissertation has been read and approved by the examing committee:

Advisor: Silvia Blemker

Advisor:

Committee Member: Shayn Pierce-Cottler

Committee Member: Rebecca Scharf

Committee Member: Douglas DeSimone

Committee Member: Thomas Barker

Committee Member:

Committee Member:

Accepted for the School of Engineering and Applied Science:

Jennifer L. West, School of Engineering and Applied Science

December 2023

The journey from structure to function: multiscale mechanical models and experiments reveal how collagen organization influences passive muscle mechanics

By Ridhi Sahani

Acknowledgements

This thesis tells the story of my research over the past five years, focusing on a journey from structure to function. This journey, nor my personal one, would have been possible without my incredible support system.

Firstly, I must thank my amazing Ph.D. advisor and mentor, Silvia. I still remember our first meeting during BME graduate recruitment. I was immediately in awe of your exciting and innovative research, approach to science, and commitment to mentoring. While I knew that the M3 lab would be a good fit, I couldn't have imagined what a perfect home it would be. Thank you for your consistent positivity and encouragement, even when models don't converge and experiments fail. Research certainly has its ups and downs, but I have learned that "*embracing confusing and unexpected results with delight and intense curiosity*" leads to the most exciting and rewarding science. I can't imagine a better person to have learned from, not just about muscle mechanics, but how to stay true to who you are and maintain the fun while doing hard science. You have been an incredible role "*model,*" and I would not have the confidence or be the person I am today without all your support!

I must also thank my Ph.D. committee for all their advice and support. Shayn, thank you for being my committee chair and for your dedication to students as graduate program director and now the chair of BME! I am also grateful for the opportunity to learn from you in the BME grad core courses and for your support during the SEAS teaching fellowship. Dr. Scharf, the opportunity to shadow you in the Neuromuscular Clinic during my first year was instrumental to the development of my project and I have continued to be inspired by your dedication to helping others. Tom and Doug, thank you for all your valuable insights on the ECM. Your input has strengthened my thesis work and my understanding and appreciation of the ECM.

To the M3 lab, you have truly been a family these last few years and I feel lucky to have a place that is so hard to leave. To the M3 alum that welcomed me when I joined the lab, thank you for guiding me through research and grad school. Katie P, I feel like I was able to learn so much about navigating grad school from you, even though we were only in the lab together for a short while. Adrienne, thanks for your positive attitude and for always having an encouraging word to say. Brian, thanks for all your guidance on so many things, from experiments to modeling. Katie K, thank you for all your advice on career paths, fun chats about muscle (and Taylor Swift), and continually being a great role model. Hunter, thanks for all your mentoring through experiments (and pretending we were sending the mice to Disney Land). Vi, thank you for being my lab big sis and one of the kindest (and sassiest) humans I have ever met. I could not imagine grad school without you and am so thankful for our friendship.

To the current M3 lab, I can't thank you enough for all the support, laughs, and memories. I will miss all the coffee walks, lab dinners, and dominating the BME department competitions (sometimes). Matt, it's been so great to go through the grad school process together, and thanks for keeping my mint addiction in check. Xiao, I am so glad we were able to co-teach biomechanics and thank you for your guidance during that process. Emily, thanks for all your mentoring in the lab and advice about the postdoc process (and introducing me to stress toys). Kaitlyn, thanks for being such a rockstar undergrad and for all your hard work. I can't wait to see your exciting next steps! Mario, I'm so glad you joined our lab (even though you kept us guessing) and I will miss the scary movie nights and coffee chats. Megan, I'll never forget our mice sacs and fun memories in and out of lab. Thanks for always being there to listen, no matter how busy you are. To Allie, thanks for being the TA2 to TA1, my cubicle buddy, and partner in crime. I don't know what I would have done without you to talk through science and life with these last few years.

My experience at UVA and in C'ville wouldn't have been the same without so many other incredible people. To the BME department, you have been such a special community, and I feel so grateful for all the memories in and out of MR5. To the "2018 till defense do us part" cohort, thanks for all the game nights, happy hours, HSL study sessions, and other fun adventures. I'll miss you all so much! Mara, I'm so thankful for all our memories, from quarantine walks to writing nights and everything in between. Amy, thanks for being so genuinely kind, positive, and supportive. To the Cumulus dance group, I have loved being a part of this community and am so thankful for all the classes, performances, and memories.

I also must thank my support system outside of C'ville. To the herd - Alli, Lindsey, Emily, and Lauren, I wouldn't have made it to grad school without our late nights in the lib, milkshakes from seventh street, and various other adventures at Bucknell. To Catherine, Steph, and Libby, thanks for all the amazing memories in Tustin and beyond and for continually being so encouraging. I also must thank my undergrad Professors at Bucknell. Dr. K, thank you for being such a great research advisor and introducing me to biomechanics research. To Kelly, thank you for being so incredibly supportive and committed to all your students. I am so grateful to have had so many positive mentors.

Finally, I must thank my amazing family. To my grandparents, Dadima, Dadaji, Nanu, and Nanaji, your lives and legacies continue to inspire me to be a better person and make an impact in this world. While you may not be here today, I hope that you would be proud. To my extended family, Mohit Mamu, Leslie Aunty, Shaanti and Raj, thank you for your consistent support and I am so thankful for all of our memories.

To my sister, Shadhi, thank you for being my best friend and role model. I will always look up to you and am so lucky that I was able to learn about how to go through grad school from you. Thank you for always listening to me, calming me down, and believing in me. To my parents, Mama and Baba, none of this would be possible without you. From moving halfway across the world with us, to making sure we had access to every opportunity, I can't thank you enough. You have always believed in me and encouraged me to be myself and I wouldn't be where I am today without you. I love you all so much and would not be the scientist or person I am without you!

No one can take your education away.

—Balraj Trikha

Abstract

The skeletal muscle extracellular matrix (ECM) is a beautiful and complex three-dimensional scaffold that transmits physical and chemical signals and regulates passive muscle properties. Collagen fibers determine the ECMs' structural and tensile properties and have unique arrangements surrounding (epimuscular) and within (intramuscular) muscle. An accumulation of collagen is often used to characterize the development of fibrosis in neuromuscular disorders such as Duchenne muscular dystrophy (DMD); however, increased collagen levels do not explain alterations in passive muscle properties, such as increased stiffness, that contribute to muscle dysfunction. Thus, we must consider how collagen organization influences passive muscle mechanics, especially in complex muscles such as the diaphragm, which is severely affected in DMD.

My thesis couples imaging, mechanical testing, and multiscale finite element modeling to examine the role of collagen microstructure on macroscopic muscle tissue properties. First, I characterized collagen organization in the epimuscular ECM of diaphragm muscle and found that collagen fibers were oriented perpendicular to muscle fibers (cross-muscle fiber direction), with greater collagen fiber alignment in *mdx* (dystrophin null) relative to WT mice. I then developed epimuscular micromechanical models to determine the mechanical implications of changes in collagen structure on ECM properties and predicted higher cross-muscle fiber stiffness in the *mdx* compared with WT models. Next, I developed micromechanical models of both epimuscular and intramuscular regions and coupled their predictions to determine bulk muscle tissue properties. I then performed biaxial mechanical tests to characterize along- and cross-muscle fiber tissue properties in *mdx* and WT diaphragm muscle to directly calibrate and validate the models. We predicted higher cross-muscle fiber collagen alignment and stiffness in the *mdx* compared with WT models, with nonuniform stresses between ECM and muscle regions. Further, collagen fiber distribution had a much more substantial impact on tissue stiffness than ECM area fraction. Taken together, we show that the primary orientation of collagen fibers relative to muscle fibers explains anisotropic tissue properties observed in diaphragm muscle, and that the distribution of collagen fibers explains discrepancies between measurements of collagen amounts and tissue stiffness. This work provides novel insights into collagen's complex role on passive muscle mechanics and highlights the capability of mechanical modeling to fill gaps along the journey from structure to function.

Table of Contents

List of Tables

List of Equations

List of Figures

"If there's a book that you want to read,
but it hasn't been written yet,
then you must write it."

—Toni Morrison

Chapter 1 : Introduction

Duchenne muscular dystrophy (DMD) is a fatal x-linked genetic disorder affecting 1 in 3500 males, with no cure or effective treatment to date.[1] A lack in expression of dystrophin at the muscle fiber membrane increases susceptibility to mechanical stress from everyday muscle contractions and triggers a chronic state of inflammation.[2–6] Excessive accumulation of extracellular matrix (ECM) components leads to buildup of fibrotic tissue along with increased muscle stiffness, and muscle degeneration that progresses with age. Diminished pulmonary function contributes to respiratory insufficiency, a leading cause of death in DMD.[7] Mechanical ventilation (MV) prolongs survival[8] but further weakens the diaphragm muscle[9] and there is variability in the type and timing of ventilatory support prescribed.[10,11] Atrophy has been a large focus of the field and limits contractile properties, but the role of fibrosis on diaphragm function is less understood.

The skeletal muscle ECM has a complex 3-D structure with collagen fibers organized uniquely between the epimuscular and intramuscular ECM layers. *Mdx* mouse diaphragm reproduces degeneration seen in DMD patients, with impairment in respiratory function and fibrosis,[12,13] but collagen amount and tissue stiffness do not correlate,[14] highlighting the need to investigate changes in ECM structure. Multiscale models provide a unique opportunity to predict how variations in microstructure influence macroscopic tissue properties. Micromechanical finite-element models study the role of muscle-fascicle microstructure on tissue-level properties.[15,16] Previous 2-D models of *mdx* lower limb muscle highlighted the importance of ECM mechanics on muscle regeneration, revealing that increased ECM stiffness was not explained by total amount of collagen alone.[17] Thus, we must consider the role of fibrotic tissue structure and mechanics on diaphragm function and disease progression.

In chapter three, I focused on the role of collagen organization on ECM level tissue properties. The goals of this study were to (1) determine if and how collagen organization changes with the progression of DMD in diaphragm muscle tissue, and (2) predict how collagen organization influences the mechanical properties of the ECM. I first visualized collagen structure with scanning electron microscopy (SEM) images and then developed an analysis framework to quantify collagen organization and generate image-based finite-element models. The image analysis revealed increased collagen fiber straightness and alignment in diseased relative to healthy mice and increased collagen fiber straightness in old relative to young healthy mice. Collagen fibers retained a transverse orientation relative to muscle fibers in all groups. All mechanical models predicted an increase in the transverse relative to longitudinal (muscle fiber direction) stiffness, with an increase in stiffness ratio (transverse/longitudinal) in diseased relative to healthy models. This study revealed changes in diaphragm ECM structure and mechanics during disease progression in the *mdx* muscular dystrophy mouse phenotype, highlighting the need to consider the role of collagen organization on diaphragm muscle function. Chapter three is published in the Journal of Applied Physiology (DOI:10.1152/japplphysiol.00248.2021) with co-authors ,C. Hunter Wallace, Brian K. Jones, and Silvia S. Blemker.

In chapter four, I focused on the role of collagen microstructure on bulk muscle tissue properties. The goals of this study were to (1) measure diaphragm muscle tissue structure and mechanical properties in *mdx* and WT mice, (2) develop, calibrate, and validate a modeling framework that relates the multiple layers of ECM microstructure to bulk muscle tissue properties, and (3) predict how changes in tissue microstructure contribute to impairments during disease. I first performed *in vitro* biaxial testing to characterize both along-muscle fiber and cross-muscle fiber tissue properties and collected *ex vivo* images to measure tissue microstructure. I then developed epimuscular and intramuscular micromechanical models to predict local tissue properties and then coupled their outputs to predict bulk tissue properties. This framework integrated experimental and finite element modeling techniques, providing an avenue to examine how microstructural variations account for measured differences in macroscopic tissue properties.

The models predicted that intramuscular collagen fibers aligned primarily in the cross-muscle fiber direction in both *mdx* and WT models, with greater cross-muscle fiber alignment required in the *mdx* models compared with WT. The models also predicted that the distribution of collagen fibers had a greater influence on passive tissue properties than the amount of ECM, explaining the variation across samples. Further, tissue stresses were more nonuniform during cross-muscle fiber loading and collagen organization explained the increased cross- relative to along-muscle fiber stiffness observed in diaphragm muscle. Chapter four is in preparation for submission to the Journal of the Royal Society Interface, with co-authors Kaitlyn Hixson, and Silvia S. Blemker.

Overall, my findings suggest that the distribution of collagen fibers has a greater influence on passive tissue properties than collagen amount, and that collagen reorganization, rather than accumulation may provide an effective target for therapeutics. By coupling experiments and mechanical models we highlighted gaps from predicting structure function relationships with experiments alone and provide a framework that can be applied to hypothesize new experiments and intervention targets.

Chapter 2 : Background

From walking to breathing, skeletal muscle is essential for daily movement. Skeletal muscles come in all shapes and sizes, with unique macroscopic muscle architectures related to distinct functional demands. While differences in three-dimensional muscle geometries are seen, the fundamental structure of skeletal muscle tissue remains conserved and is highly organized. Individual muscle fibers form muscle fascicles that group together into whole muscle, separated by layers of extracellular matrix (ECM). The sarcomere is the basic building block of skeletal muscle, where the formation of actin and myosin cross bridges generate active contractile forces. Force generation is dependent on muscle length, with the maximum active force occurring at optimal muscle fiber length, and passive forces often assumed to begin at optimal fiber length. Passive structures within muscle tissue, namely titin and the ECM, regulate non-contractile passive forces, with a transition from its toe to linear region occurring with their unkinking and straightening.

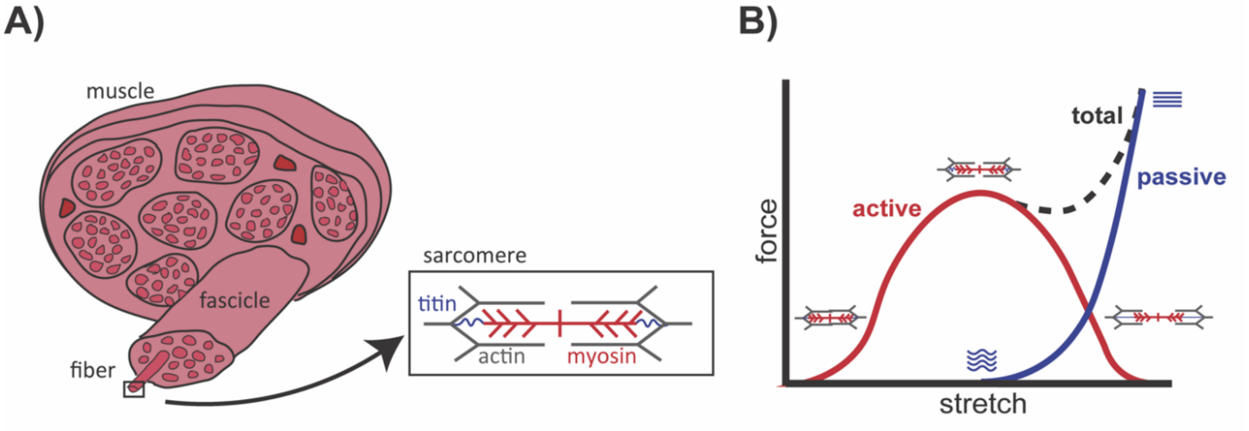

Figure 2.1 (A) Muscle hierarchy and (B) force length curve

The extracellular matrix is a key contributor to passive muscle properties. In skeletal muscle, the extracellular matrix (ECM) serves as a three-dimensional scaffold and is essential for transmitting both physical and chemical signals.[18–20] The ECM consists of fibrous proteins embedded in a ground matrix, where each component plays a unique role in force transmission. Proteoglycans (PGs) and glycosaminoglycans (GAGs) regulate the viscous properties of the ECM, while collagen is the key structural protein. Type I and III collagen fibers make up 75% of the total collagen amount in skeletal muscle. Type I collagen fibers are rod like with little flexibility and are responsible for regulating the tensile properties of the ECM. Type III collagen fibers are more loosely packed and form a "reticular" fiber network along with elastin fibers that is responsible for distributing stresses within the ECM.[21] The ECM's role in passive force generation is shown by indirect measurements, comparing properties of single muscle fibers and muscle fiber bundles with intact ECM.[22–24] However, such measurements do not account for the complex microstructure of collagen in the ECM.

Collagen is organized uniquely across ECM layers and muscle groups. The epimysium (epimuscular ECM) surrounds the outermost surface of skeletal muscle, while the perimysium and endomysium (intramuscular ECM) separate muscle fascicles and muscle fibers.[25–27] The orientation of collagen fibers relative to muscle fibers affects their ability to transmit force during muscle contractions[26] and unique collagen arrangements are seen between ECM layers and across muscle groups. The structure of the endomysium is observed to be similar across skeletal muscles,[28] with a helical arrangement surrounding muscle fibers (**Fig. 2.2C**). In the perimysium of skeletal muscles such as the biceps, gastrocnemius, and psoas major, large bundles of collagen fibers are seen arranged both parallel and circumferential to muscle fibers (**Fig. 2.2B**).[28] Differences in the structure of the epimysium are also reported across skeletal muscles. In long strap-like muscle, a cross-ply arrangement of wavy collagen fibers oriented approximately 55° to the muscle fiber direction is reported (**Fig. 2.2A**) and in pennate muscle, a dense layer of collagen fibers aligned parallel to muscle fibers is reported.[26] To understand collagen's role in passive force transmission, we must consider the unique arrangements of collagen fibers between ECM layers, muscle groups, and changes in arrangement during disease.

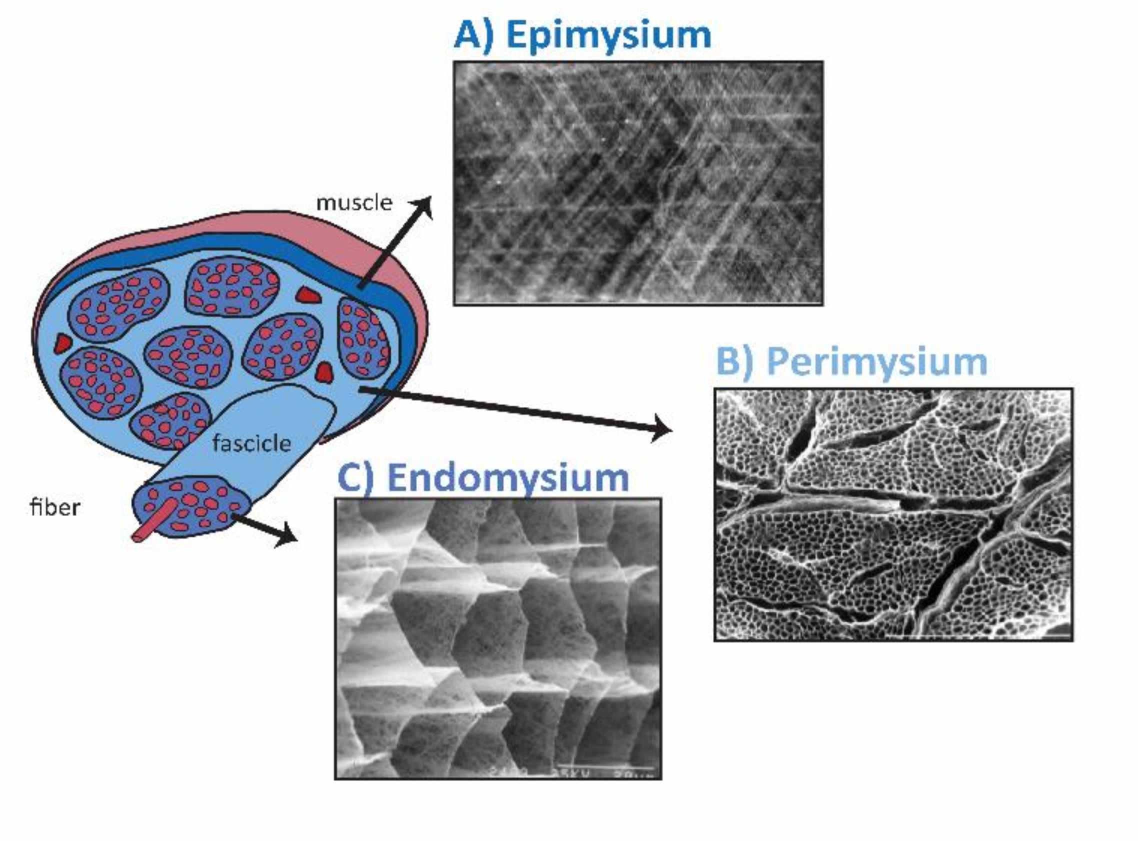

Figure 2.2 Scanning electron microscopy images of decellularized skeletal muscle in the (A) epimysium,[45] (B) perimysium,[45] and (C) endomysium.[16]

Duchene muscular dystrophy impacts skeletal muscle across multiple scales. Duchenne muscular dystrophy (DMD) is a fatal x-linked genetic disorder affecting 1 in 3500 males, with no cure or effective treatment to date.[1] Muscle degeneration results due to a lack in expression of the protein dystrophin, responsible for maintaining the linkage between the intracellular cytoskeleton and extracellular matrix (ECM) (**Fig. 2.3C**).[29] The absence of dystrophin at the muscle fiber membrane increases susceptibility to mechanical stress from everyday muscle contractions. Regenerative capacity of muscle is decreased, with contraction induced damage leading to a chronic state of inflammation and subsequent fibrosis.[2–6] Dystrophic muscle is characterized by changes in composition (fat infiltration, fibrosis, decreased muscle fiber cross-sectional area (CSA)),[30] mechanics (decreased force production, increased stiffness),[31] and cellular pathophysiology (dynamic behaviors of fibroblasts, increased inflammatory cells, depletion of satellite stem cell (SSC) pool)[32,33] (**Fig. 2.3A**). A cycle of dysfunction and disuse results in progressive degeneration, and there remains no cure or effective treatment for DMD. Corticosteroids are the palliative standard of care but carry negative effects (weight gain, bone fractures, scoliosis)[34] and drug therapies (genetic therapies, anti-fibrotics) are only effective in a subset of patients and show variable functional benefits.[35]

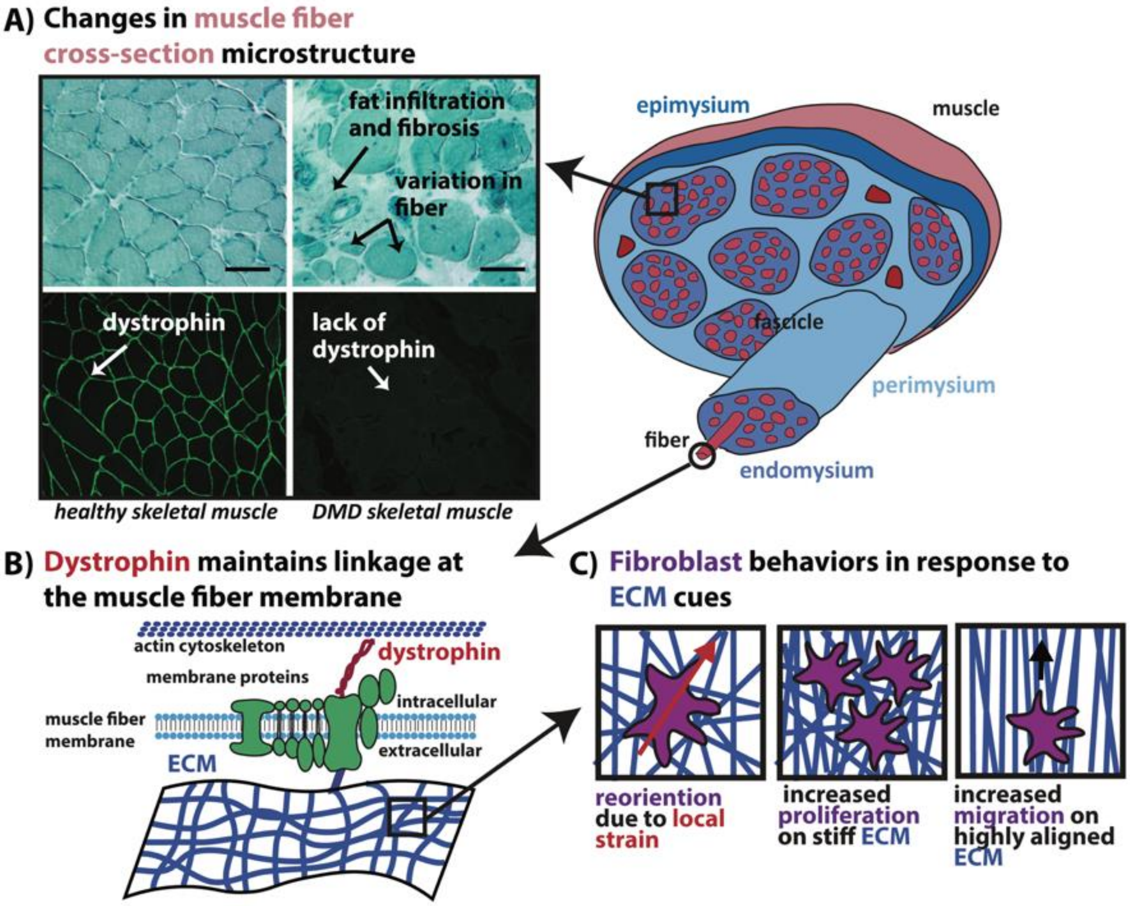

Figure 2.3: (A) <u>Top:</u> Histology of healthy (L) and DMD (R) muscle reveals pathological variations seen in DMD. Scale bar,60mm.[23] <u>Bottom:</u> Immunofluorescence staining of healthy (L) and DMD (R) muscle show a lack of dystrophin expression in DMD.[2] (B) Dystrophin protein maintains linkage between intracellular cytoskeleton and ECM at the muscle fiber membrane. (C) Fibroblast behaviors reported in response to local strain,[49,50] stiffness,[51]and alignment of ECM.[52]

Diaphragm muscle weakening has devasting consequences in DMD. As DMD progresses, pulmonary function declines[36] as the diaphragm muscle weakens.[37–39] Diaphragm muscle dysfunction contributes to respiratory insufficiency, which is a leading cause of death in the mid-twenties.[7] Mechanical ventilation (MV) is required to maintain gas exchange and improves patient survival in DMD,[8] but MV results in diaphragm muscle atrophy and further complications (reintubation, tracheostomy)[9], with the length of MV associated with amount of atrophy.[40] Despite advances in ventilatory supportive devices, there remains variability in the timing and type of MV prescribed to patients and no consensus on which functional parameters should be used to indicate the initiation or extent of ventilator use.[10,11] Diaphragm dysfunction is usually attributed to decline in active contractile properties of diaphragm muscle (loss in strength, decrease in activation) in DMD,[41] overlooking changes in passive muscle properties regulated by the ECM and how these changes influence diaphragm function.[22–24,42]

We must consider how changes in the ECM during fibrosis influence passive muscle properties to better understand diaphragm muscle weakening. One of the primary sources for progressive diaphragm muscle dysfunction in DMD is the development of fibrosis, and indeed, many studies have shown that dystrophic muscles have increased amounts of collagen.[43,44] The dystrophin knockout *mdx* mouse is commonly used to model DMD and *mdx* diaphragm reproduces degeneration seen in DMD patients, with impairment in respiratory function, decrease in muscle fiber CSA, and fibrosis.[12,13,45] However, collagen amount and tissue stiffness are not well correlated in *mdx* diaphragm muscle[14] and we must look beyond collagen amount to characterize the complexity of fibrosis. Structural, mechanical, and chemical properties of the ECM all contribute to a feed-forward cycle in fibrosis. Fibroblasts and myofibroblasts are the primary ECM-secreting cells in fibrosis and regulate collagen fiber networks,[46] with fibroblast alignment a key regulator of collagen alignment.[47,48] Mechanical cues (local strain, stiffness) and structural cues (alignment) from existing ECM regulate behaviors of fibroblasts (alignment, migration, proliferation) (**Fig. 2.2D**).[49,50] Further, increased strains and stiffness activate signaling cascades resulting in transcription of pro-fibrotic genes (ie. TGF-β[51]) and block cleavage sites required for collagen degradation.[52,53]

Changes in collagen microstructure are implicated in diaphragm muscle fibrosis. Increased collagen cross-linking is reported in *mdx* mice, especially in the diaphragm muscle.[54] The ratio of type I/III collagen is also implicated in fibrosis, with elevated type I/III ratio reported in fibrotic lung tissue.[55] Increased levels of both collagen I and III mRNA are reported in *mdx* diaphragm muscle relative to healthy[56] and increased collagen type III is seen in the intramuscular ECM layers of dystrophic human muscle compared to healthy muscle.[57] Beyond skeletal muscle, increased collagen fiber alignment is reported in pulmonary fibrosis[50] and increased collagen fiber straightness is reported in cancerous pancreatic tissue.[58] Collagen fiber alignment is also reported to be a significant predictor of passive lower limb muscle stiffness,[59] but *mdx* lower limb muscle does not mimic the severity of the human phenotype nearly as well as the diaphragm does. The diaphragm muscle ECM is not well characterized, and we must consider the distribution and arrangement of collagen within each ECM layer, as well as changes in microstructure during the progression of fibrosis.

Unlike most skeletal muscles, the diaphragm sustains biaxial loads *in vivo* and exhibits nonuniform and anisotropic behavior. In previous uniaxial mechanical tests of diaphragm muscle tissue, significant differences in stiffness along the muscle fiber direction were not observed between healthy and dystrophic intact diaphragm muscle samples.[4] However, we must consider the unique geometry and biaxial loads sustained by the diaphragm muscle *in vivo*. Diaphragm muscle tissue is anisotropic, with decreased compliance observed in the direction perpendicular to muscle fibers as compared to the compliance along muscle fibers.[61–63] Biaxial experiments in *mdx* diaphragm muscle tissue show significant age effects on tissue properties, with decreased compliance in both along and cross-muscle fiber directions in 9-month-old *mdx* mice compared with very young, 3 week old mice[63]. Additionally, increased compliance was measured in 3-week-old *mdx* mice relative to WT mice, suggesting that the accumulation of fibrotic tissue with aging, rather than the primary loss of dystrophin, contributes to increased tissue stiffness.[63]

It is difficult to extrapolate the role of collagen microstructure on muscle tissue properties from experiments alone. Collagen's contribution to passive diaphragm muscle tissue properties has previously been estimated by performing mechanical testing before and after enzymatically digesting collagen.[60,64] Biaxial experiments in *mdx* and WT diaphragm muscle tissue found greater along- and cross-muscle fiber stiffness in *mdx* relative to WT samples before collagen digestion, but these differences were no longer observed after enzymatically digesting collagen.[64] Similarly, uniaxial experiments in *D2.mdx* and WT mice observed greater along-muscle fiber stiffness in the *D2.mdx* diaphragm relative to WT that was no longer observed after collagen digestion.[60] However, collagen digestion did not significantly decrease the total amount of collagen per weight of the tissue.[60] This suggests that alterations in collagen microstructure during enzymatic digestion contribute to the loss of stiffness, rather than decreased collagen amount, highlighting an important role of collagen microstructure on tissue stiffness.

Computational models provide insight on skeletal muscle across multiple scales.

In whole body level musculoskeletal models, individual muscles are represented by line segments with one dimensional Hill-type lumped parameter models.[65] While these models provide insights on human movement,[66] they simplify the complex geometries of skeletal muscles. Finite-element (FE) modeling allows us to subdivide 3-D geometries into individual “elements”, assign constitutive laws to materials, simulate *in vivo* conditions, and calculate mechanical properties. This technique was applied to reconstruct complex 3-D skeletal muscles and revealed the influence of macroscopic muscle architecture on mechanical properties.[67] In this framework, a new constitutive model was introduced that represents skeletal muscle as hyperplastic, transversely isotropic, and nearly incompressible. This model also defines the material response based on physical based strain invariants governing the along fiber stretch (λ), along fiber shear (B_1), and cross-fiber shear (B_2) (**Fig 2.4**).[67,68] Whole-muscle level models have been developed using this approach and highlight the effects of muscle architectural features such as fascicle arrangements[67] and aponeurosis morphology.[69,70] However, these models lump together connective tissue, muscle fibers, and muscle fascicles into one transversely isotropic material, without accounting for the structure of the ECM.

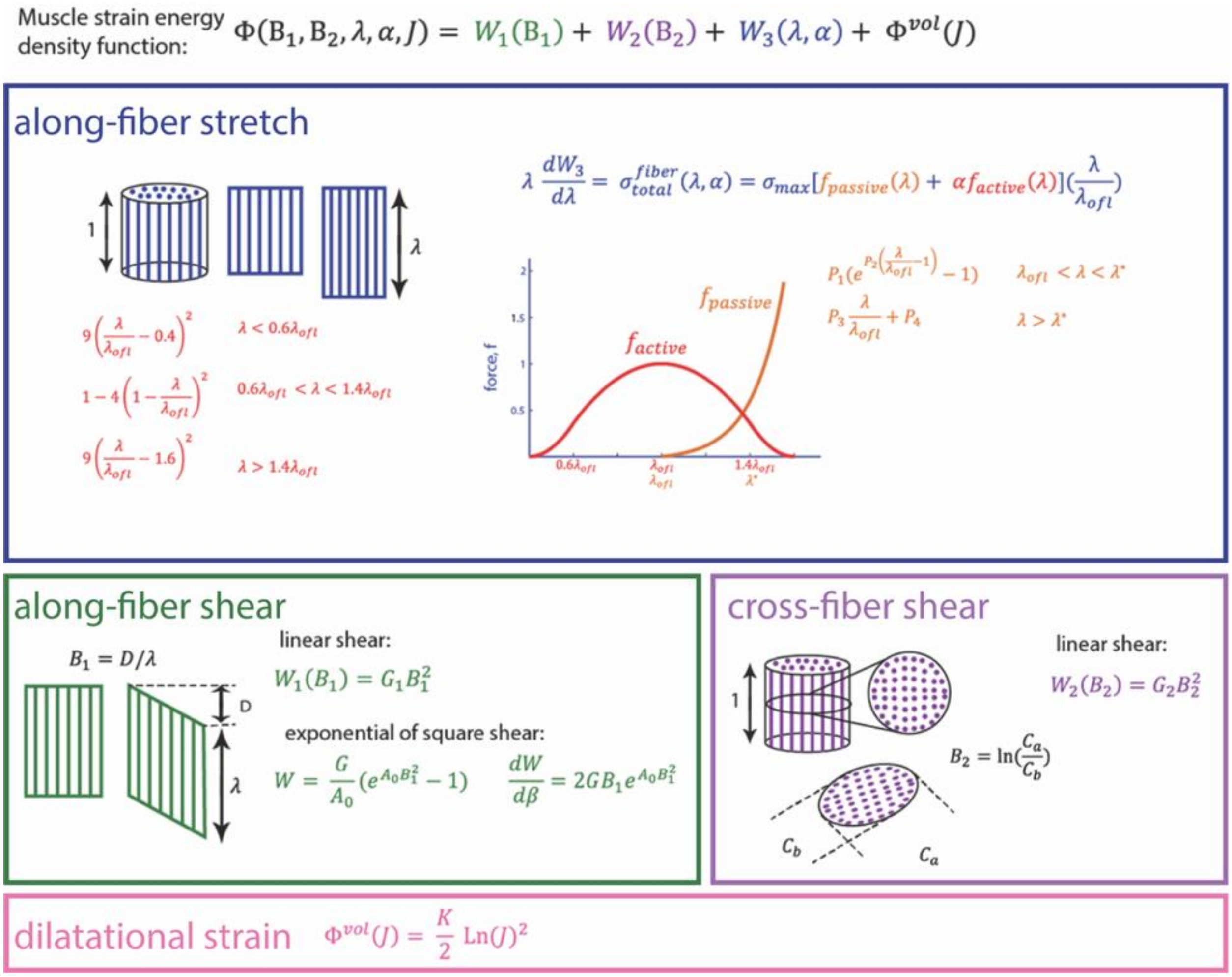

Figure 2.4 Skeletal muscle constitutive model with physically based strain invariants[68] used to relate material properties to experimentally quantifiable measurements.[67]

Micromechanical modeling provides an optimal platform to examine how microstructural variations contribute to macroscopic tissue properties. Micromechanical models were developed to characterize tissue behavior at the muscle fiber and fascicle levels and separate regions of muscle fibers and ECM.[15] These models were generated from images of muscle cross-sections and found that transverse isotropy was maintained at the muscle fiber level. However, the fascicle-level models revealed transversely anisotropic behavior, with macroscopic properties such as shear moduli dependent on fiber and fascicle shapes.[15] When changes in fascicle microstructure seen in DMD, such as variation in muscle fiber cross-sectional area were simulated in these models, the influence of these changes in microstructure on macroscopic properties was dependent on the relative stiffness between the ECM and muscle fibers.[16] Additional methods for micromechanical modeling have also been developed that utilize Voronoi tessellation to replicate muscle fiber geometries,[71] either by estimating muscle fiber sizes and spacing[72,73] or by mapping muscle fiber centroids from histology images.[71,74,75] These techniques improve computational efficiency and have been applied to various contexts such as examining variations in structure along the muscle fiber direction,[74] damage propagation,[73] and aging effects.[75] However, previous micromechanical models have not accounted for distinct ECM layers or focused on the role of changes in collagen microstructure on muscle tissue properties. These models often simplify the representation of the ECM as isotropic,[73] transversely isotropic aligned with muscle fibers,[15,76] or use a generalized helical assumption to represent collagen direction.[71,74,75] These models also rely on integrating measurements from previous experiments across different length scales and muscle groups. To examine the influence of collagen organization on diaphragm muscle tissue level properties, we must consider the full microstructure of ECM surrounding and within diaphragm muscle tissue.

Chapter 3

Diaphragm muscle fibrosis involves changes in collagen organization with mechanical implications in Duchenne Muscular Dystrophy

Acknowledgements: C. Hunter Wallace, Brian K. Jones, Silvia S. Blemker

Before you can achieve
you must believe in yourself.

You are more capable than you think.

—Simone Biles

3.1 Abstract

In Duchenne muscular dystrophy (DMD), diaphragm muscle dysfunction results in respiratory insufficiency, a leading cause of death in patients. Increased muscle stiffness occurs with buildup of fibrotic tissue, characterized by excessive accumulation of extracellular matrix (ECM) components such as collagen, and prevents the diaphragm from achieving the excursion lengths required for respiration. However, changes in mechanical properties are not explained by collagen amount alone and we must consider the complex structure and mechanics of fibrotic tissue. The goals of our study were to (1) determine if and how collagen organization changes with the progression of DMD in diaphragm muscle tissue, and (2) predict how collagen organization influences the mechanical properties of the ECM. We first visualized collagen structure with scanning electron microscopy (SEM) images and then developed an analysis framework to quantify collagen organization and generate image-based finite-element models. The image analysis revealed increased collagen fiber straightness (2.04-10.03%) and alignment (4.99-15.52%) in diseased relative to healthy mice and increased collagen fiber straightness (0.67-5.39%) in old relative to young healthy mice. Collagen fibers retained a transverse orientation relative to muscle fibers (69.68-89.90˚) in all groups. All mechanical models predicted an increase in the transverse relative to longitudinal (muscle fiber direction) stiffness, with a 64.22-176.65% increase in stiffness ratio (transverse/longitudinal) in diseased relative to healthy models. This study revealed changes in diaphragm ECM structure and mechanics during disease progression in the *mdx* muscular dystrophy mouse phenotype, highlighting the need to consider the role of collagen organization on diaphragm muscle function.

Key Words

Duchene muscular dystrophy, fibrosis, collagen organization

New & Noteworthy

Scanning electron microscopy images of decellularized diaphragm muscle from WT and *mdx,* Duchenne muscular dystrophy model*,* mice revealed that collagen fibers in the epimysium are oriented transverse to muscle fibers, with age- and disease- dependent changes in collagen arrangement. Finite-element models generated from these images predicted that changes in collagen arrangement during disease progression influence the mechanical properties of the extracellular matrix. Thus, changes in collagen fiber-level structure are implicated on tissue-level properties during fibrosis.

3.2 Introduction

Duchenne muscular dystrophy is a devastating disease with no cure and diaphragm muscle weakness leads to death. Duchenne muscular dystrophy (DMD) is a fatal genetic disease, with devastating impacts from the subcellular to whole muscle levels. Muscle degeneration results due to a lack in expression of the protein dystrophin, responsible for maintaining the linkage between the intracellular cytoskeleton and extracellular matrix (ECM).[29] Current therapies are targeted towards either replacing the dystrophin protein or treating the secondary and downstream pathological mechanisms, yet there remains no cure. [35] Drug therapies (ie. genetic therapies, anti-fibrotics) show promise for the treatment of DMD, but are only effective in a subset of patients and show variable functional benefits.[35] The absence of dystrophin at the muscle fiber membrane increases susceptibility to mechanical stress from everyday muscle contractions. Regenerative capacity of muscle is decreased, with contraction induced damage leading to a chronic state of inflammation and subsequent fibrosis.[2–6] A cycle of dysfunction and disuse results in progressive muscle wasting, with differences in severity and progression across muscles.[77] Lower limb muscle is impacted in the earlier stages of DMD, leading to a loss of ambulation at 10-14 years of age. At later stages of the disease, the diaphragm, the main inspiratory muscle,[78] is severely impacted. Diaphragm muscle weakness progresses with age in DMD and contributes to respiratory insufficiency, a leading cause of death in the early to mid-20s.[7,37]

Fibrosis limits muscle function, but the structure and mechanics of fibrotic tissue are not well characterized in diaphragm muscle. One of the primary sources for progressive muscle dysfunction in DMD is the development of fibrosis, characterized by excessive accumulation of extracellular matrix (ECM) components such as collagen. Indeed, many studies have shown that dystrophic muscles have increased amounts of collagen,[43,44] but collagen amount does not correlate with stiffness in diaphragm muscle tissue from *mdx* mice, the most common animal model used to study DMD.[14] *Mdx* lower limb muscle shows an increase in collagen fiber alignment.[59] While collagen fiber amount does not predict tissue stiffness, collagen fiber alignment is reported to be a significant predictor of passive lower limb muscle stiffness.[59] However, the *mdx* lower limb muscle does not mimic the severity of the human phenotype nearly as well as the diaphragm does. Similar to the human condition, *mdx* mice exhibit impairment in respiratory function[79,80], decrease in diaphragm muscle fiber cross-sectional area, and increased diaphragm muscle fibrosis.[12,13,45,81] Beyond skeletal muscle, changes in collagen organization with fibrosis are implicated in additional tissue systems. Increased collagen fiber alignment is reported in pulmonary fibrosis[50] and increased collagen fiber straightness is reported in cancerous pancreatic tissue.[58] Changes in collagen organization, such as collagen fiber direction, alignment, and straightness, remain unknown in *mdx* diaphragm muscle, but are needed to understand how and why diaphragm muscle mechanics change during the progression of DMD.

Finite element models allow us to study structure-function relationships in biological tissues. In prior studies, collagen organization is related to passive properties of skeletal muscle measured by mechanical testing of intact muscle.[14,59] The contribution of the ECM to the passive properties of skeletal muscle is shown by indirect measurements, comparing properties of single muscle fibers and muscle fiber bundles with intact ECM,[22–24] and direct measurements of properties of decellularized muscle fiber bundles.[42] While it is difficult to isolate the influence of organizational parameters on ECM properties with traditional mechanical testing, finite-element (FE) models allow us to isolate the impact of specific structural variations on mechanical properties. Whole muscle-level FE models reveal the influence of macroscopic muscle architecture on mechanical properties[67] but have been limited in their representation of the ECM. These models typically lump together connective tissue, muscle fibers, and muscle fascicles into one transversely isotropic material, without accounting for changes in ECM structure during fibrosis.[67,82–84] Micromechanical muscle models at the fascicle-level reveal transversely anisotropic behavior, with macroscopic properties such as shear moduli dependent on fiber and fascicle shapes.[15] When changes in fascicle microstructure seen in DMD, such as variation in muscle fiber cross-sectional area were simulated in these models, the influence of these changes in microstructure on macroscopic properties was dependent on the relative stiffness between the ECM and muscle fibers.[16] However, these muscle fascicle-level FE models assumed that the ECM was aligned with muscle fibers and did not account for changes in the structure of the ECM during DMD. Therefore, as we apply these modeling techniques to study fibrotic muscle, we must first consider the complex structure and function of the ECM.

We aim to quantify changes in ECM structure and mechanics during the progression of diaphragm muscle fibrosis. The goals of our study were to (1) determine if and how collagen organization changes with the progression of DMD in diaphragm muscle tissue, and (2) predict how collagen organization influences the mechanical properties of ECM. We aimed to characterize collagen organization within the epimysium and predict how changes in its structure are implicated on both transverse (cross muscle fiber) and longitudinal (along muscle fiber) tissue properties during disease progression. To do so, we developed an image-based finite-element modeling pipeline to explore the influence of collagen organization on ECM mechanics. We collected scanning electron microscopy (SEM) images of epimysium isolated from *mdx* and wild-type (WT) control mice at 3, 6, and 12 months, and quantified collagen fiber direction, alignment, and straightness. We then generated finite-element models and simulated biaxial stretch to determine the implications of our collagen organization measurements on ECM mechanical properties.

3.3 Methods

Animal protocol

All experiments were approved by the University of Virginia Animal Care and Use Committee. This study was conducted in C57BL/10ScSn-Dmdmdx/J male mice (referred to as *mdx*), bred inhouse, and C57BL/6J male mice (referred to as WT), purchased from Jackson Laboratories. Our study groups included 3, 6, and 12-month-old mice, both WT and *mdx* (n=6 mice per group).

Ex vivo sample collection and imaging

After humane euthanasia, the diaphragm muscle was excised and samples from the costal region were dissected and placed in phosphate-buffered saline. We followed a standard sodium hydroxide digestion protocol to leave only collagen fibrils, removing the muscle fibers, sarcolemma, basement membrane, and proteins associated with the ECM.[25] Although we imaged the outer epimysial layer of the ECM, the digestion process was required for clear imaging, visualization, and quantification of collagen fibers alone (**Supplemental Fig. 3.1:** https://figshare.com/s/61c8117024f275f39e2c). Excised muscle samples were first placed in fixative for 24 hours (8% glutaraldehyde,16% paraformaldehyde, 0.2M sodium cacodylate). Samples were then placed in digestion solution (10% sodium hydroxide) for approximately 6 days, and then rinsed in H_2O for 24 hours. Since samples were physically unconstrained during enzymatic digestion, this protocol left the tissue in a zero-strain configuration after muscle fibers were digested. Therefore, the arrangement of collagen fibers reflects their position with the tissue in a stress-free state. Samples were prepared for Scanning Electron Microscopy (SEM) imaging following standard dehydration with a graded series of EtOH (10-100%), mounted on 1/8” stubs, and sputter coated in gold. Care was taken to ensure that tissue samples were mounted such that SEM images of the surface plane captured the outer epimysial layer of the ECM. One image per sample was captured at the following magnifications: 40X, 500X, 1kX, 15kX to visualize collagen organization (Zeiss Sigma VP HD field SEM). Images collected at 1kX were then used for measurements in our image analysis. SEM images collected in this study are publicly available (https://figshare.com/s/34012e1d437c69a9c2ec).

Image analysis

Muscle fiber direction: After enzymatic digestion in sodium hydroxide, collagen structure was isolated from samples of diaphragm muscle. Ridges in tissue samples were still evident, indicating the presence of muscle fibers that had been digested from the samples (**Fig. 3.1A**). From these features, we measured muscle fiber direction manually from raw images (1024x768 pixels) by tracing three locations along the length of digested muscle fibers and averaging the angles of the traces (**Fig. 3.1A**). Images collected at 1kX magnification were rotated such that the muscle fiber direction aligned with the horizontal direction, and then the images were cropped to a square (540x540 pixels) (Adobe Illustrator) (**Fig. 3.1B**). Images collected at 15kX were used to confirm successful digestion by visually inspecting that collagen fibers were isolated and other proteins and attachments in the ECM were eliminated (**Fig. 3.1C**).

Collagen fiber straightness: Collagen straightness (P_s) was determined using the following relationship:

$$P_s = L_o/L_f$$

Equation 3.1

where L_f, collagen fiber length, was calculated by manually tracing the contour path length of a representative collagen fiber, and L_o, the linear end-to-end straight-line length, was determined by drawing a straight line connecting the ends of the measured fiber. The collagen straightness parameter was then calculated for three representative fibers and averaged (ImageJ) (**Fig. 3.1D**).

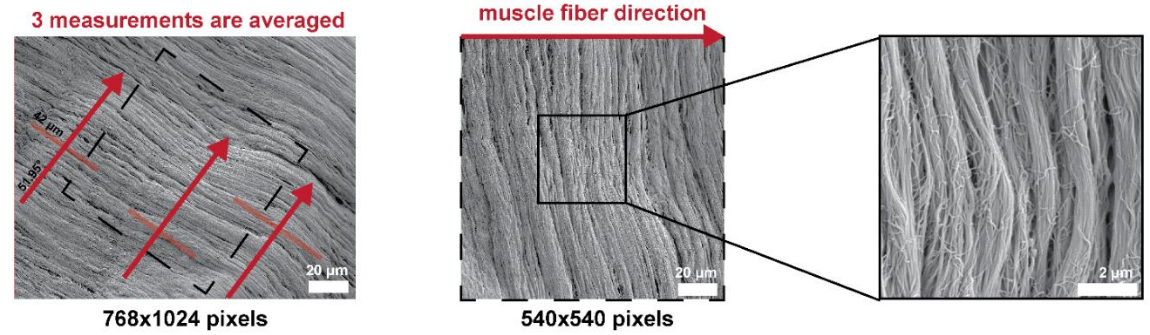

A) Muscle fiber direction is measured manually.

B) 1kX image is cropped and rotated.

C) 15kX image is used to confirm digestion.

D) Collagen straightness (Ps) is calculated at 1kX as the ratio of the linear end-to-end length (Lo) vs contour path length (Lf) of a collagen fiber.

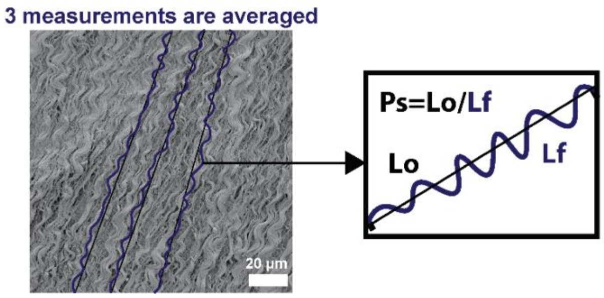

Figure 3.1. Overview of muscle fiber direction and collagen fiber straightness measurements from SEM images.

Image processing algorithm

Local collagen measurements: We developed an image processing algorithm to automatically measure collagen orientation within subregions of each image in MATLAB (MathWorks Inc., Natick, MA). Each image was discretized into 4,096 sub-regions of 16x16 pixels (**Fig. 3.2A**). We utilized built-in image processing functions (MATLAB R2018b and Image Processing Toolbox 3.5.8) to measure collagen fiber direction. Each sub-region of the image (i) was first thresholded using Otsu's method.[85] Collagen pixel ratio (cpr_i) was calculated by dividing the number of white pixels detected as collagen fibers (n_{coll}) by the number of total pixels (n_{tot}) (**Fig. 3.2B**).

$$cpr_i = \frac{n_{coll}}{n_{tot}}$$

Equation 3.2

Fiber boundaries were determined from thresholded image subregions using canny edge detection (**Fig. 3.2C**). We then computed the Radon transform[86,87] at fiber boundaries to measure fiber orientation[88–90]. The Radon transform, $R_\Theta(a')$ provides the predominant angle of fiber alignment in a subregion by computing line integrals along parallel-beam projections oriented at discrete rotation angles (Θ) and spaced 1 pixel apart. For a two-dimensional function, $f(a,b)$, a and b are the horizontal and vertical axes and a' and b' are the axes of the parallel-beam projections determined by the prescribed rotation angle (Θ). Eqns 3-4 describe the Radon transform:

$$R_\theta(a') = \int_{\infty}^{\infty} f(a'cos\theta - b'sin\theta, a'sin\theta + b'cos\theta)db'$$

Equation 3.3

$$\begin{bmatrix} a' \\ b' \end{bmatrix} = \begin{bmatrix} cos\theta & sin\theta \\ -sin\theta & cos\theta \end{bmatrix} \begin{bmatrix} a \\ b \end{bmatrix}$$

Equation 3.4

For each image subregion, we computed the Radon transform $R_\Theta(a')$ while varying rotation angle ($0° < \Theta < 180°$). The subregion Radon transform reaches a unique maximum value at the angle of greatest pixel alignment. The maximum value of the Radon transform was taken as a measure of collagen alignment within each image subregion.

$$R_{peak} = max(R_\theta(a'))$$

Equation 3.5

The angle of greatest pixel alignment was taken as the subregion predominant collagen fiber direction (α_i) and confined to the first two quadrants such that ($0° < \alpha_i < 180°$). (**Fig. 3.2D**).

$$\{\alpha_i\} = \underset{\theta}{arg\,max}\,(R_\theta(a'))$$

Equation 3.6

Predominant collagen fiber direction α_i and peak Radon intensity R_{peak} were calculated for all 4,096 image subregions (**Fig. 3.2E**).

Mean collagen measurements: We utilized built-in MATLAB circular statistics functions[91] to calculate mean collagen direction and strength of alignment. Subregion collagen directions (α_i) were converted to unit vectors ($\mathbf{r}_i$) and averaged to obtain the image mean resultant vector ($\bar{\mathbf{r}}$).

$$\mathbf{r_i} = \begin{pmatrix} cos(\alpha_i) \\ sin(\alpha_i) \end{pmatrix}$$

Equation 3.7

$$\bar{\mathbf{r}} = \frac{1}{N}\sum \mathbf{r_i}$$

Equation 3.8

Next, the mean collagen fiber direction (*cfd*) was calculated per image as the acute angle of $\bar{\mathbf{r}}$ relative to the horizontal axis, such that ($0° < cfd < 90°$). (**Fig. 3.2H**). The resultant vector length was used to calculate the strength of collagen fiber alignment ($0 < SA < 1$, 1=high alignment), capturing the circular spread in local orientations per image.

$$SA = \|\bar{\boldsymbol{r}}\|$$

Equation 3.9

The mean in peak Radon intensity was determined per image as a measure of subregion collagen alignment. The mean collagen pixel ratio was also determined per image as a measure of the number of pixels detected as collagen. Our SEM images were collected of the surface of the epimysium and thus, the collagen pixel ratio corresponds to the density of collagen in the imaging plane.

$$cpr_{image} = \frac{1}{N}\sum_i cpr_i$$

Equation 3.10

Sensitivity and validation: To validate the image processing algorithm and determine the appropriate subregion size, we first used our image processing algorithm with two manually-generated sets of test images of dark lines that approximated collagen fibers.

In the first image set, we varied collagen (line) direction over the range $0° < cpd < 90°$ while holding strength of alignment constant ($SA_{known}=1$) (**Supp. Fig. 3.2A**). In the second set, we varied strength of alignment over the range $0.92 < SA < 0.99$ with collagen direction constant ($cpd_{known}=90°$) (**Supp. Fig. 3.2B**). To test the sensitivity of our algorithm to the image subregion size, we also varied the number of image subregions ($2x2 < NxN < 128x128$) and calculated the error between the known collagen direction and strength of alignment in our test images vs. the values determined by our image processing algorithm. As we increased the number of image subregions, error in collagen direction increased (**Supp. Fig. 3.2C**), with error in strength of alignment minimized at the 64x64 subregion size, corresponding to 1.8x1.8 µm (**Supp. Fig.2D**). Based on this analysis, we selected the 64x64 subregion size, which yielded a collagen direction error of 0.35° and a strength of alignment error of 0.014. (**Supplemental Materials 3.2**: https://figshare.com/s/794d28b5628a81b6e294)

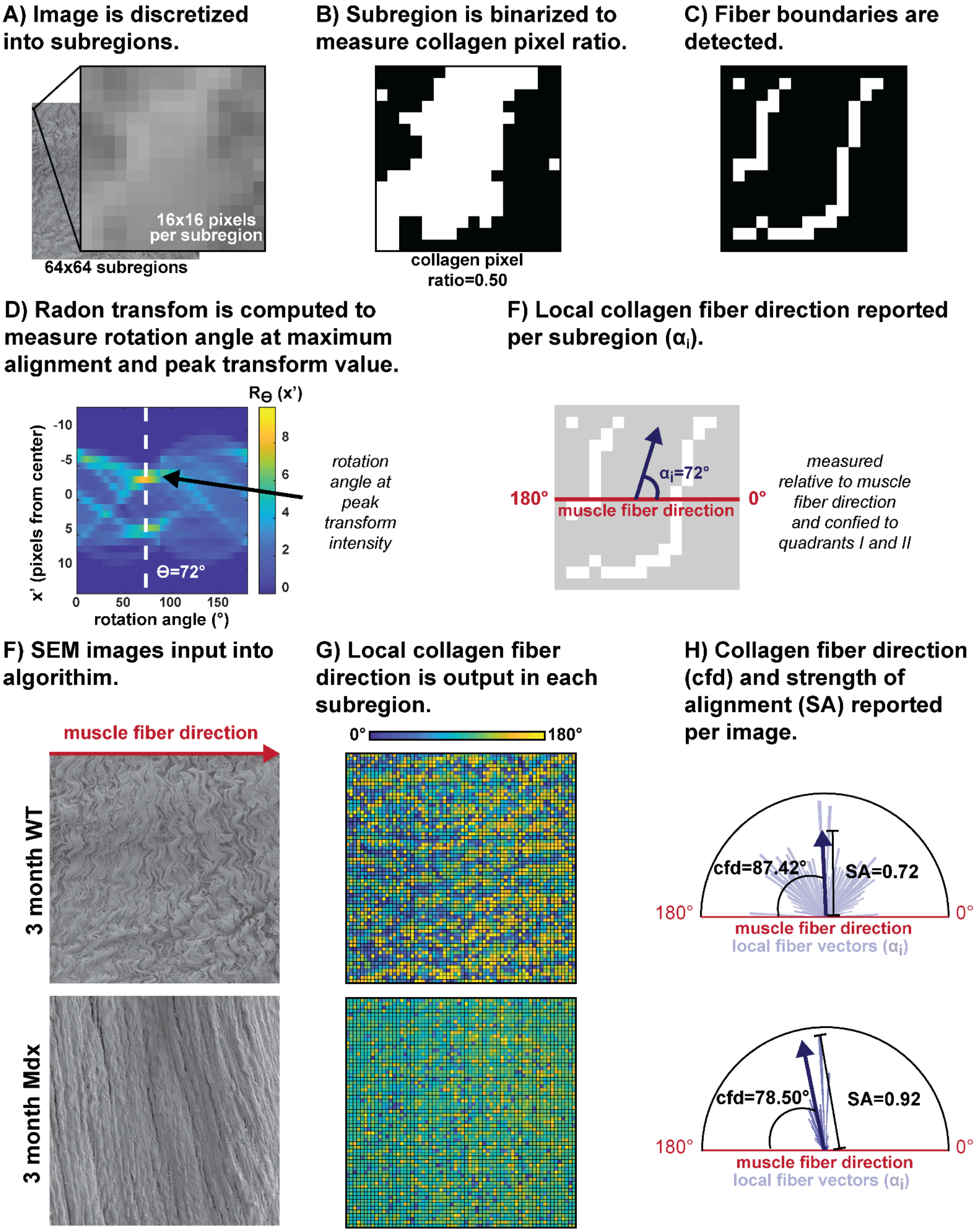

Figure 3.2 Overview of local collagen fiber direction measurements from SEM images.

In silico finite-element modeling

Geometry: We generated finite-element (FE) models in the nonlinear finite element solver, FEBio (Musculoskeletal Research Laboratories, University of Utah, Salt Lake City, UT, USA).[92] FE models corresponded to the height and width of our cropped SEM images (118μm x 118μm), with a constant thickness (3μm). The FE model was meshed into 64x64 hex8 elements, with each element corresponding to one subregion (1.8μm x 1.8μm), from our image processing algorithm (**Fig. 3.3A**).

Material law: Connective tissue is often modeled as a composite of collagen fibers embedded in an isotropic "ground matrix".[93–96] The "ground matrix" is referred to as a gel-like amorphous substance and contains all non-fibrillar components of the ECM (e.g. proteoglycans, glycosaminoglycans).[43] Collagen fibers contribute only to the tensile properties of the ECM. Their stress-strain behavior exhibits distinct toe and linear regions under tensile deformation as collagen fibers uncrimp and straighten.[97] To represent the skeletal muscle ECM, we assigned a coupled solid mixture constitutive model to the geometry. Collagen fibers were modeled as a toe-linear fiber[98], where the strain energy density is a function of the fiber stretch λ. A transition from the toe to linear region occurs at λ_0, where β is the power law exponent in the toe region and E is the linear fiber modulus. The remaining ground substance of the ECM was modeled as a Mooney-Rivlin material[99] where c_1 and c_2 are the Mooney-Rivlin material coefficients and K is a bulk modulus-like penalty parameter for the coupled solid mixture. Specific details and constitutive equations of these materials can be found in the FEBio user manual (help.febio.org).

Material parameters: The toe region of the collagen fiber stress-strain curve is associated with both the straightening of wavy collagen fibers[100,101] and collagen fiber realignment,[102] often modeled with $\lambda_0=1.06$.[103] We explicitly modeled collagen fiber straightness by discretizing our image into subregions and measuring local collagen directions. Since collagen fiber straightening is already accounted for in our model, we used a constant stretch ratio of $\lambda_0=1.01$, such that it only accounts for the contribution of collagen fiber realignment within the image sub-regions. Due to the wide range of values for collagen fiber stiffness and ground matrix stiffness reported in the literature, we varied the ratio of E to c_1 and conducted a sensitivity analysis described in detail in Supplemental Materials (**Supplemental Materials 3.3:** https://figshare.com/s/b5397e2c2093d2dbdd26). Based on that analysis, we saw that the influence of collagen fiber stiffness on the effective stiffness ratio began to stabilize when the ratio of E to c_1 was greater than 500. Therefore, we selected a collagen fiber modulus 800 times greater than the ground matrix stiffness ($E=800MPa$, $c_1=1MPa$). We then selected a bulk modulus to ensure incompressibility ($K=100{,}000MPa$).[96] The purpose of our FE models was to isolate the effect of ~1µm scale structural changes of collagen fiber organization on ~100 µm scale tissue mechanical behavior. Therefore, the material parameters shown in **Table 3.1** were held constant for all SEM-image based models. Material axes were then assigned per element to reflect the subregion collagen direction measurements (α_i) obtained from our image processing algorithm, with fiber angles in the x-y plane (**Fig. 3.3B**). The x axis corresponded to the longitudinal (muscle fiber) direction, the y axis corresponded to the transverse (cross-muscle fiber) direction, and the z axes was orthogonal to the x and y axes.

Table 3.1 Material parameters for coupled solid mixture material in SEM-image based mechanical models

Toe-linear collagen fiber		
E	Fiber modulus in the linear range	800 MPa
β	Power-law exponent in the toe region	3
λ_0	Stretch ratio when toe region transitions to the linear region	1.01
Mooney-Rivlin ground matrix		
c_1	Mooney-Rivlin c1 parameter	1 MPa
c_2	Mooney-Rivlin c2 parameter	0 MPa
K	Bulk-modulus	100,0000 MPa

Boundary conditions: We assigned boundary conditions to simulate an equibiaxial 20% engineering strain (**Fig. 3.3C**), by prescribing displacements to the +y and +x mesh surfaces corresponding to the top and right edges of the SEM image, respectively. The -y surface was fixed in y, the -x surface was fixed in x, and the +z surface was fixed in z.

Model outputs: Cauchy stress and Lagrange strain, in the longitudinal (x, muscle fiber) and transverse (y, cross-muscle fiber) directions, were output for each element and averaged to determine the stress-strain curve for each model (**Fig. 3.3D**). Effective stiffness in the longitudinal (k_{long}) and transverse (k_{trans}) directions were measured with a linear fit of the 18, 19, and 20% strain points and effective stiffness ratio was then calculated for each model ($k_r = k_{trans}/k_{long}$) (**Fig. 3.3E**). A sensitivity analysis was performed to determine the influence of applied strain percentage on model outputs of transverse and longitudinal stiffness. We found that model outputs of stiffness stabilized between 15-20% strain. Further, strain percentage did not influence the trends between model outputs and thus our overall conclusions were not sensitive to the strain value. We normalized model outputs of stress and stiffness by collagen fiber modulus ($E=800\ MPa$) due to uncertainty in estimates for our material parameters.

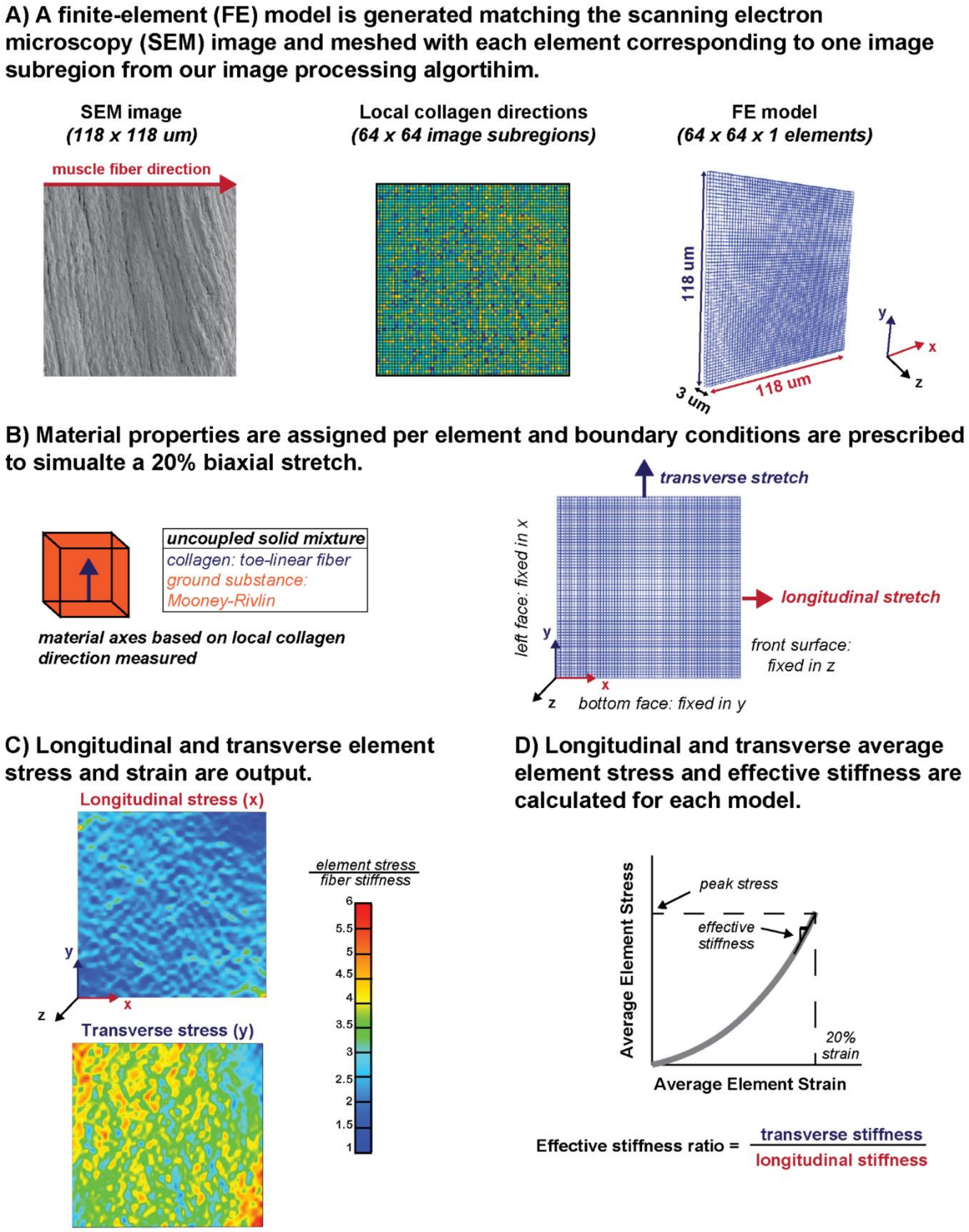

A) A finite-element (FE) model is generated matching the scanning electron microscopy (SEM) image and meshed with each element corresponding to one image subregion from our image processing algortihim.

B) Material properties are assigned per element and boundary conditions are prescribed to simualte a 20% biaxial stretch.

C) Longitudinal and transverse element stress and strain are output.

D) Longitudinal and transverse average element stress and effective stiffness are calculated for each model.

Figure 3.3 Overview of SEM image-based finite-element model framework.

Structure-function relationships between collagen organization and ECM stiffness

To determine if ECM-level properties could be predicted by collagen-fiber level organization, we first compared our measurements of collagen fiber organization from the SEM images with mechanical properties output from the corresponding SEM-image based models (**Fig. 3.8**). This analysis allowed us to ask questions such as, *"Do changes in collagen fiber straightness, collagen fiber direction, or collagen fiber alignment measured in SEM images predict changes in effective stiffness predicted in FE models?"* To predict the influence of specific parameters of collagen organization on mechanical properties, we then simulated changes in each parameter alone in "simplified" images that we manually generated. We then used our modeling pipeline to measure the effective stiffness in FE models based on each simplified image. This allowed us to determine "theoretical" structure function relationships (**Fig. 3.9**) and answer questions such as, *"How do collagen fiber straightness and collagen fiber direction influence ECM stiffness independently?"*. By comparing the theoretical relationships with SEM image-based models we then asked questions such as, *"Do SEM image-based models follow theoretical structure-function relationships?".*

Simplified image-based models: First, we created images with varied collagen fiber direction ($5° < cfd < 85°$), with collagen fiber straightness constant at 1.0 and then 0.85, since the straightness parameters from SEM images fell within this range (**Supp. Fig. 3.4A**). Next, we varied collagen fiber straightness ($0.589 < P_s < 0.997$) while holding fiber direction constant at 90° and then 70°, since the collagen fiber directions from SEM images fell within this range (**Supp. Fig. 3.4B**). We generated FE models from each simplified image and plotted the key model outputs (transverse/cross-muscle fiber stiffness, longitudinal/muscle-fiber stiffness, stiffness ratio) vs. the parameter that was varied in the simplified image. We then conducted nonlinear regression analysis to fit theoretical curves to the relationships between each key model output and collagen fiber direction (**Supp. Fig. 3.4C**), as well as collagen fiber straightness (**Supp. Fig. 3.4D**). For all theoretical models we matched the collagen fiber stiffness and ground matrix stiffness from the SEM image-based models ($E=800MPa$, $c1=1MPa$) and selected a bulk modulus to ensure incompressibility ($K=100\ MPa$) (**Supplemental Materials 3.4:** https://figshare.com/s/2fe7931de519cb2864de). The image processing and modeling code is publicly available (https://github.com/ridhisahani/sem-fem).

Statistical analysis

Comparison of image measurements and model outputs between groups: A two-way analysis of variance (ANOVA) with age (3, 6, 12 months) and group (*mdx* vs WT) as factors was performed for the following measurements: (1) collagen pixel ratio, (2) collagen fiber direction relative to muscle fiber direction, (3) collagen fiber straightness parameter, (4) collagen fiber strength of alignment, (5) longitudinal/muscle-fiber direction effective stiffness, (6) transverse/cross-muscle fiber direction effective stiffness, (7) effective stiffness ratio. Assumptions of random sampling, equal variance, and normality of residuals were confirmed with qq plots and distribution plots. When applicable, Tukey HSD post-hoc comparison was performed to determine which groups were significantly different. Alpha was set at 0.05 for all tests.

Structure-function relationships between image measurements and model outputs: Nonlinear and linear regression were used to fit relationships between model outputs and collagen fiber organization (MATLAB (R2018b) and Curve Fitting Toolbox 3.5.8).[104] For the SEM image based models, we fit linear relationships between image measurements (collagen fiber direction, collagen fiber straightness, collagen fiber alignment) and ECM effective stiffness (transverse/cross-muscle fiber direction, longitudinal/muscle-fiber direction), confirming assumptions of linear regression. For our models based on the simplified images, the assumptions for linear regression were no longer met. Therefore, we fit power law and exponential relationships between the parameters varied in the simplified images (collagen fiber direction, collagen fiber straightness) and model outputs of ECM effective stiffness (transverse, longitudinal). Power law relationships were better fits between collagen fiber straightness and ECM effective stiffness (transverse, longitudinal), and exponential relationships were better fits between collagen fiber direction and ECM effective stiffness (transverse, longitudinal). For all models, both SEM image based and simplified image based, we determined the stiffness ratio by dividing the curve fits for transverse effective stiffness by the curve fits for longitudinal effective stiffness.

3.4 Results

Collagen fibers were straighter and more highly aligned in *mdx* and older WT mice but retained a transverse orientation relative to muscle fibers.

Changes in collagen fiber organization can be detected visually in the SEM images (**Fig.3.4**). Collagen fiber straightness was significantly greater in *mdx* over WT at 3 months (*mdx*=0.976±0.0108, WT=0.887±0.0309, p=3.3e-6) and 6 months (*mdx*=0.942±0.0182, WT=0.881±0.0163, p=1.0e-3). Collagen fiber straightness was also significantly greater in 12-month-old WT (0.931±0.0289) over 3-month-old WT (0.887±0.0309), (p=0.027), as well as 12-month-old WT (0.931±0.0289) over 6-month-old WT (0.881±0.0163), (p=0.0090) (**Fig. 3.5A**). Collagen fiber strength of alignment was significantly greater in *mdx* over WT groups at 3 months (*mdx*=0.876±0.0333, WT=0.759±0.0416, p=3.0e-5) and 6 months (*mdx*=0.840±0.0315, WT=0.759±0.0368, p=4.5e-3) (**Fig. 3.5B**). Collagen pixel ratio ranged from 0.47-0.61, with no significant differences between age or disease groups (**Fig. 3.5C**). Collagen fiber direction relative to muscle fiber direction ranged from 70-90°, with no significant differences between age or disease groups (**Fig. 3.5D**).

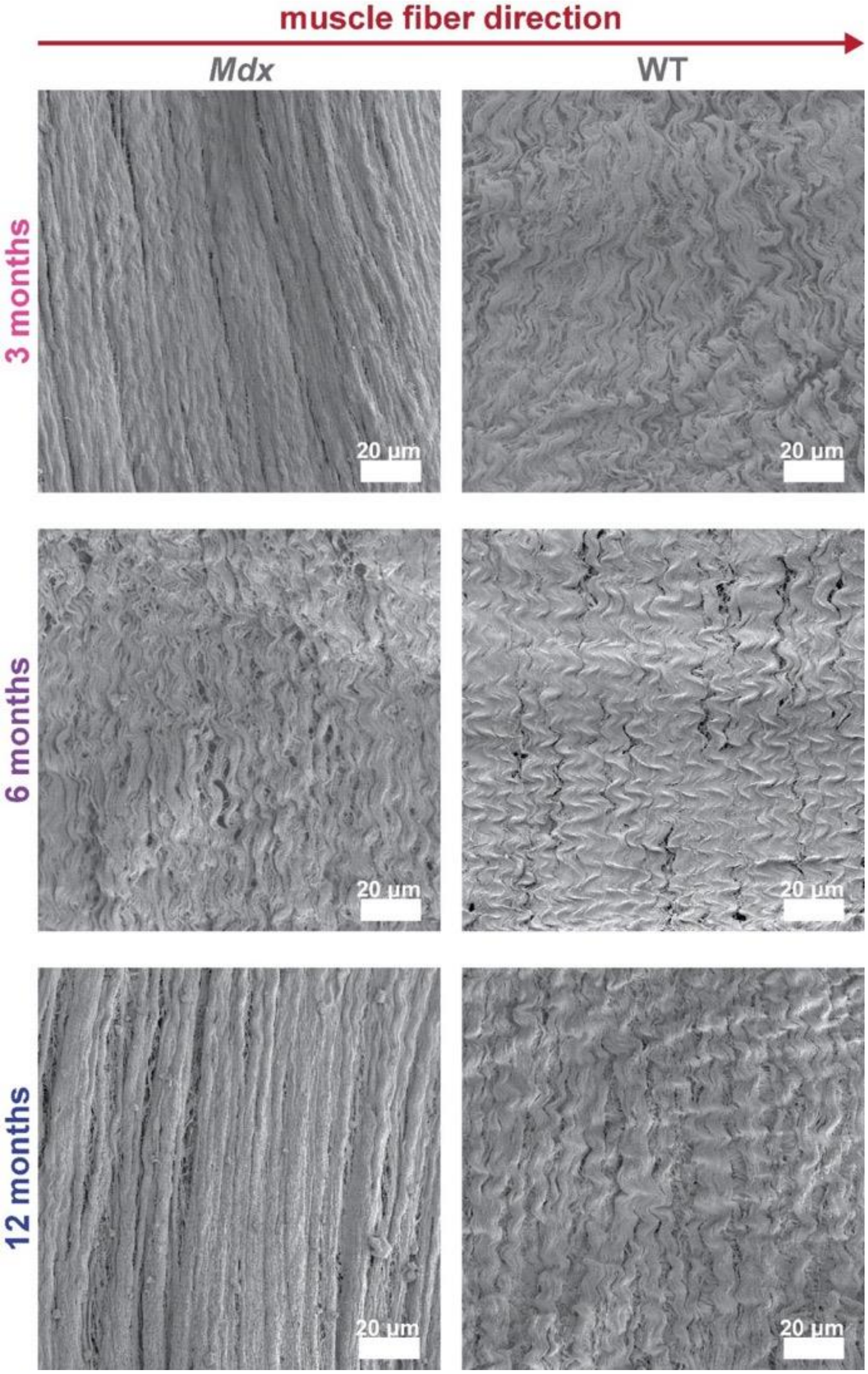

Figure 3.4 SEM images of epimuscular collagen in mdx and WT mice.

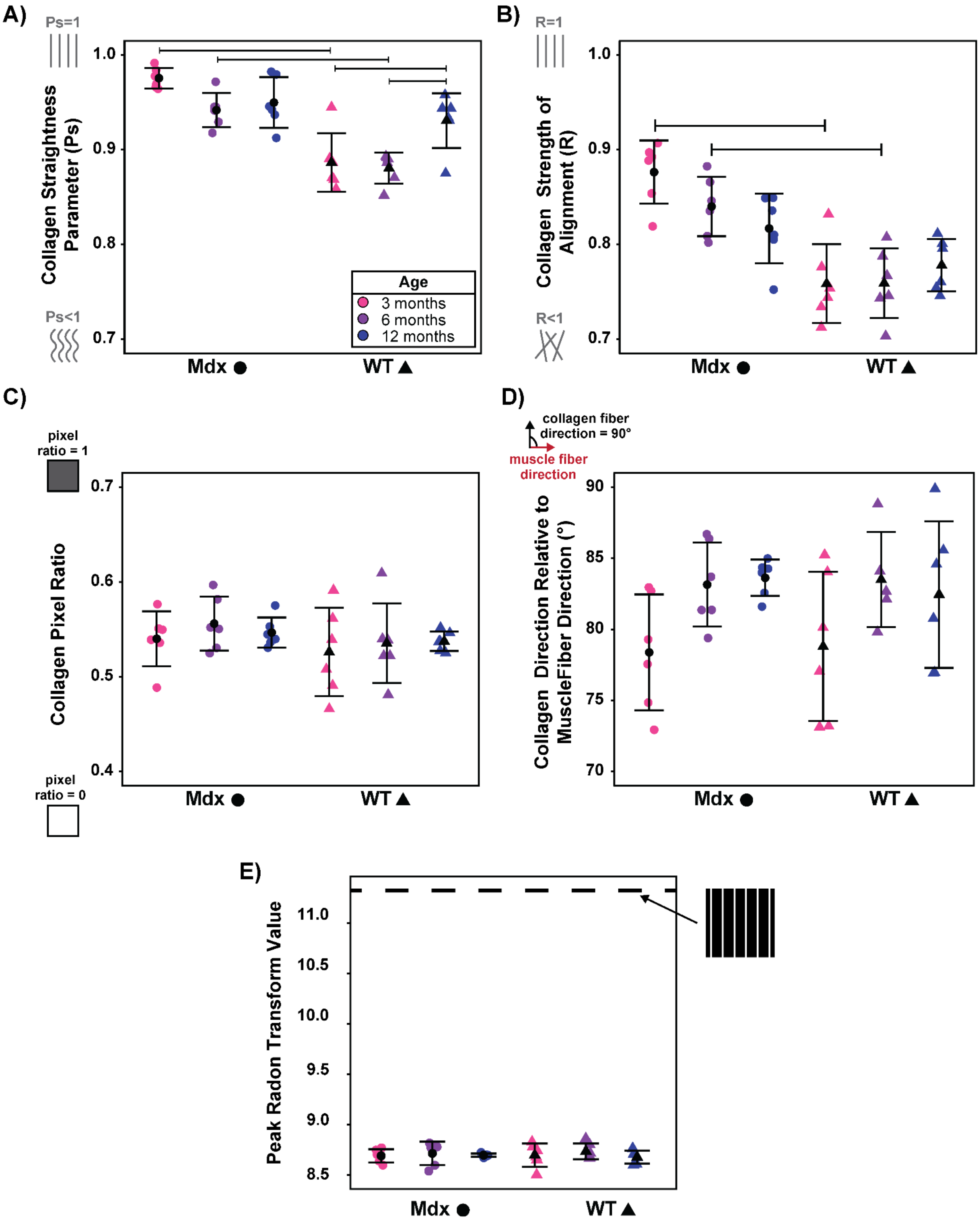

Figure 3.5 SEM image based measurements. (A) Collagen fiber straightness (B) Collagen strength of alignment (C) Collagen pixel ratio (D) Mean collagen orientation relative to the muscle fiber direction (E) Peak radon transform value per image. Significance between groups shown with bars, where p<0.05 and n=6 mice per group.

The mechanical models predicted that longitudinal effective stiffness was greater in WT mice compared to *mdx* mice, while transverse effective stiffness and the ratio of transverse to longitudinal effective stiffness was greater in *mdx* mice compared to WT mice. Variations in collagen fiber organization measured in SEM images were reflected qualitatively in the element stresses in the FE models. (**Fig. 3.6**). Longitudinal (muscle fiber direction) effective stiffness was significantly greater in WT over *mdx* at 3 months (mdx=0.143±0.0464, WT=0.268±0.0451, p=1.21e-4) and 6 months (*mdx*=0.177±0.0330, WT=0.268±0.0383, p=5.93e-3) (**Fig. 3.7C**). Transverse (cross-muscle fiber direction) effective stiffness was significantly greater in *mdx* over WT at 3 months (*mdx*=0.646±0.0826, WT=0.500±0.0699, p=6.75e-3) and 6 months (*mdx*=0.633±0.0492, WT=0.487±0.0692, p=7.15e-3) (**Fig. 3.7D**). For all SEM-image based models, the effective stiffness ratio was greater than 1, indicating greater stiffness in the direction transverse to the muscle fibers. The effective stiffness ratio was also significantly greater in *mdx* over WT at 3 months (*mdx*=5.45±2.04, WT=1.97±0.670, p=1.32e-4) and 6 months (*mdx*=4.05±0.985, WT=1.96±0.506, p=3.50e-24.6e-3) (**Fig. 3.7E**).

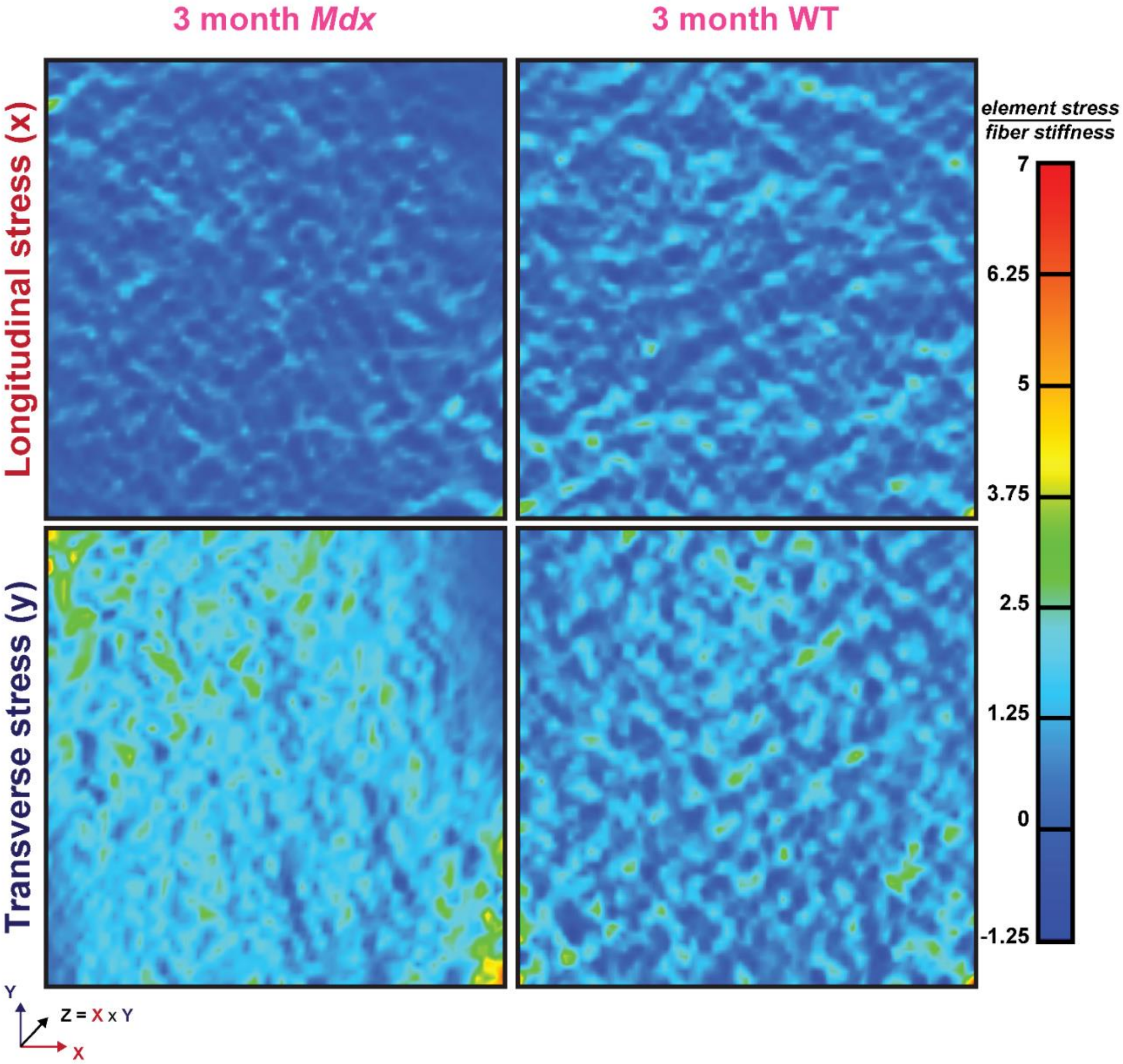

Figure 3.6 Finite-element models based on images of 3-month-old mdx and WT mice (seen in Figure 4). Element stress normalized by collagen fiber stiffness is plotted in the longitudinal/muscle-fiber (top) and transverse/cross-muscle fiber (bottom) directions.

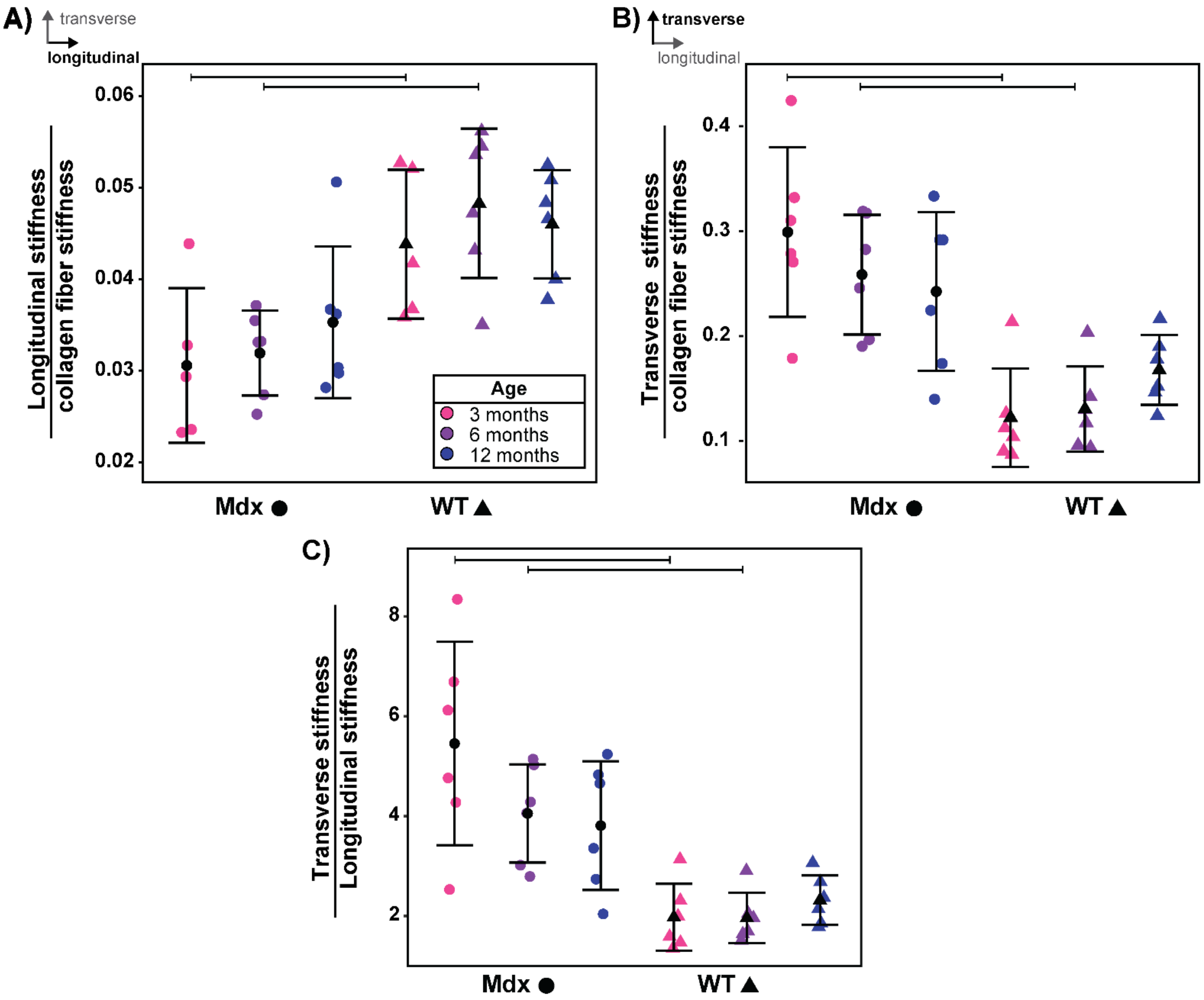

Figure 3.7: (A) Longitudinal/muscle-fiber direction effective stiffness at 20% strain, normalized by collagen fiber stiffness. (B) Transverse/cross-muscle fiber direction effective stiffness at 20% strain, normalized by collagen fiber stiffness. (C) Stiffness ratio quantified as the transverse stiffness divided by longitudinal stiffness. Significance between groups shown with bars, where p<0.05 and n=6 mice per group.

Collagen fiber straightness and collagen fiber alignment were significant predictors of SEM-image based model outputs. There were positive linear relationships between collagen fiber straightness and transverse (cross-muscle fiber direction) effective stiffness ($k_{trans}= 1.827*P_s -1.122, R^2=0.6$) and between collagen fiber alignment and transverse (cross-muscle fiber direction) effective stiffness ($k_{trans}= 1.423*R -0.5731, R^2=0.8$) (**Fig. 3.8B,C**). There were negative linear relationships between collagen fiber straightness and longitudinal (muscle fiber direction) effective stiffness ($k_{long} = -1.189 * P_s + 1.1323$, $R^2 = 0.7$) and between collagen fiber alignment and longitudinal (muscle fiber direction) effective stiffness ($k_{long} = -1.09 * R + 1.097$, $R^2 = 0.9$) (**Fig. 3.8 E,F**). The data points follow the effective stiffness ratio determined from the linear fits ($k_{ratio} = k_{trans}/k_{long}$) (**Fig. 3.8 G,H,I**). There were no significant relationships between collagen fiber direction and longitudinal or transverse effective stiffness (**Fig. 3.8 A,D,G**).

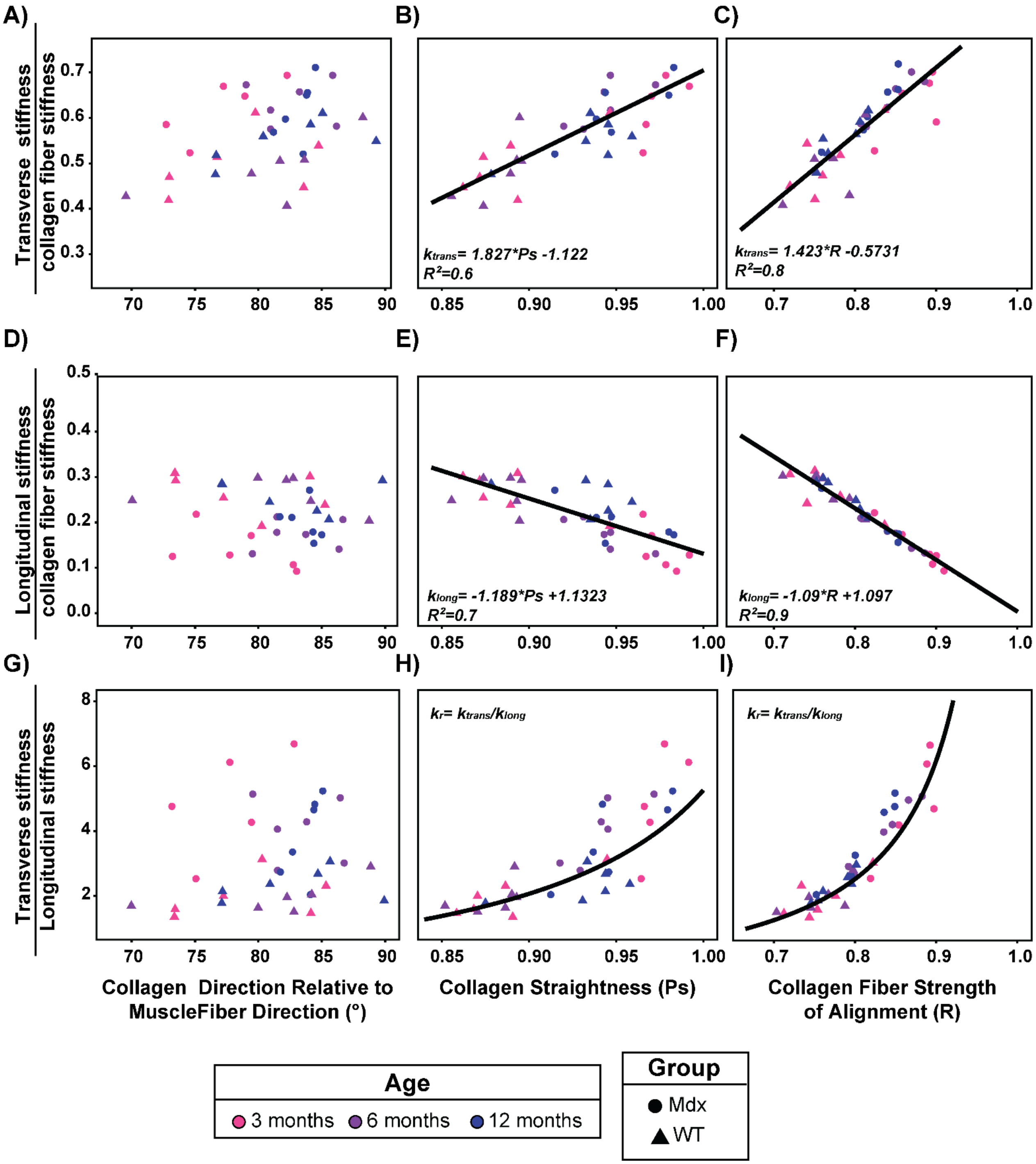

Figure 3.8 Relationships between collagen fiber organization measured from SEM images and tissue level properties predicted from mechanical models. Linear relationships for transverse/cross-muscle fiber direction and longitudinal/muscle-fiber direction stiffness vs. collagen fiber straightness and alignment were calculated with linear regression (A-F). Relationships for stiffness ratio were calculated by dividing fits for transverse stiffness (A-C) by fits for longitudinal stiffness (D-F).

Theoretical structure-function relationships between collagen fiber organization and tissue stiffness were determined from simplified image-based models. FE models based on simplified images predicted power law relationships between collagen fiber straightness and effective stiffness and exponential relationships between collagen direction and effective stiffness (**Fig. 3.9**). *Collagen fiber direction vs. effective stiffness*: The transverse (cross-muscle fiber direction) stiffness values from the SEM-image based models were better approximated by the theoretical curve with collagen fiber straightness constant at 1 (**Fig. 3.9A**). Both theoretical curves predicted lower values for longitudinal (muscle fiber direction) effective stiffness than the SEM-image based models (**Fig. 3.9C**). The effective stiffness ratio values from the SEM-image based models were better approximated by the theoretical curve with collagen fiber straightness constant at 85˚ (**Fig. 3.9E**). *Collagen fiber straightness vs. effective stiffness*: The transverse (cross-muscle fiber direction) stiffness values from the SEM-image based models were better approximated by the theoretical curve with collagen fiber direction constant at 90˚ (**Fig. 3.9B**). Both theoretical curves predicted lower values for longitudinal (muscle fiber direction) effective stiffness than the SEM-image based models (**Fig. 3.9D**). The effective stiffness ratio values from the SEM-image based models were better approximated by the theoretical curve with collagen fiber direction constant at 70˚ (**Fig. 3.9F**).

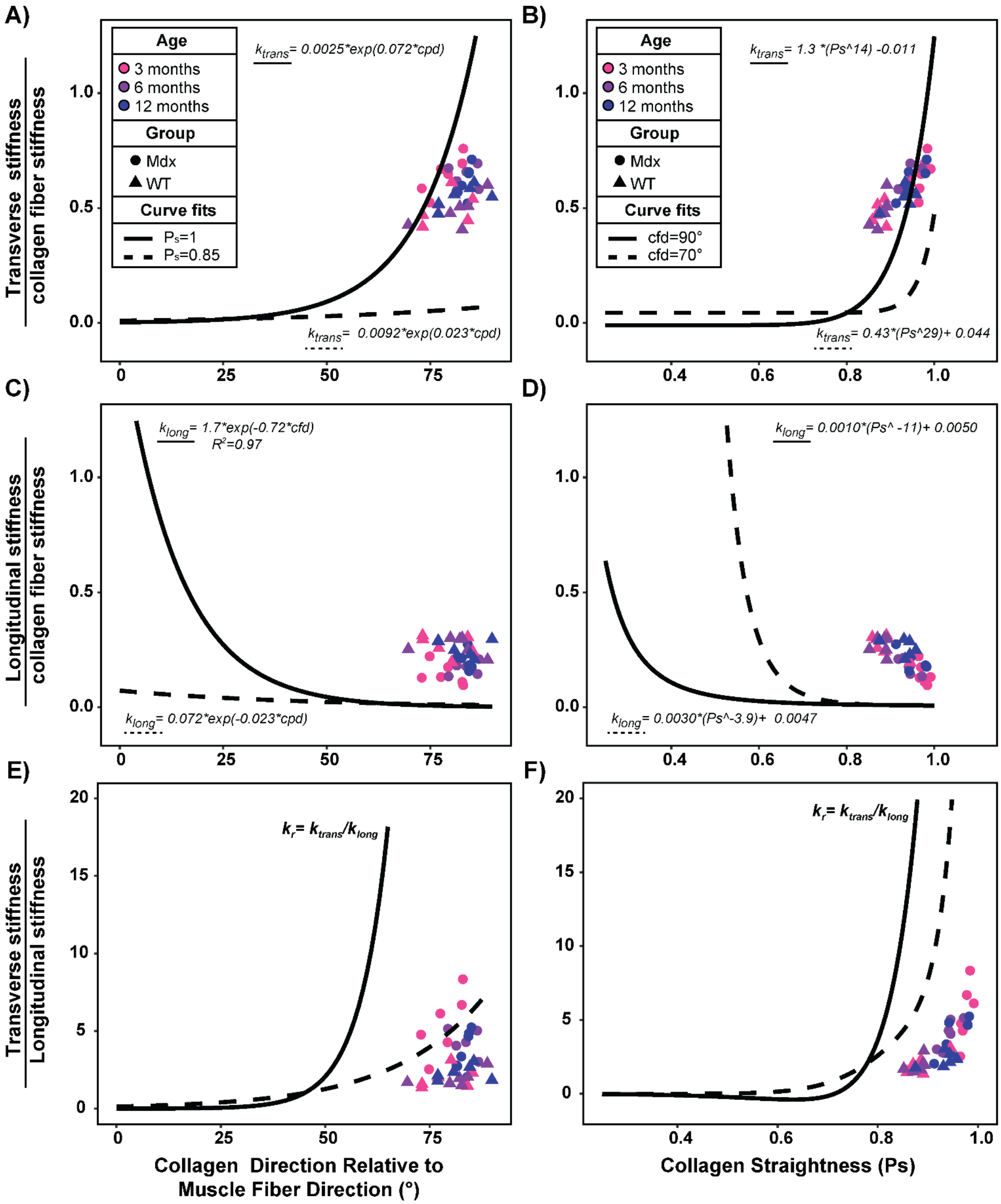

Figure 3.9: Theoretical relationships between collagen fiber organization from simplified images and tissue level properties predicted from mechanical models (see Supplemental Materials 4). Relationships for transverse and longitudinal stiffness vs. collagen fiber straightness and direction were calculated with nonlinear regression (A-D) and relationships for stiffness ratio were calculated by dividing fits for transverse stiffness (A-B) by fits for longitudinal stiffness (C-D). Power law relationships between collagen fiber straightness and model outputs with collagen direction constant at 90° (solid lines) and 70° (dashed lines) are shown in B,D,F. Exponential relationships between collagen fiber direction and model outputs with collagen fiber straightness constant at 1 (solid lines) and 0.85 (dashed lines) are shown in B,D,F. R^2>0.95 for all fits.

3.5 Discussion

In this study we tested the hypotheses that collagen structure within the ECM is altered in DMD and that these changes have implications on the mechanical properties of the ECM. We first visualized collagen structure with SEM images and then developed an analysis framework to quantify collagen organization and explore the influence of our measurements on ECM mechanics (**Fig. 3.1-3.3**). The image analysis reveals that collagen fibers within the diaphragm muscle epimysium are oriented transversely, with increased collagen fiber straightness and alignment with age and disease (**Fig. 3.5**). From the SEM image-based mechanical models, we predict that transverse (cross-muscle fiber direction) effective stiffness is also increased with age and disease. Additionally, both healthy and diseased models reveal an increase in transverse (cross-muscle fiber direction) effective stiffness relative to longitudinal (muscle fiber direction) effective stiffness, with the ratio of transverse to longitudinal effective stiffness increased with disease (**Fig. 3.7**). Collagen fiber straightness and alignment measured in the SEM images were significant predictors of transverse and longitudinal stiffness output from our models, while collagen direction was not (**Fig. 3.8**). From the models based on simplified images, we predict theoretical power law relationships between collagen fiber straightness and effective stiffness and theoretical exponential relationships between collagen direction and effective stiffness (**Fig. 3.9**).

Our findings implicate changes in ECM structure and mechanics on the mechanical properties of diaphragm muscle. As DMD progresses in patients, pulmonary function declines[36] as the diaphragm muscle weakens with age.[37,38] To understand how tissue level properties lead to changes in muscle function, animal models such as the *mdx* mouse allow us to measure tissue properties with disease. Mechanical properties of diaphragm muscle are often measured from uniaxial strip tests and show a decrease in elasticity and contractile force in *mdx* diaphragm.[12,105] However, unlike most skeletal muscles, the diaphragm sustains biaxial loads *in vivo* and exhibits nonuniform and anisotropic behavior.[61,62,106] From uniaxial tests of rat diaphragm muscle, Boriek et al. report that extensibility of diaphragm tissue is decreased when loaded uniaxially transverse to muscle fibers, than when loaded uniaxially along muscle fibers.[62] From biaxial tests of healthy canine diaphragm muscle, Boriek et al. reported that samples were stiffer and more non-linear transverse to muscle fibers than along the muscle fiber direction.[61] In our models, we simulated a 20% equibiaxial test and predicted that both healthy and *mdx* tissue was stiffer transverse to the muscle fiber direction, similar to Boriek et al.'s findings.[61] While our models of healthy murine tissue predicted about a two times increase in transverse relative to longitudinal stress, Boriek et al. reported about a five times increase in transverse to longitudinal stress in healthy canine tissue at 20% longitudinal strain when a load corresponding to 20% transverse strain was applied. Differences in the experimental conditions and animal models may account for the decreased stiffness ratio predicted in our healthy models and future studies in murine diaphragm tissue are needed to make direct comparisons with our model predictions.

In our study we only modeled the ECM, focusing on the effects of collagen organization, and found that WT tissue was stiffer than *mdx* in the longitudinal direction. Indeed, previous studies report that longitudinal muscle stiffness is greater in *mdx* tissue than WT and Stedman et al. reported that the dynamic elastic modulus of *mdx* diaphragm muscle was more than 30 times greater than WT[12]. Although we expect that in *mdx* muscle tissue both longitudinal and transverse stiffness are greater than in WT muscle tissue, we posit that the increase in transverse passive stiffness is due to the organization of collagen fibers. Surprisingly, Smith et al. did not find any significant differences in longitudinal passive stiffness in *mdx* and healthy diaphragm muscle tissue although collagen area fraction was approximately four times greater in *mdx* relative to WT mice at 12 months.[14] Based on the findings presented here, the increase in collagen amount may play a larger role on the transverse properties in the diaphragm muscle, requiring biaxial mechanical testing to elucidate the role of collagen on passive mechanics.

The methods presented here offer a novel framework to explicitly model the influence of ECM structure on mechanical properties. In a previous constitutive model of epimysium from rat tibialis anterior muscle[107], Gao et al represented collagen fibers with unit cells and assigned unit cell angle from collagen fiber distributions that were measured experimentally[25] but were not specific to the epimysium. In the image-based modeling pipeline presented here, we explicitly modeled collagen organization by assigning fiber directions in each finite element, allowing for a framework that can be easily translated. In the SEM images, we found an increase in collagen fiber straightness in older healthy mice relative to younger healthy mice (**Fig. 3.5A**), but this difference was not reflected in the model predictions (**Fig. 3.7**). In both images and models, we did not find any differences between diseased and healthy groups at 12 months, suggesting that the ECM of older healthy mice resembles that of diseased mice. A benefit of our modeling pipeline is that we can relate collagen fiber-level structural parameters to tissue-level mechanical parameters to predict structure-function relationships. In the models based on SEM images, significant relationships were seen between collagen fiber straightness and alignment with effective stiffness, but not collagen fiber direction (**Fig. 3.8**). Theoretically, we would expect collagen fiber direction to be an important predictor of tissue properties and the models based on simplified images show an exponential relationship between collagen direction and tissue stiffness (**Fig. 3.9**). However, in the SEM-image based models collagen direction was not a dominant factor in distinguishing the properties across samples. This may be due to the fact that collagen fiber direction did not vary greatly between the tissue samples or because collagen alignment and straightness accounted for key differences between samples and had a greater impact on stiffness. For all SEM image-based models, the effective stiffness was greater in the transverse/cross-muscle fiber direction relative to longitudinal/muscle-fiber direction ($k_r > 1$), and collagen fibers were oriented in the transverse direction. Taken together, these findings suggest that although collagen fiber direction determines the direction in which the ECM will be stiffer in tension, collagen fiber straightness and alignment explain differences in model predictions for *mdx* and WT mice. Another advantage of the methods presented here is that we can isolate structural parameters using simplified images and predict “theoretical” structure-function relationships from our FE models. By comparing these theoretical curves with the SEM image-based models, we can see that accounting for collagen fiber direction or collagen fiber straightness alone is not sufficient for explaining the changes in tissue level properties we predicted with age and disease in our FE models. This suggests that there is isotropy beyond changes in collagen fiber straightness or direction that play a role in distrusting stresses throughout the ECM.

There are some limitations of this approach that should be mentioned. Enzymatic and detergent digestions such as the sodium hydroxide protocol used in this study have been shown to alter the mechanical properties of the ECM.[42] While this is what motivated us to use modeling to explore the mechanical implications of the ECM, changes in the structure of collagen fibers may have been influenced by removing all other ECM components. As chemical fixation has been shown to lead to tissue shrinkage, [108] there may have been shrinkage in our diaphragm muscle samples before isolating the ECM, as well as during the dehydration preparation for SEM imaging. This tissue shrinkage may have influenced the straightness of collagen fibers, possibly increasing the waviness we detected. Since all samples underwent the same protocol, we assume that these influences were constant between groups.

All samples were physically unconstrained throughout the duration of our protocol. Our images were captured after muscle fibers and additional ECM components were digested, leaving only the collagen fibers. Although all samples were imaged with the epimysium in a stress-free configuration, the collagen fibers may still have some form of stress and we cannot directly relate this configuration to *in vivo* muscle fiber lengths. Collagen fiber angle is known to vary with muscle fiber length, with collagen becoming more aligned with muscle fibers at greater sarcomere lengths.[109] Therefore, the transverse collagen fibers we measured in our samples may reflect their position at shorter sarcomere lengths. As collagen becomes more aligned with the muscle fiber direction at greater sarcomere lengths, the wavier collagen fibers may allow for more lengthening while the straighter fibers may prevent longer muscle fiber lengths from being achieved. Henry et al. reported a decrease in “resting” sarcomere length in *mdx* diaphragm muscle relative to WT,[45] suggesting that they operate on different regions of the force-length curve. Based on our findings, we posit that the straighter collagen fibers measured in our *mdx* samples may contribute to this leftward shift on the force-length curve.

In the FE models, we grouped all collagen subtypes in one material and did not account for changes in other ECM components or crosslinking of collagen fibers, although increased collagen crossing linking has been previously reported in *mdx* mouse diaphragm tissue and muscle from patients with DMD.[54] For this reason, it is important to acknowledge that the results presented in this work focus on the effects of collagen fiber organization alone. Additionally, we did not measure mechanical properties of our decellularized samples directly. While simplistic, this allowed us to focus specifically on relating structural parameters at the collagen fiber level to bulk level tissue properties. Thus, the modeling results presented here are theoretical in nature and provide interesting hypotheses for future experiments to examine changes in passive mechanics of the dystrophic diaphragm.

The skeletal muscle ECM is a complex three-dimensional scaffold that is organized uniquely across muscle groups. Skeletal muscle fibrosis is often characterized with images of muscle cross-sections showing a honeycomb structure of the perimysium, surrounding muscle fascicles, and endomysium, surrounding muscle fibers.[25–27] The structure of the endomysium is similar across skeletal muscles,[28] while differences in perimysium and epimysium are reported across muscle groups and with disease. Borg et. al report that perimysium from diaphragm muscle is less developed than other skeletal muscle groups where large bundles of collagen fibers are seen, arranged both parallel and circumferential to muscle fibers.[28] An increase in the number of such "perimysial collagen cables" has been reported with fibrosis, [110] but their prevalence in diaphragm muscle fibrosis remains unknown. In our study, we collected images of the diaphragm muscle epimysium, the outermost layer of the ECM surrounding skeletal muscle. Differences in the structure of the epimysium are also reported across skeletal muscles, where a cross-ply arrangement of wavy collagen fibers oriented approximately 55° to the muscle fiber direction is reported in long strap-like muscle and a dense layer of collagen fibers aligned parallel to muscle fibers is reported in pennate muscle.[26] These muscles sustain uniaxial loads *in vivo*, and thus collagen fibers aligned with the muscle fiber direction may mainly contribute to the longitudinal, or along muscle fiber properties. Gao et al. report that the outer layer of the epimysium in rat tibialis anterior muscle consists of wavy collagen fibers highly aligned in a "predominant direction" but do not report the direction relative to muscle fiber direction or quantify collagen alignment or straightness.[111] Our SEM images show a similar arrangement to Gao at al. in the diaphragm muscle epimysium, but with collagen fibers oriented transverse to muscle fibers. As the diaphragm sustains biaxial loads *in vivo,* this suggests that the epimysium may mainly contribute to its transverse, or cross-muscle fiber properties. We hypothesize that the arrangement of collagen fibers we measured in the epimysium is unique to the diaphragm muscle and highlights the need to study the arrangement of collagen fibers in each muscle before we can determine how changes during fibrosis affect its mechanical properties.

Compared to other skeletal muscles, the diaphragm is thin and relatively flat with a larger surface to volume ratio. Thus, the epimysium spans a greater area as it is continuous with the surface of the diaphragm muscle and may be responsible for bearing a greater amount of load relative to the peri- and endomysium. Griffiths et al. report the presence of an elastin rich layer of connective tissue on the thoracic surface of sheep diaphragm muscle, which provides elastic recoil and reduces stress on the diaphragm muscle.[112] A similar structure has not been reported in mouse diaphragm muscle, nor did we notice the presence of one during our muscle isolation. However, the epimysium may serve a similar purpose and the increased collagen fiber straightness and alignment we measured in *mdx* epimysium may increase stress on the diaphragm muscle. Although the epimysium may play a larger role in the diaphragm muscle, future studies are still needed to explore changes in collagen organization within the intramuscular ECM layers. Prior studies report that the endomysium is composed of a planar network of irregularly wavy collagen fibers,[25,26] and thus the changes in alignment and straightness that we measured in the epimysium may also be implicated in these layers in the diaphragm muscle.

The skeletal muscle ECM is essential for transmitting forces from muscle fibers. Muscle fibers can transmit force both longitudinally along the muscle fiber axis, and laterally to adjacent muscle fibers.[113–115] Lateral force transmission occurs through physical linkages between the actin cytoskeleton and ECM at the muscle fiber membrane.[18] This notion is supported by the ability of the endomysium to transmit forces between intrafascicularly terminating muscle fibers through shear[115] and the physical continuity of the perimysium from muscle to tendon.[20] Huijing et al. describe “epimuscular myofascial force transmission” as the force transmitted between muscle and its surroundings through the epimsuyim.[19] This idea is supported through experiments where force transmission still occurs after tendonotomy[116,117] and differences in proximal and distal force are measured when the muscle-tendon complex length is held constant.[118] Such experiments provide strong evidence of force transmission through pathways other than the myotendinous junctions and highlight the role of the ECM. Damage to connective tissue is shown to hinder force transmission and we must consider how fibrosis affects the ability of the ECM to transmit forces.[118] In *mdx* mice, where the muscle fiber membrane is weakened due to the lack of dystrophin, lateral force transmission is severely impaired.[114] The diaphragm muscle has a complex architecture with a majority of intrafascicularly terminating muscle fibers,[119] suggesting that the ECM is especially critical for lateral force transmission. The SEM images in this study revealed that collagen fibers are oriented transverse to the muscle fibers, suggesting that they may serve as a direct pathway for transmitting forces laterally between muscle fibers. Thus, changes in the alignment or straightness of these transversely oriented collagen fibers may influence the ability of the ECM to transmit lateral forces between neighboring muscle fibers of from muscle fibers to tendon.

We must consider the role of collagen organization on respiratory insufficiency in DMD. To hypothesize the implications of our findings on respiration we must first consider the unique architecture of the diaphragm muscle. The diaphragm is a dome shaped, “sheet-like” muscle, with a central tendon connecting to the costal and crural muscle domains.[120] In our study, we collected samples from the costal region. In this region, the muscle fibers are arranged radially from the central tendon to insertion at the rib cage. Therefore, if we consider our results at the whole-muscle level we expect that collagen fibers are arranged circumferentially to maintain the transverse orientation we measured at high magnifications. Collagen fibers are responsible for generating force when stretched in tension, implicating that the epimysium limits circumferential expansion of the diaphragm muscle. This suggests that the epimysium may regulate the ability for the diaphragm muscle to return to its fully relaxed configuration during expiration, preventing it from moving through the proper excursion lengths contributing to insufficiency. To better understand the mechanical role of the epimysium on respiratory insufficiency we must characterize the changes in biaxial properties of diaphragm muscle with fibrosis and develop methods to quantify *in vivo* motion of the diaphragm during respiration.

Future work should consider the unique structure and mechanics of fibrotic tissue in therapies for DMD. Despite progress in recent years, DMD remains a fatal condition, with fibrosis a key contributor to muscle dysfunction and hypothesized to decrease the effectiveness of therapeutics. Anti-fibrotic therapies target inflammatory pathways such as TGF-β, but their effectiveness is measured by decreasing levels of collagen expression, without accounting for changes in ECM structure or mechancis.[121,122] The importance of mechanical and structural properties of the ECM is well documented in the literature, with ECM stiffness and alignment key regulators of cellular behaviors involved in fibrosis, such as fibroblast alignment, migration, and proliferation.[49,50] Our study reveals changes in both ECM structure and mechanics in fibrosis, highlighting the need to study the role of therapeutics on collagen organization. Further, we must account for differences in collagen organization between tissue systems, especially as we aim to alleviate the deleterious impacts of fibrosis in DMD in the diaphragm muscle.

Acknowledgements

We are grateful to Dr. David Sleboda for guidance on the enzymatic digestion protocol used in this study. We would also like to thank the Advanced Microscopy Facility at the University of Virginia for their support for the imaging conducted in this study. Funding for this work was provided by Grant U01AR06393 from the National Institutes of Health, and a graduate fellowship from a T32 Biotechnology Training Grant.

3.6 Glossary of Terms

Longitudinal/muscle fiber direction: direction of muscle fibers, aligned with the horizontal axes

Transverse/cross muscle fiber direction: direction transverse to muscle fiber direction, aligned with vertical axes

Collagen fiber direction ($0° < cfd < 90°$): average of collagen fiber directions measured in each image subregion reported relative to muscle fiber direction, automatically output from image processing algorithm

Collagen fiber straightness ($0 < P_s < 1$): straightness of collagen fibers ($P_s = L_o / L_f$,), where L_o = linear end-to-end straight-line length of collagen fiber and L_f,=collagen fiber path length, measured manually in ImageJ

Collagen fiber strength of alignment ($0 < SA < 1$, 1=high alignment): alignment of collagen fibers across image subregions calculated from resultant vector length ($SA = \|\bar{\boldsymbol{r}}\|$), automatically output from image processing algorithm

Transverse effective stiffness (k_{trans}): tissue-level stiffness in the cross-muscle fiber direction calculated from mechanical models at 20% applied biaxial strain

Longitudinal effective stiffness (k_{long}): tissue-level stiffness in the muscle fiber direction calculated from mechanical models at 20% applied biaxial strain

Effective stiffness ratio: transverse effective stiffness divided by longitudinal effective stiffness ($k_{ratio} = k_{trans} / k_{long}$

Chapter 4

It’s more than the amount that counts- implications of collagen organization on passive muscle tissue properties revealed with multiscale mechanical models and experiments.

Acknowledgements: Kaitlyn Hixson, Silvia S. Blemker

The middle is messy,

but it’s also where the magic happens.

—Brenè Brown

4.1 Abstract

Collagen accumulation is often used to characterize skeletal muscle fibrosis, but collagens' role in passive muscle mechanics remains debated. Here we combined multiscale finite element models and experiments to examine how collagen organization contributes to macroscopic muscle tissue properties. Tissue microstructure and mechanical properties were measured from *in vitro* biaxial experiments and imaging in dystrophin knockout (*mdx*) and WT diaphragm muscle. Micromechanical models of intramuscular and epimuscular extracellular matrix (ECM) regions were developed to account for complex microstructure and predict bulk properties, and directly calibrated and validated with the experiments. The models predicted that intramuscular collagen fibers align primarily in the cross-muscle fiber direction, with greater cross-muscle fiber alignment in *mdx* models compared with WT. Higher cross-muscle fiber stiffness was predicted in *mdx* models compared with WT models and differences between ECM and muscle properties were seen during cross-muscle fiber loading. Analysis of the models revealed that variation in collagen fiber distribution had a much more substantial impact on tissue stiffness than ECM area fraction. Taken together, we conclude that collagen organization explains anisotropic tissue properties observed in the diaphragm muscle and provides an explanation for the lack of correlation between collagen amount and tissue stiffness across experimental studies.

KEYWORDS: collagen organization, passive muscle properties, biomechanics

4.2 Introduction

The development of fibrosis leads to muscle dysfunction in several neuromuscular disorders and impairments. As healthy muscle is replaced by noncontractile fibrotic tissue, increased passive stiffness contributes to decreased mobility and quality of life. An accumulation of collagen is often used to characterize fibrosis, simplifying the complex microstructure of collagen fibers within the extracellular matrix (ECM). The ECM is as a key contributor to passive muscle properties[123] and transmits both physical and chemical signals within muscle tissue.[18–20] The epimysium (epimuscular ECM) surrounds the outermost surface of skeletal muscle, and the perimysium and endomysium (intramuscular ECM) separate muscle fascicles and muscle fibers.[25–27] Collagen fibers regulate the structure and tensile properties of the ECM, with unique collagen arrangements reported across muscle groups and between ECM layers.[26,111] However, the relationship between ECM structure and muscle function remains poorly understood, particularly in complex muscles such as the diaphragm, which is severely affected in progressive muscle diseases such as Duchenne muscular dystrophy (DMD). [80,124]

The diaphragm muscle is anisotropic, with higher tissue stiffness in the direction perpendicular to muscle fibers as compared to the stiffness along muscle fibers.[61–63] Interestingly, while the dystrophin knockout mouse model (*mdx*) exhibits notable increases in fibrosis in the diaphragm (as in humans),[12,45,81,124] the amount of collagen only exhibits a minimal correlation with diaphragm passive muscle tissue stiffness.[14] Previous experiments found higher along- and cross-muscle fiber tissue stiffness in *mdx* relative to WT diaphragm (from biaxial tests)[64] and higher along-muscle fiber tissue stiffness in *D2.mdx* relative to WT diaphragm (from uniaxial tests),[60] but these differences were no longer observed after enzymatically digesting collagen.[60,64] While the collagenase impacted tissue stiffness, it did not affect collagen content (measured by collagen solubility assay)[60] and had a minimal impact on collagen area fraction (measured with imaging),[64] suggesting that alterations in collagen microstructure during enzymatic digestion contribute to the loss of stiffness. Indeed, increased intramuscular collagen fiber alignment relates to increased passive stiffness in *mdx* lower limb muscle,[125] and distinct relationships between intramuscular collagen alignment and stiffness are observed across muscle groups.[126] Similarly, we previously observed changes in epimuscular ECM of diaphragm muscle tissue in *mdx* compared to WT mice that also has implications on tissue stiffness.[127] Taken together, it is clear that it is more than the amount that matters, leading us to the following question: do variations in collagen organization in ECM layers explain why collagen amount does not correlate with muscle tissue stiffness in *mdx* diaphragm?

The above question is very challenging to answer through experiments alone; however, computational modeling empowers us to precisely examine how microstructural variations contribute to macroscopic tissue properties. For example, previous micromechanical models generated from images of muscle cross-sections revealed how fascicle cross-sectional morphology influences the transversely anisotropic behavior at the tissue level.[15] Furthermore, micromechanical models created using Voronoi tessellation to replicate muscle fiber geometries[71] examined how variations in structure along the muscle fiber direction influence shear properties,[74] how the ECM mediates strain propagation from damaged fibers,[128] and how changes in connective tissue with aging influence macroscopic muscle force.[75] Micromechanical models that simulated changes in microstructure seen in DMD found that the effect of increased ECM area fraction was highly dependent on the stiffness of the ECM.[76] These previous models provided key insights, but simplify the representation of the ECM as isotropic,[128] transversely isotropic aligned with muscle fibers,[15,76] or use a generalized helical assumption to represent collagen direction.[71,74,75] Therefore, they do not account for distinct ECM layers or incorporate the ability to examine the role of changes in collagen microstructure on muscle tissue properties. These models also rely on integrating measurements from several studies across different skeletal muscle groups,[71,74,75,128] so it would be impossible to use these models to answer specific questions about variations in the structure and function of a particular muscle.

Here we introduce a novel framework that couples experimental measurements with multiscale finite element models to examine how microstructural variations account for measured differences in macroscopic tissue properties. Specifically, the goals of our study were to (1) measure diaphragm muscle tissue structure using imaging and biaxial mechanical properties in *mdx* and WT mice, (2) develop, calibrate, and validate a modeling framework that relates the multiple layers of ECM microstructure to bulk muscle tissue properties, and (3) predict how changes in tissue microstructure contribute to impairments during disease.

4.3 Methods

Our framework combines experimental measurements of tissue microstructure and mechanical properties with multiscale finite element models to investigate how collagen organization within the epimuscular and intramuscular ECM influences skeletal muscle tissue properties (**Fig 4.1**). All experiments were conducted in diaphragm muscle tissue from 6-month-old *mdx* and WT mice and used to develop *mdx* and WT models. Micromechanical models of intramuscular and epimuscular regions were developed to account for complex microstructure and coupled to predict bulk muscle tissue properties. *In vitro* biaxial experiments were performed to measure bulk tissue stresses and stiffness for model calibration and validation. Imaging measurements were collected to determine tissue microstructure to initialize the intramuscular model geometries and couple the intramuscular and epimuscular model predictions.

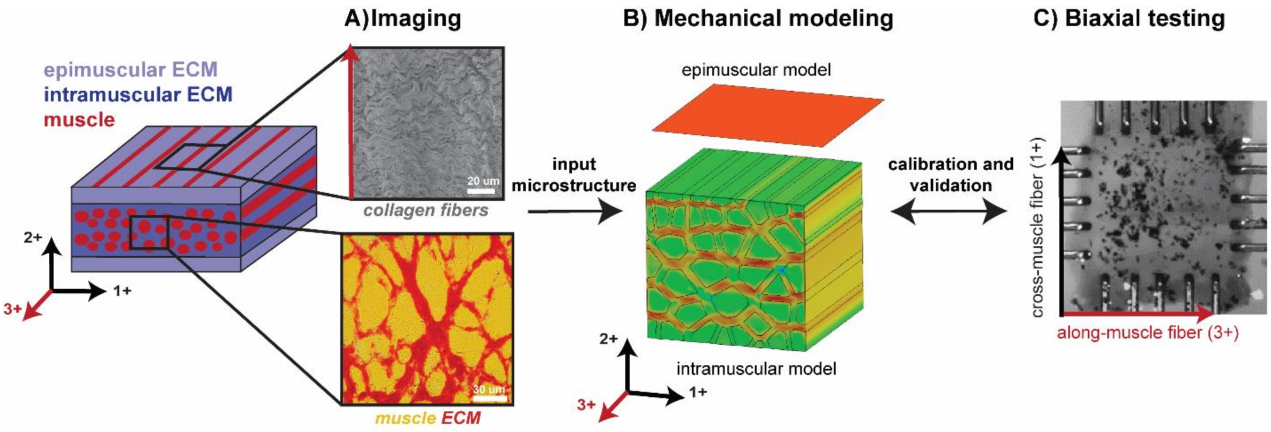

Figure 4.1: Overview of coupled framework leveraging imaging (A), mechanical modeling (B) and biaxial testing (C).

4.3.1 *In vitro* biaxial mechanical testing

All experiments were approved by the University of Virginia Animal Care and Use Committee and conducted in C57BL/10ScSn-Dmdmdx/J male mice (*mdx*), and C57BL/6J male mice (WT), purchased from Jackson Laboratories (n=6 WT, n=5 *mdx*). Mice were humanely euthanized with CO_2 and cervical dislocation. Incisions were made above and below the xiphoid process of the sternum to allow pressure to equalize. The entire diaphragm muscle was then excised along with its attachments to the ribs and placed in a chilled 30mM solution of 2,3-butanedione monoxime (BDM) to prevent actin-myosin crossbridge formation. A 5x5 mm sample was dissected from the costal region on the right side of diaphragm muscle while keeping the whole diaphragm muscle pinned to maintain its length. The excised sample was loaded into a Cell Scale Biotester (CellScale, Waterloo, Canada) such that the 3+ direction corresponded to the longitudinal/muscle fiber direction and 1+ direction corresponded to the transverse/cross-muscle fiber direction (**Fig 4.2A**). The sample was speckled with graphite powder for strain tracking analysis and lowered into BDM solution for the duration of the testing. The tissue was preloaded to 10mN in both directions and tested in four loading conditions. The first condition simulated muscle contraction by applying 5% along-muscle fiber shortening and 5% cross-muscle fiber lengthening (*in vivo*). The second condition prescribed 10% equibiaxial along- and cross muscle fiber lengthening (biax). The third condition applied 10% uniaxial lengthening in the along-muscle fiber direction (uniax along). The fourth condition applied 10% uniaxial lengthening in the cross-muscle fiber direction (uniax cross) (**Fig 4.2B**). Five cycles of each stretch condition were applied, and the final cycle was analyzed to minimize the effects of viscoelastic behavior. A contralateral sample from the left side of diaphragm muscle was dissected and used to measure thickness with a laser displacement sensor (Keyence, Itasca, IL). Thickness was measured in nine evenly spaced locations and averaged. The sample was then placed in optimal cutting temperature solution and snap frozen in liquid nitrogen cooled isopentane for imaging. We assumed symmetry between the two halves of the diaphragm, as differences in microstructure are not observed between the left and right sides.[45,129]

Images of the tissue sample were collected during the duration of the test and used for strain tracking analysis. Digital image correlation was performed to obtain the deformation gradient (F)[130] and determine the components corresponding to deformation in the along and cross-muscle fiber directions (F^{11}, F^{33}, F^{13}, F^{31}). Lagrangian strain (E) was then calculated with the following equation:

$$\mathrm{E} = \frac{1}{2}(F^T F - I)$$

Equation 4.1

Along- (A_3) and cross- (A_1) muscle fiber cross-sectional tissue areas were calculated using the measured tissue thickness and sample length and widths recorded during testing. Along (f_3) and cross (f_1) muscle fiber force-displacement data was output from the Biotester and an exponential curve was fit to the data to resample the force data and filter out noise. Along-muscle fiber (t_{33}) and cross-muscle fiber (t_{11}) Cauchy stresses were calculated with the following equation:

$$t_{11} = \frac{f_1}{A_1}\sqrt{F_{11}^2 + F_{13}^2},\ \ t_{33} = \frac{f_3}{A_3}\sqrt{F_{33}^2 + F_{31}^2}$$

Equation 4.2

For each sample, tissue stress and strain values were plotted and resampled with an exponential function. A linear fit was calculated using three points near the specified strain value and used to calculate stress and stiffness (**Fig 4.2C**). For the *in vivo* condition, along- and cross-muscle fiber stress was analyzed at 1% cross-muscle fiber tissue strain. For the biaxial and uniaxial conditions, along- and cross- muscle fiber stresses were both analyzed at 3.5% along- or cross muscle fiber strain.

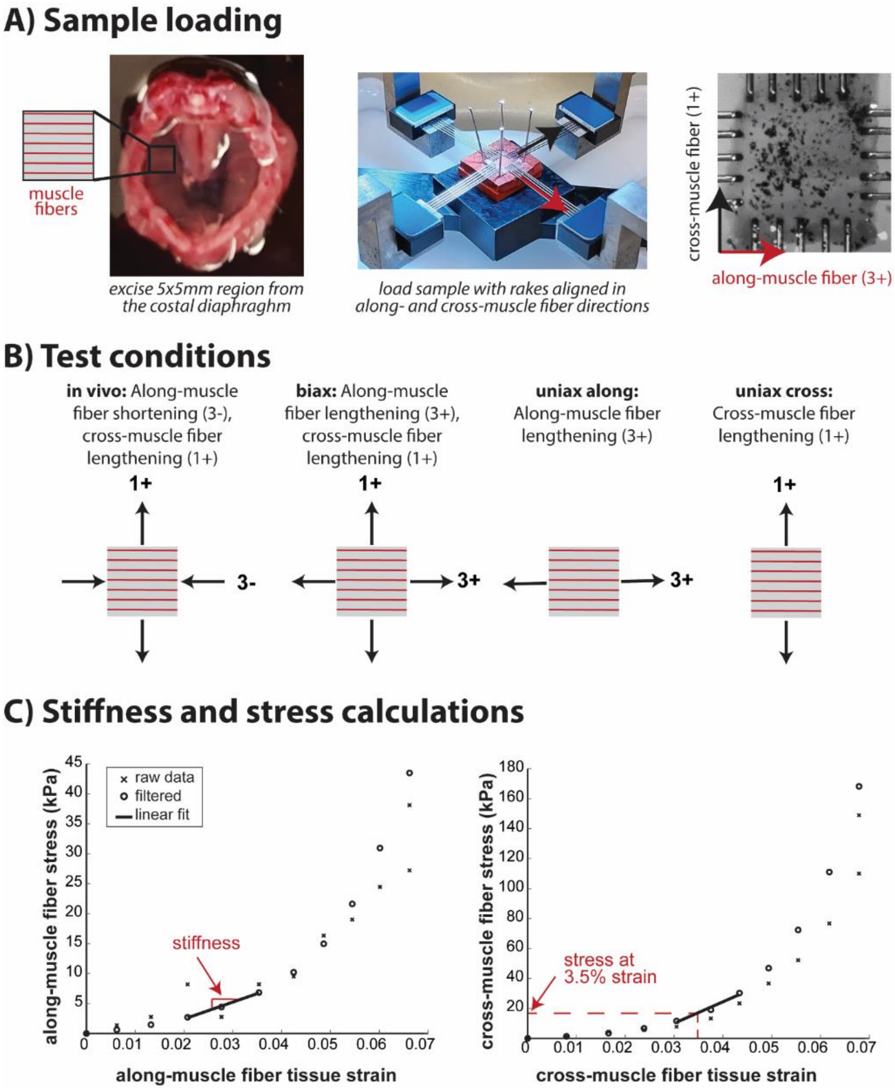

Figure 4.2 Overview of in vitro *biaxial mechanical testing. (A) A 5x5mm sample of diaphragm muscle tissue was excised from the costal region and loaded into the Biotester. Rakes were attached to align with the along-muscle fiber (3+) and cross-muscle fiber (1+) directions. (B) Samples underwent four loading conditions: (1) 5% along-muscle fiber shortening and 5% cross-muscle fiber lengthening (in vivo), (2) 10% equibiaxial along- and cross muscle fiber lengthening (biax), (3) 10% uniaxial along-muscle fiber lengthening (uniax along), (4) 10% uniaxial cross-muscle fiber lengthening (uniax cross). (C) For each sample, raw tissue stress and strain values were plotted (x) and resampled with an exponential function (o). A linear fit was calculated using three points near the specified strain value and used to calculate stress and stiffness.*

4.3.2 *Ex vivo* imaging of tissue microstructure

Snap frozen tissue samples were cryosectioned perpendicular to the muscle fiber direction to obtain 15µm thick cross-sections and mounted onto microscope slides. Slides were air dried for 20 mins and then fixed with ice cold acetone for 30 mins. Picrosirius red staining was performed with the following steps: 1) Rehydrate with 100%, 95%, and 70% EtOH (3 min each) and rinse in deionized H_20 (1 min). 2) Incubate with picrosirius red solution (60 min) followed by 0.1N hydrochloride acid (2 min). 3) Rinse with deionized H_2O (1 min) and dehydrate in 70% EtOH (30 sec), 95% EtOH (3 min), and 100% EtOH (6 min). 4) Incubate with Xylene (6 min), seal with cytoseal, and coverslip. Samples were then imaged under brightfield (BF) to visualize ECM (red) and muscle (yellow) regions and a custom code was written to determine image measurements (MATLAB). First, the outer border of the sample and the border of the intramuscular area were manually traced to create separate masks for the total sample (M^{sample}), intramuscular region (M^{intra}), and epimuscular region ($M^{epi} = M^{sample} - M^{intra}$). The areas of each region (a^{sample}, a^{intra}, a^{epi}) were calculated by summing the number of pixels (n_{pixels}) within each mask. The RGB image was converted to HSV color space and ECM pixels were identified as pixels within a specified range of red hue values (0<h<0.077, 0.094<h<1). ECM area fraction was then calculated for each region independently ($ECM_{af}^{sample}, ECM_{af}^{intra}, ECM_{af}^{epi}$) by summing the number of ECM pixels (n_{ECM}) within each mask, and dividing by the area of each region. All measurements were averaged across *mdx* and WT samples (n= 4 WT, 3 *mdx*). For one image per group a 150x150 µm region was selected and manually segmented (MATLAB Image Segmentation App) to outline muscle fiber boundaries for the intramuscular model geometries (n=1 WT, 1 *mdx*).

4.3.3 *In silico* micromechanical finite element modeling framework

The diaphragm muscle has a thin and flat structure where the epimuscular ECM covers its thoracic and abdominal surfaces, with an intramuscular layer of muscle fibers and ECM. During axial loading along the muscle fiber (3) and cross-muscle fiber directions (1), we assume these layers act in parallel. This assumption allows us to implement the Voigt model[131] to calculate the bulk muscle tissue stresses based on the stresses in each layer and their relative thicknesses. Therefore, we created separate models of intramuscular and epimuscular regions to account for their unique complex microstructures and then coupled their outputs to predict bulk tissue properties.

Model geometries: Epimuscular models represented a 100x100x1µm region of ECM from the ECM layers surrounding the diaphragm muscle. Models were generated in FeBio (Musculoskeletal Research Laboratories, University of Utah, Salt Lake City, UT, USA) and meshed with 10x10x1 hexahedral elements.[127]

Intramuscular models represented a 150x150x150µm region of muscle fibers and ECM from the middle of the thickness of the diaphragm muscle. A custom code was developed in MATLAB to generate models. Muscle fiber boundaries from the cropped 150x150µm picrosirius red images were used for model initialization (**Fig 4.3A**). The segmented image was binarized and repeated in a 3x3 grid to create a periodic geometry[71] (**Fig 4.3B**). Centroids were defined within each muscle fiber and used as seed points for Voronoi tessellation. The tessellation generated polygons based on the number and positions of the muscle centroids and was bounded to the inner 150x150 µm region. Polygon vertices were then modified to define both ECM and muscle regions. For each polygon, vertices were moved inward towards the muscle centroid based on a prescribed ratio of the initial distance that defined the ECM thickness. This thickness was defined to match ECM area fractions measured from the segmented image. Periodicity was ensured by averaging the x locations of nodes of the left and right edges, and the y locations of nodes on the top and bottom edges (**Fig 4.3C**). An initial surface mesh was defined with Delaunay triangulation using the updated muscle and ECM vertices and mesh density was refined by adding centroids within each muscle triangle and repeating the triangulation. The mesh density was further refined by defining new centroids within both ECM and muscle triangles and repeating the triangulation (**Fig 4.3D**). Vertices from the final triangulation were used to define surface nodes and repeated along the muscle fiber direction (3+) to generate pentahedral elements. The number and thickness of elements was defined to maintain the average aspect ratio of the elements ($n_z = \sqrt{n_{front}}$) and the length along the z dimension ($\ell_1 = \ell_2 = \ell_3$). Elements were defined as either muscle or ECM based whether triangle vertices fell within muscle polygons from the surface mesh (**Fig 4.4**).

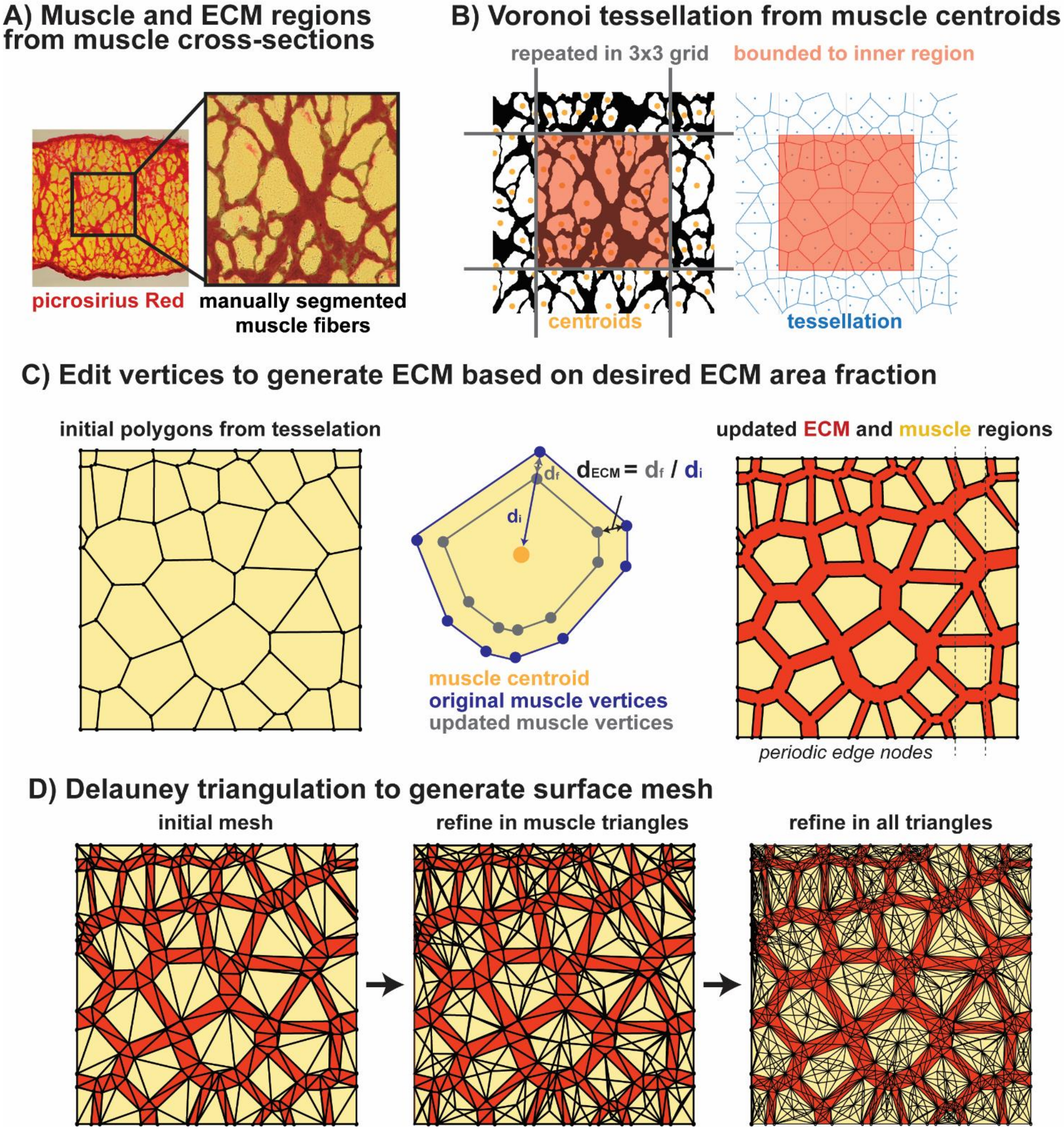

*Figure 4.3***:** *Overview of intramuscular model generation shown with example mdx image. A) Muscle fiber boundaries were manually segmented from cropped 150x150µm region of picrosirius red image. B) Segmented image was binarized and repeated in a 3x3 grid. Centroids were defined within each muscle fiber and used as seed points for Voronoi tessellation. C) Polygon vertices were modified to define both ECM and muscle regions and maintain periodicity. D) Surface mesh was defined with Delaunay triangulation using muscle vertices, refining mesh within muscle triangles, and then refining mesh within all triangles.*

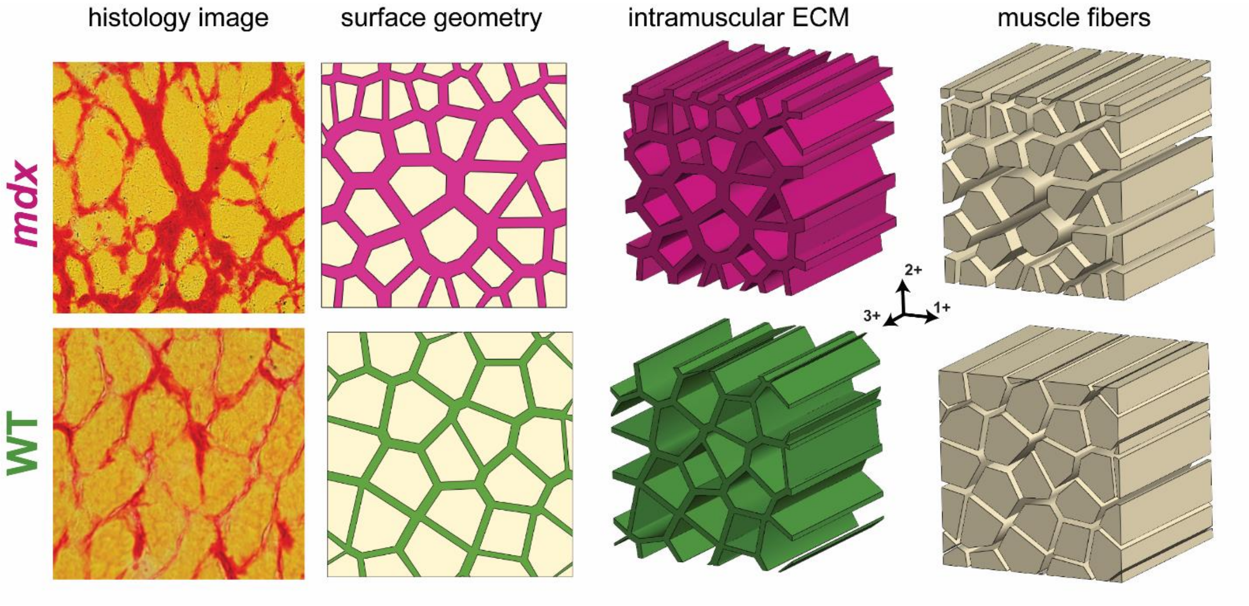

Figure 4.4: Mdx (top) and WT (bottom) intramuscular model geometries generated from picrosirius red stained cross-sections.

Material properties: A transversely isotropic, nearly incompressible, hyperplastic constitutive relationship representing the passive and active behavior of skeletal muscle was assigned to the muscle elements in the intramuscular model.[67] Maximum isometric stress was assigned from single muscle fiber experiments in *mdx* and WT EDL muscle and held constant for all simulations, as no significant differences were seen between *mdx* and WT mice.[132] The bulk modulus was varied to ensure volume preservation and all other material parameters were based on previous modeling studies.[69,70] We set the activation term to 0, as we were only examining passive conditions. All muscle parameters were constant across all simulations (**Table 4.1**).

Table 4.1: Material parameters that were held constant or calibrated (*)

Muscle: Uncoupled solid mixture	
Density	1
k	1,000 kPa
Muscle material	
Along fiber shear modulus (G_1)	3.87 kPa
Cross fiber shear modulus (G_2)	22.4 kPa

Exponential stress coefficients (p_1)	0.04
Fiber uncrimping factor (p_2)	6.6
Optimal fiber length (λ_{ofl})	1
Maximum isometric stress (σ_{max})	100 kPa
Fiber stretch for straightened fibers (λ^*)	1.06
Activation level (α)	0
Fiber vector	(0,0,1)
ECM: Uncoupled solid mixture	
Density	1
k	10,000 kPa
Ellipsoidal fiber distribution	
Fiber exponent (β)	2
*Fiber stiffness (ξ_{total})	WT: 200 kPa *Mdx*: 300 kPa
Material axes	a (0,0,1)
Mooney-Rivlin	
Coefficient of first invariant term (c1)	$1000\xi_{total}$
Coefficient of second invariant term (c2)	0

A coupled solid mixture was used to represent tensile load bearing collagen fibers and the non-tensile load bearing “ground matrix”. An isotropic Mooney-Rivlin material was used for the ground matrix, governed by the c_1 and c_2 material coefficients. An ellipsoidal fiber distribution was used to represent collagen, where the strain energy density is defined by power law exponents (β_{e1}, β_{e2}, β_{e3}) and stiffness parameters (ξ_{e1}, ξ_{e2}, ξ_{e3}).[133] These material parameters vary based on the material axes (e_1, e_2, e_3) and thus the ratio of their components determines their relative contribution along each material axes. Specific details and constitutive equations can be found in the FEBio user manual (help.febio.org). For all simulations $\beta_1=\beta_2=\beta_3$ to account for constant power law behavior across material axes. The ratio of the total collagen fiber stiffness ($\xi_{tot}= \xi_{e1}+\xi_{e2}+\xi_{e3}$) to the ground matrix stiffness (c_1) was held constant, assuming a constant density of collagen within the ECM. We selected $\xi_{tot}=1000c_1$ so that the material response was driven by the fibers (**Supp Fig 4.1**). The total collagen fiber stiffness was constant between intramuscular and epimuscular ECM elements and is referred to as k^{coll}. The collagen fiber distribution (ξ_{e1}/ξ_{e2}) was assigned separately for each ECM layer and is referred to as $cfdist^{intra}$ and $cfdist^{epi}$, with $\xi_{e3}=\xi_{e2}$ for all simulations.

For the epimuscular ECM material, e_1 corresponded to the transverse cross-muscle fiber direction and e_2 corresponded to the longitudinal along-muscle fiber direction, as collagen is reported to be oriented transverse to muscle fibers in the epimysium.[127] The epimuscular collagen fiber distribution ($cfdist^{epi}$) was determined from scanning electron microscopy (SEM) images of collagen fibers within the diaphragm muscle epimysium in 6-month-old *mdx* and WT mice from our previous study.[127] In that study, local collagen fiber directions were measured from the SEM images and here we fit the ratio of ξ_{e1}/ξ_{e2} based on the height and width of the probability density function of local fiber directions.

For the intramuscular ECM material, e_1 corresponded to the longitudinal along-muscle fiber direction and e_2 corresponded to the transverse cross-muscle fiber direction, as intramuscular collagen fibers are reported to primarily align with muscle fiber direction in diaphragm muscle.[60] The intramuscular collagen fiber distribution ($cfdist^{intra}$) was varied during material parameter calibration as described below.

Boundary conditions: To replicate each condition from our biaxial experiments, we simulated biaxial and uniaxial loading in our micromechanical models. We assumed that the composite materials for the intramuscular and epimuscular layers are spatially periodic and thus our micromechanical models can be treated as repeating unit cells (RUC) within each layer. Therefore, we assume that the average deformation of the cell is equal to the macroscopic deformation gradient and boundaries on opposite surfaces of the RUC are compatible.[15] This assumption allowed us to determine boundary conditions for each loading scenario (**Table 4.2**). To implement the boundary conditions in the models, we assigned linear constraints with specified load curves to govern the displacement between nodes in the respective degree in freedom.

Table 4.2: Periodic boundary conditions applied to intramuscular models

Loading scenario	Macroscopic deformation gradient	Periodic boundary conditions	Application
***biax**: along-muscle fiber (3+) and cross-muscle fiber (1+) lengthening*	$F_{1+,3+}^{macro}=\begin{bmatrix}\lambda & 0 & 0\\ 0 & \frac{1}{\lambda^2} & 0\\ 0 & 0 & \lambda\end{bmatrix}$ $\lambda=1.1$	$u_1^{face1+}=(\lambda-1)\ell_1+u_1^{face1-}$ $u_3^{face1+}=u_3^{face1-}$ $u_3^{face3+}=(\lambda-1)\ell_3+u_3^{face3-}$ $u_1^{face3+}=u_1^{face3-}$	Model calibration step 1
***in vivo**: along-muscle fiber (3-) shortening and cross-muscle fiber (1+) lengthening*	$F_{1+,3-}^{macro}=\begin{bmatrix}-\lambda_1 & 0 & 0\\ 0 & \frac{1}{-\lambda_1\lambda_3} & 0\\ 0 & 0 & \lambda_3\end{bmatrix}$ $\lambda_1=-1.1,\lambda_3=1.1$	$u_1^{face1+}=(-\lambda_1-1)\ell_1+u_1^{face1-}$ $u_3^{face3+}=(\lambda_3-1)\ell_3+u_3^{face3-}$	Model calibration step 2
***uniax cross**: Uniaxial cross-muscle fiber (1+) lengthening*	$F_{1+}^{macro}=\begin{bmatrix}\lambda & 0 & 0\\ 0 & \frac{1}{\sqrt{\lambda}} & 0\\ 0 & 0 & \frac{1}{\sqrt{\lambda}}\end{bmatrix}$ $\lambda=1.1$	$u_1^{face1+}=(\lambda-1)\ell_1+u_1^{face1-}$ $u_3^{face1+}=u_3^{face1-}$ $u_3^{face3+}=u_3^{face3-}$ $u_1^{face3+}=u_1^{face3-}$	Model calibration step 3
***uniax along**: Uniaxial along-muscle fiber (3+) lengthening*	$F_{3+}^{macro}=\begin{bmatrix}\frac{1}{\sqrt{\lambda}} & 0 & 0\\ 0 & \frac{1}{\sqrt{\lambda}} & 0\\ 0 & 0 & \lambda\end{bmatrix}$ $\lambda=1.1$	$u_3^{face3+}=(\lambda-1)\ell_3+u_3^{face3-}$ $u_1^{face3+}=u_1^{face3-}$ $u_3^{face1+}=u_3^{face1-}$ $u_1^{face1+}=u_1^{face1-}$	Model validation

Bulk tissue properties: Average along-muscle fiber and cross-muscle fiber element stresses and strains outputted from the intramuscular ($\sigma_{11}^{intra}, \sigma_{33}^{intra}$) and epimuscular ($\sigma_{11}^{epi}, \sigma_{33}^{epi}$) models were used to calculate the total predicted stress (σ_{total}) based on the areas of the intramuscular (a_{intra}) and epimuscular (a_{epi}) regions using the Voigt model:

$$\sigma_{total} = \frac{a_{epi}\sigma_{epi} + a_{intra}\sigma_{intra}}{a_{epi} + a_{intra}}$$

Equation 4.3

Bulk tissue stiffness was determined by plotting the total stress-strain curve and determining a linear fit at 3.5% strain.

Calibration and validation with in vitro biaxial data

Calibration: To calibrate the unknown parameters in our ECM material (k^{coll}, $cfdist^{intra}$) we varied the collagen fiber stiffness (10kPa< k^{coll} <800kPa) and intramuscular collagen fiber distribution (0.1< $cfdist^{intra}$ <2) independently in both the *mdx* and WT models. We selected a range of collagen distribution values to encompass the variability seen in the literature, where collagen fibers are reported to primarily align in the along-muscle fiber direction ($cfdist^{intra}$ <1)[126] or cross-muscle fiber direction ($cfdist^{intra}$ <1).[127] The range of collagen fiber stiffness values was selected to encompass the range of ECM stiffness values reported for decellularized diaphragm muscle from *mdx* and WT mice.[60] This method allowed us to determine the relationship between each parameter and tissue properties and then narrow down parameter sets sequentially. We simulated a series of deformations in the epimuscular and intramuscular models (**Table 4.2**) and compared the bulk tissue properties from the models with the experimental data. After each series of simulations, we excluded parameter sets that fell outside of one standard deviation from the measured group averages (**Supp Table 4.1**). Calibration was performed in the following order: (1) The biax test was simulated first and total model predicted stiffnesses ($k_{11}^{tot}, k_{33}^{tot}$) as well as stiffness ratio ($k_{33}^{tot}/k_{11}^{tot}$) at 3.5% strain were compared with experimental measurements. (2) Next, the *in vivo* test was simulated, and the total model predicted stresses ($\sigma_{11}^{tot}, \sigma_{33}^{tot}$) at 1% strain were compared with experimental measurements. For this step, we compared stresses because we applied a negative along-muscle fiber strain, and thus a stiffness calculation was not meaningful. (3) Finally, the uniax cross test was simulated, and total model predicted cross-muscle fiber stiffnesses (k_{11}^{tot}) at 3.5% strain were compared with experimental measurements.

Validation: After reducing the parameter values such that the models fit within the experimental range from all calibration experiments, we used the uniax along test to validate the model predictions. The total model predicted along-muscle fiber stiffnesses (k_{33}^{tot}) at 3.5% strain were compared with experimental measurements.

In silico **investigations informed by variation in experimental data**

To isolate the influence of specific structural parameters within epimuscular and intramuscular ECM on bulk muscle tissue properties, we performed a series of sensitivity analyses. The average of the calibrated *mdx* models was selected as our baseline model and we varied each structural parameter through the range of values measured from the picrosirius red stained images. Intramuscular area fraction was varied by assigning a range of ECM thickness values during the model geometry generation such that ($0.17 < ECM_{af}^{intra} < 0.53$). The ratio of intramuscular to epimuscular area was varied in the bulk stress calculation ($10 < \frac{a^{intra}}{a^{epi}} < 35$). Collagen fiber distribution was also independently varied in the intramuscular ECM based on the range of values narrowed down during our calibration process ($0.1 < cfdist^{intra} < 1$).

4.4 Results

Model calibration suggests that intramuscular collagen fibers are more distributed in the cross-muscle fiber than along-muscle fiber direction. For all calibrated models, $cfdist^{intra}$ <1 was required, indicating that intramuscular collagen fibers are more aligned in e_2 (cross-muscle fiber direction: 1+) than e_1 (muscle fiber direction: 3+) (**Supp Table 4.1**). The biax calibration narrowed down the collagen distribution values (*mdx:* 200kPa<k^{coll}<800kPa, 0.1<$cfdist^{intra}$ <0.8, WT: 100kPa<k^{coll}<600kPa, 0.1< $cfdist^{intra}$ <0.7, **Fig 5**) and the *in vivo* calibration narrowed down the collagen stiffness values (*mdx*: 200kPa<k^{coll} <300kPa, 0.1< $cfdist^{intra}$ <0.2, WT: k^{coll} =200kPa, 0.2< $cfdist^{intra}$ <0.7, **Fig 4.6A-D**). The uniax cross calibration further narrowed down the parameters, with a larger range in the WT models (*mdx*: k^{coll}=200kPa, 0.125< $cfdist^{intra}$ <0.175, WT: k^{coll}=200kPa, 0.2< $cfdist^{intra}$ <0.7, **Fig 4.6E-F**). The cross- (ξ_{e2}) relative to the along-muscle fiber direction (ξ_{e1}) collagen fiber stiffness was 5.7-8 times greater in the calibrated *mdx* models and 1.4-5 times greater in the calibrated WT models. This finding suggests that there is greater intramuscular collagen alignment in the cross-muscle fiber direction in the *mdx* relative to WT case.

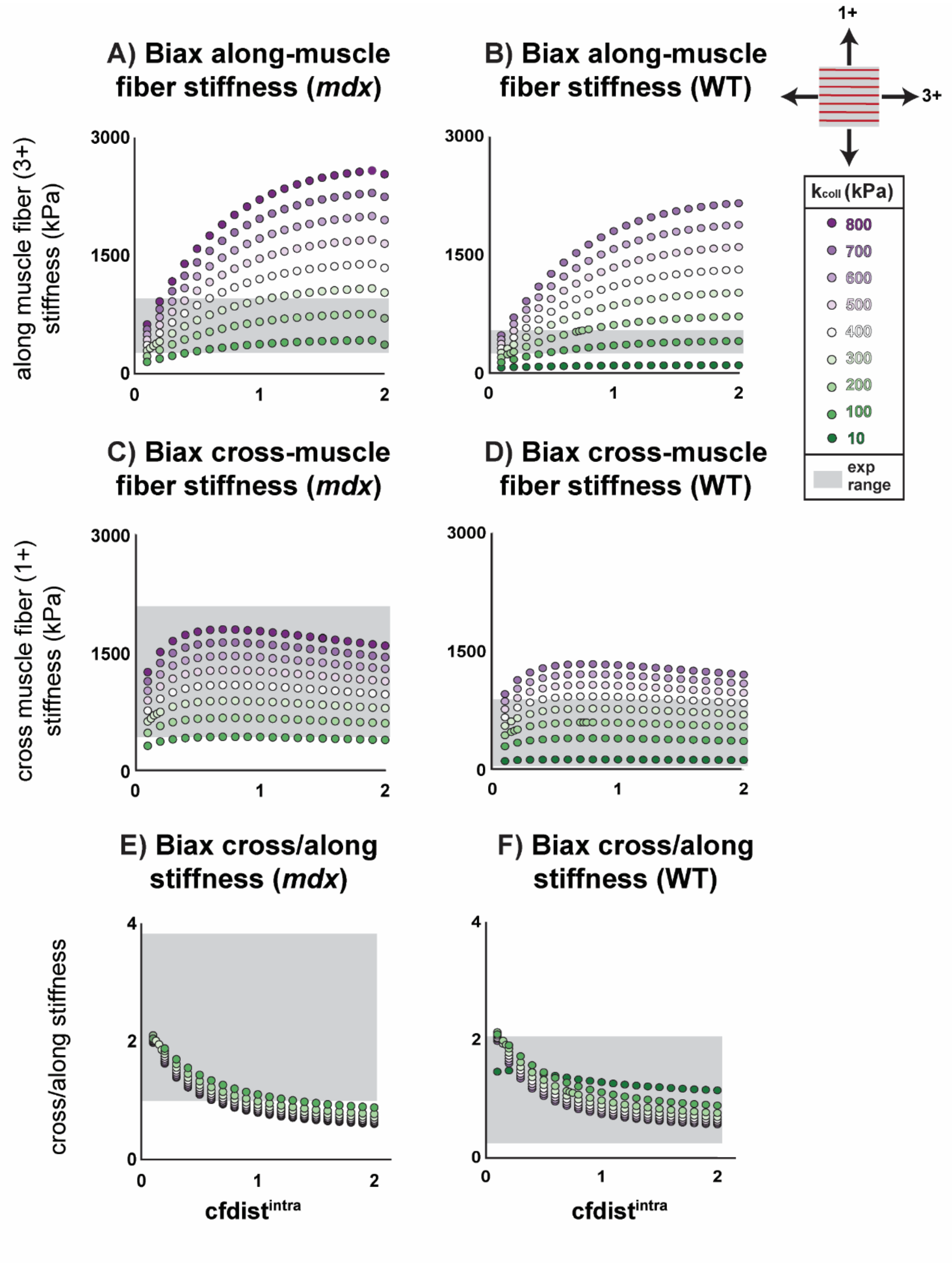

Figure 4.5: Initial mdx and WT model calibration varying total collagen fiber stiffness ($10kPa<\xi tot<800kPa$) and intramuscular collagen fiber distribution ($0.1< \xi e1/\xi e2 <2$). Range in experiments shown in shaded bar with individual model predictions in circles. The equibiaxial lengthening test was simulated and the total model predicted stiffnesses (k_{33}^{tot}, k_{11}^{tot}) as well as stiffness ratio ($k_{33}^{tot}/k_{11}^{tot}$) at 3% strain were compared with experimental measurements.

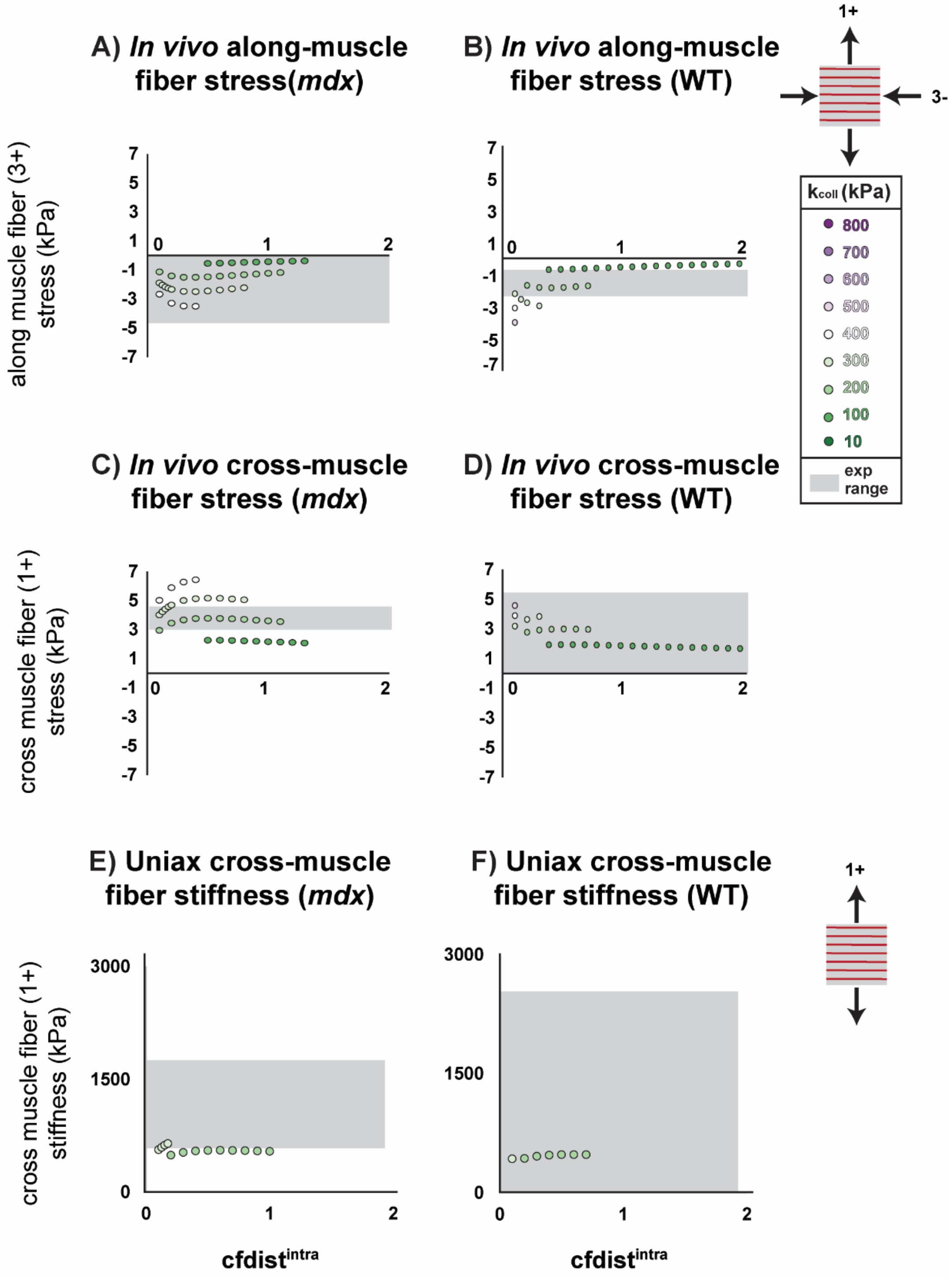

Figure 4.6: Additional mdx and WT model calibrations based on narrowed down parameter sets from Fig 4. Range in experiments shown in shaded bar with individual model predictions in circles. A) The along-muscle fiber shortening, cross-muscle fiber lengthening test (in vivo) was simulated, and the total model predicted stresses (σ_{11}^{tot}, σ_{33}^{tot}) at 1% strain were compared with experimental measurements. B) The uniaxial cross-muscle fiber lengthening test was simulated, and the total model predicted cross-muscle fiber stiffnesses (k_{11}^{tot}) at 3% strain were compared with experimental measurements.

Validated models suggest an increase in cross-muscle fiber tissue stiffness in *mdx* relative to WT models. Bulk along-muscle fiber tissue stiffnesses from calibrated *mdx* and WT models fell within the uniaxial along experimental range, validating the model predictions (**Fig 4.7E**). Comparison across the calibrated models suggests greater cross-muscle fiber stiffness in the *mdx* models compared to WT during the biax (*mdx*: $k_{11}^{tot} = 690 \pm 30$ kPa, WT: $k_{11}^{tot} = 568 \pm 34$ kPa, **Fig 4.7B**) and uniax cross (*mdx*: $k_{11}^{tot} = 622 \pm 25$ kPa, WT: $k_{11}^{tot} = 470 \pm 19$ kPa, **Fig 4.7F**) conditions. Additionally, greater along-muscle fiber and cross-muscle fiber stresses were seen in the *mdx* models compared with the WT models during the *in vivo* condition (*mdx*: $\sigma_{11}^{tot} = 4.41 \pm 0.17$ kPa, $\sigma_{33}^{tot} = -2.15 \pm 0.11$ kPa, WT: $\sigma_{11}^{tot} = 2.94 \pm 0.09$ kPa, $\sigma_{33}^{tot} = -1.77 \pm 0.06$ kPa) (**Fig 4.7C-D**).

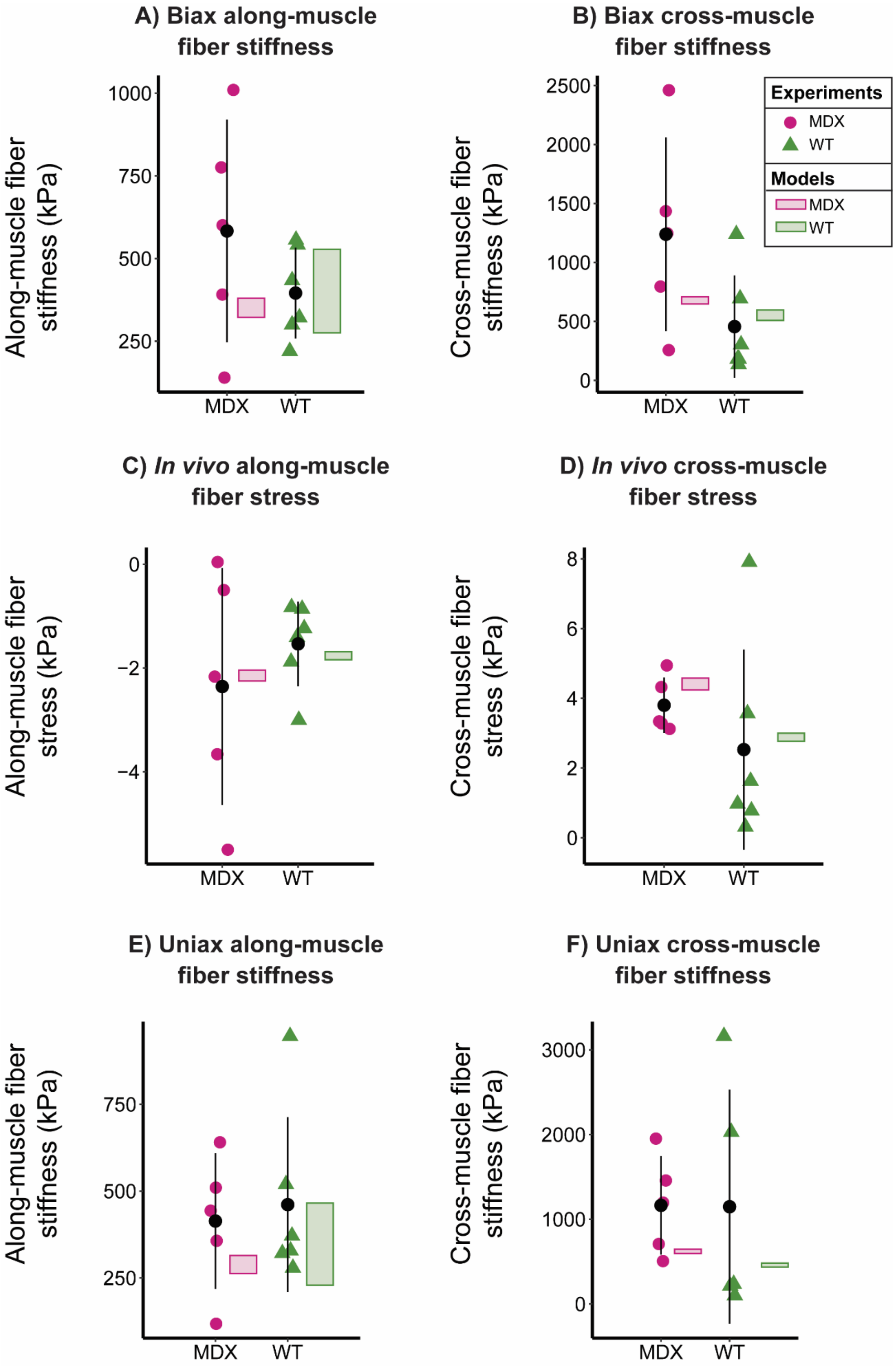

*Figure 4.7**:** Finalized model predictions (shaded bars) shown with* mdx *(circle) and WT (triangle) experimental data points. Along-muscle fiber (A) and cross-muscle fiber (B) stiffness at 3% applied equibiaxial strain. Along-muscle fiber (C) and cross-muscle fiber (D) stress at 1% applied cross-muscle fiber and -1% along-muscle fiber strains. Along-muscle fiber stiffness (E) at 3% applied uniaxial along-muscle fiber strain. Cross-muscle fiber stiffness (F) at 3% applied uniaxial cross-muscle fiber strain.*

Differences in tissue stresses were observed during cross-muscle fiber loading. Analysis of the models revealed that the differences in properties between the *mdx* and WT models led to differing stress distributions within the intramuscular and epimuscular regions. During biaxial lengthening, greater cross- relative to along-muscle fiber stress ($\frac{\sigma_{11}}{\sigma_{33}}$>1) was seen in the *mdx* model within the intramuscular ECM ($\frac{\sigma_{11}^{intra}}{\sigma_{33}^{intra}} = 2.33$) and epimuscular ECM ($\frac{\sigma_{11}^{epi}}{\sigma_{33}^{epi}} = 1.33$) (**Fig 4.8A**). In the WT model, greater cross- relative to along-muscle fiber stress was only observed in the epimuscular ECM ($\frac{\sigma_{11}^{epi}}{\sigma_{33}^{epi}} = 1.27$) during biaxial lengthening (**Fig 4.8B).** Analysis of the models across loading conditions revealed nonuniform strains within the intramuscular ECM during cross-muscle fiber lengthening. During the uniax cross and the *in vivo* simulations, 1st principal strains were primarily oriented in the cross-muscle fiber direction, with variability in magnitudes across ECM elements seen in the *mdx* model (**Fig 4.9**).

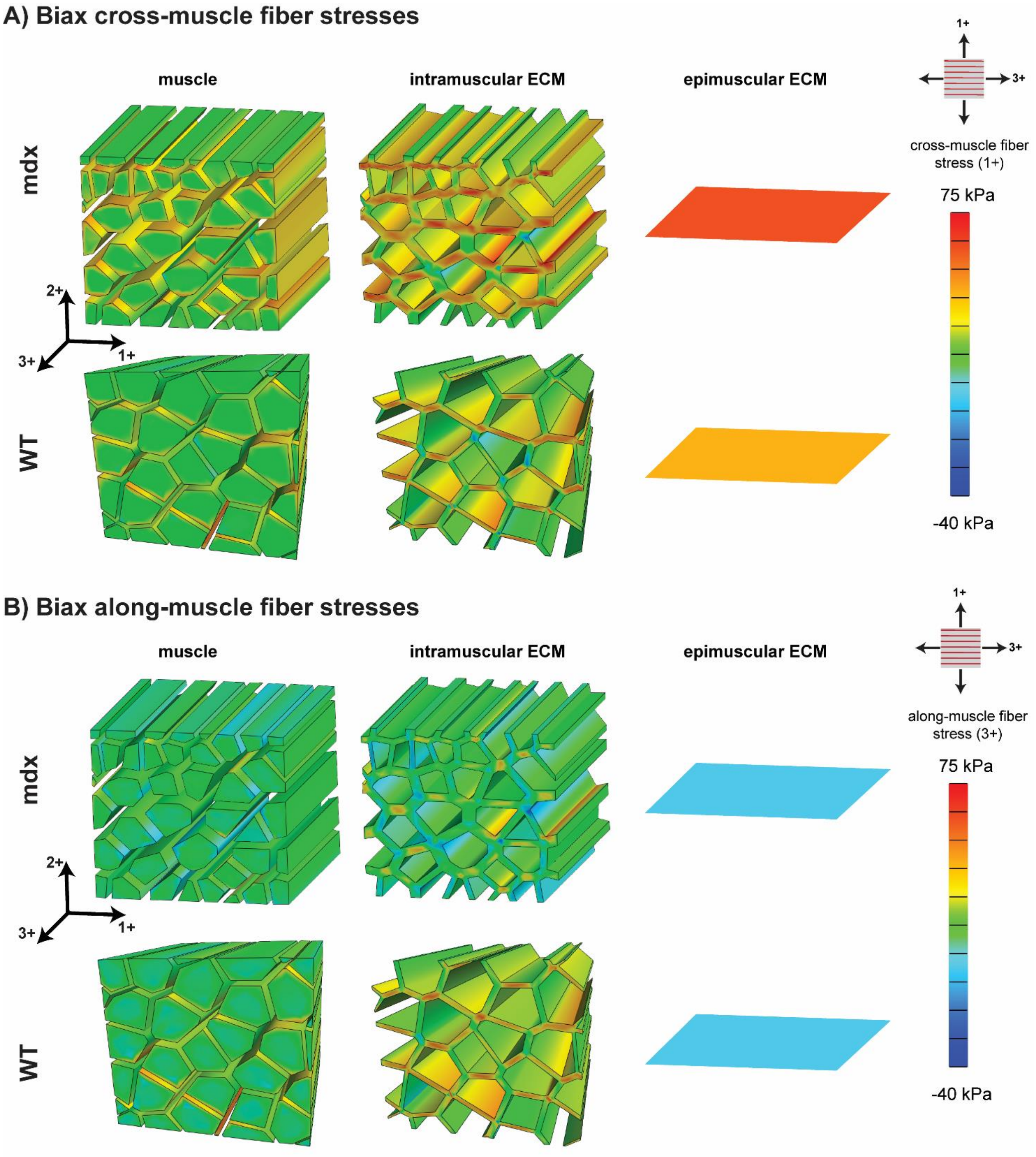

*Figure 4.8***:** *Intramuscular model outputs for example mdx (ξ_{tot}=300kPa, $\xi_{e1}/\xi_{e2}^{intra}$ = 0.015) and WT (ξ_{tot}=200kPa, $\xi_{e1}/\xi_{e2}^{intra}$ = 0.5) models from equibiaxial lengthening simulation. A) Cross-muscle fiber stress at 5% applied equibiaxial strain. B) Along-muscle fiber stress at 5% applied equibiaxial strain***.**

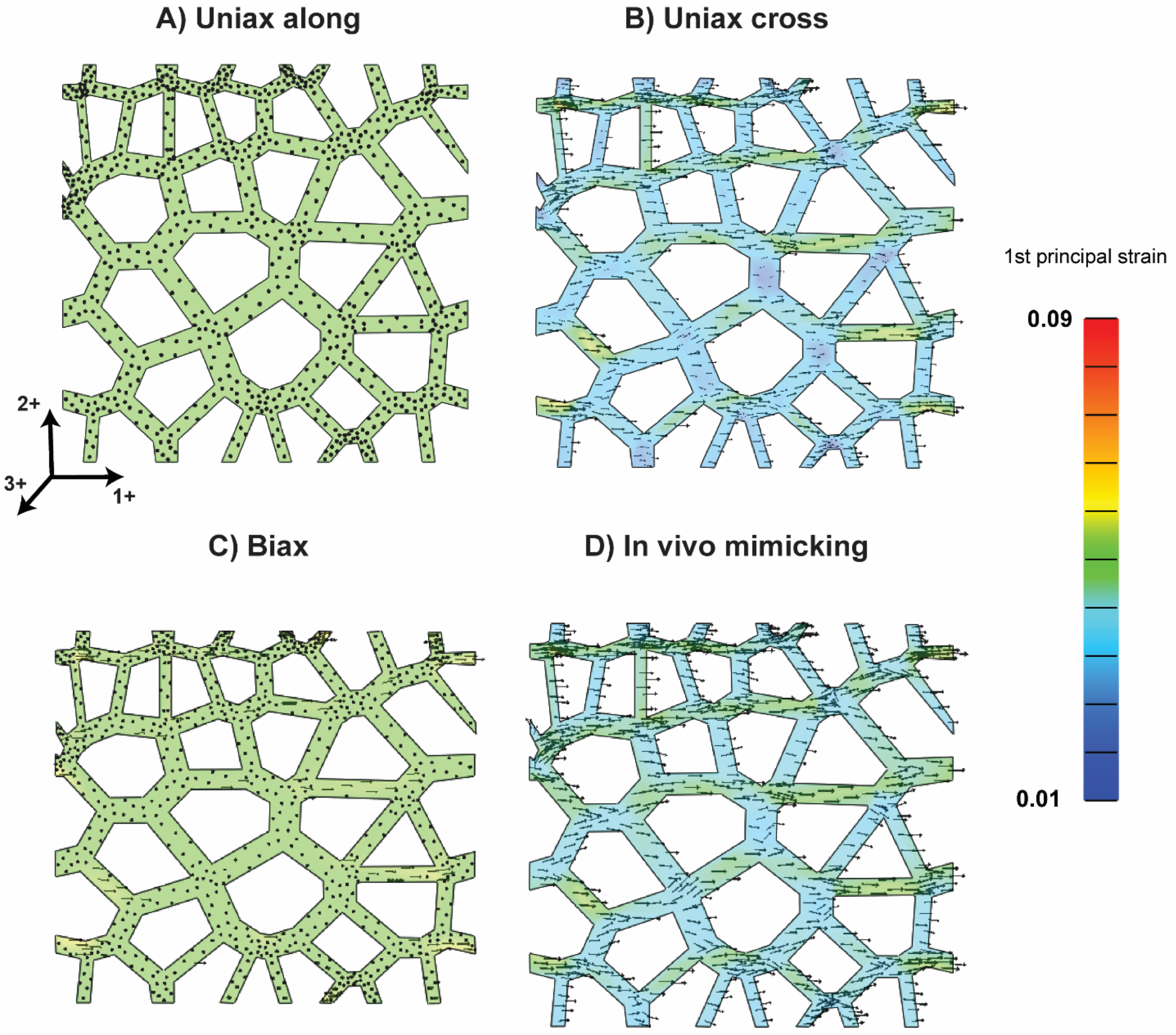

Figure 4.9: 1^{st} principal strain orientations (arrows) and magnitudes (color) in ECM elements for mdx *model (ξ_{tot}=300kPa, $\xi_{e1}/\xi_{e2}^{intra}$ = 0.015). A) 5% applied uniaxial cross-muscle fiber strain. B) 5% applied uniaxial along-muscle fiber strain. C) 5% applied equibiaxial strain. D) 5% applied cross-muscle fiber and -5% along-muscle fiber strains.*

***In silico* investigations highlight the importance of collagen distribution within the ECM.** The along- (k_{33}^{tot}) and cross-muscle fiber (k_{11}^{tot}) stiffness varied highly across the simulated range of collagen distribution ($0<cfdist^{intra}<1$) and only varied minimally with the simulated range of ECM area fractions ($0.17 < ECM_{af}^{intra} < 0.53$) and the ratio of intramuscular to epimuscular areas ($10 < \frac{a^{intra}}{a^{epi}} < 35$). Over the simulated range of collagen distributions, k_{33}^{tot} varied by 214% and k_{11}^{tot} varied by 43%. By contrast, over the simulated range of intramuscular ECM area fractions, k_{33}^{tot} varied by 32% and k_{11}^{tot} varied by 13%. Over the simulated range of the ratio of intramuscular to epimuscular area, k_{33}^{tot} varied by 31% and k_{11}^{tot} varied by 16%. These results suggest that variations in microstructure have a larger influence on along- than cross-muscle fiber stiffness, and that collagen distribution has a larger effect on tissue stiffness compared with the other variations in microstructure (**Fig 4.10)**.

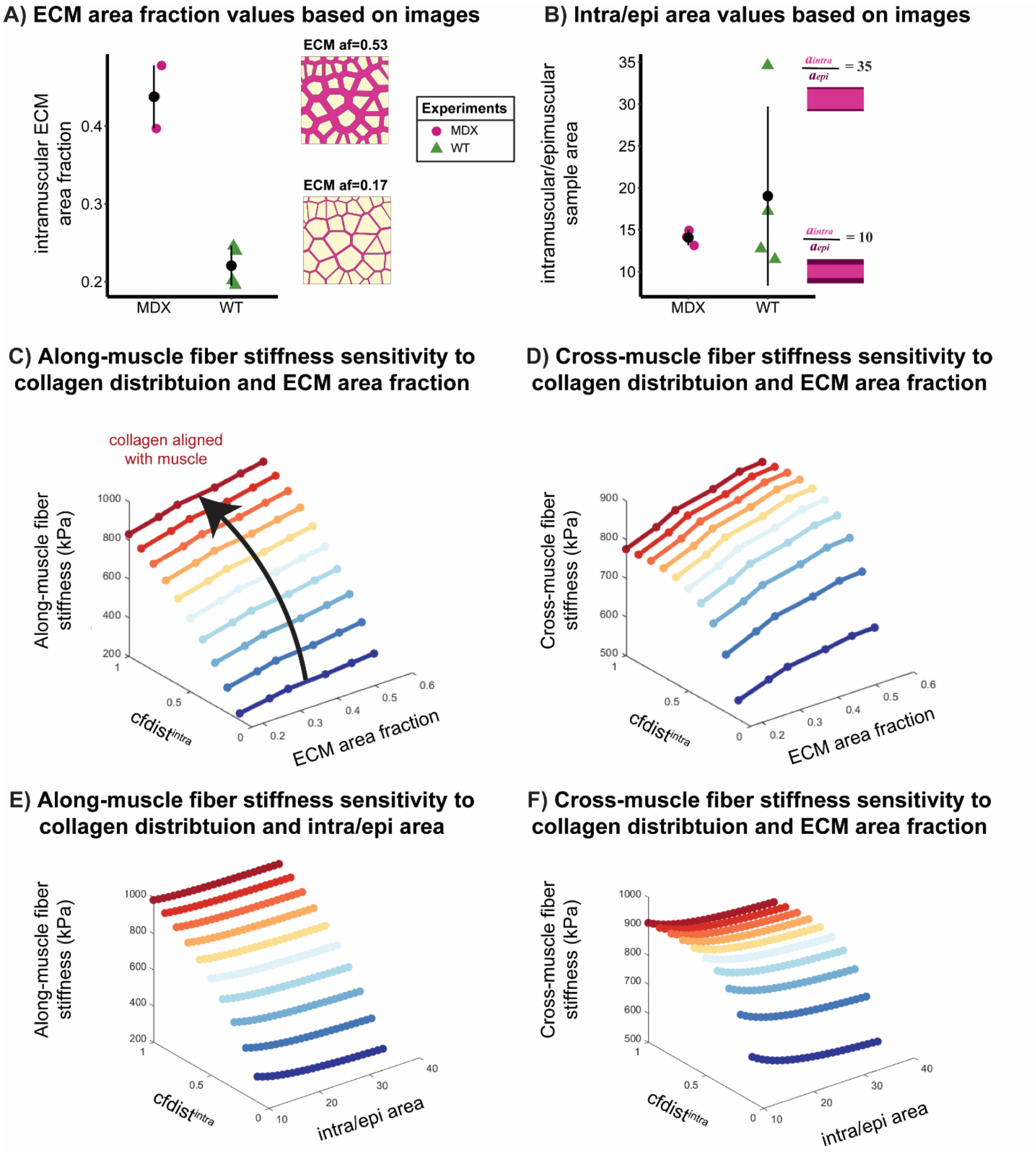

Figure 4.10: Mdx (pink circle) and WT (green triangles) image-based measurements of A) intramuscular area fraction and B) ratio of intramuscular and epimuscular areas used for range of values in model perturbations. Sensitivity analysis of the effect of varying intramuscular collagen distribution and ECM area fraction on biaxial along- (C) and cross-muscle fiber stiffness (D). Sensitivity analysis of varying intramuscular collagen distribution and ratio of intramuscular to epimuscular area on biaxial along- (E) and cross-muscle fiber stiffness (F).

4.5 Discussion

Here we present a novel framework to examine how collagen microstructure contributes to macroscopic muscle tissue properties. We focused on diaphragm muscle due to the devastating consequences of diaphragm muscle fibrosis in DMD and measured tissue structure and mechanical properties in *mdx* and WT mice. Epimuscular and intramuscular micromechanical models were developed to predict local stresses and strains and determine bulk tissue properties. The process of model calibration led to the conclusion that intramuscular collagen fibers are likely aligned primarily in the cross-muscle fiber direction in both the *mdx* and WT models, with greater cross-muscle fiber alignment required in the *mdx* models compared with WT (**Figs 4.5-6**). Higher cross-muscle fiber stiffness was predicted in the *mdx* models compared with the WT models (**Fig 4.7**), and differences between ECM and muscle properties were seen during cross-muscle fiber loading (**Figs 4.8-9**). Analysis of the models revealed that variation in the distribution of collagen fibers had a much more substantial impact on tissue stiffness, as compared to variation in ECM area fraction (**Fig 4.10**), providing an explanation for the lack of correlation between ECM area fraction and tissue stiffness across experimental studies.

Previous studies found that increased collagen levels in fibrotic tissue do not correlate with increased passive muscle tissue stiffness, suggesting that other changes in muscle from fibrosis influence stiffness. While it would be challenging to isolate these factors experimentally, we could use our model to isolate the impacts of specific structural variations during along-muscle fiber loading to compare model predictions with existing literature.[14] Similar to Smith et al, we did not observe a relationship between ECM area fraction and along-muscle fiber stiffness (**Fig 4.11**). However, our model predictions reveal that while changes in ECM area fraction have a minimal impact on along-muscle fiber stiffness, the variation in collagen fiber distributions accounts for the large range of experimental measurements. This finding highlights the important role of collagen microstructure on passive muscle tissue properties and provides important context to the many experiments over the last decade that have attempted to correlate muscle tissue stiffness with collagen amount and/or ECM area fraction. Rather, we found that collagen reorganization has more of an impact on stiffness and therefore may provide an effective target for therapeutics and should be considered in designing and testing new treatments.

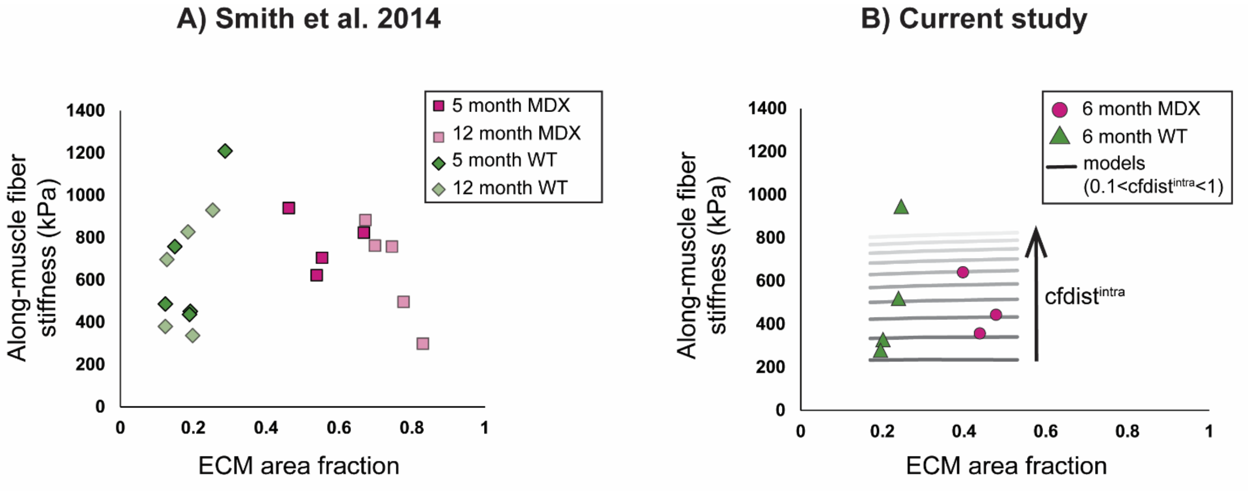

Figure 4.11: A) Measurement of ECM area fraction and along-muscle fiber stiffness from uniaxial diaphragm muscle strip testing. Recreated from Smith et al (2014).[14] B) Experiments and model results from our current study. Image based measurements of intramuscular area fraction and along-muscle fiber stiffness of mdx (circle) and WT (triangle) data points. Model predictions shown with grey lines.

A key finding of this study is that, to fit the experimental data, intramuscular collagen must be aligned in the cross-muscle fiber direction, with increased collagen alignment in the *mdx* models compared with the WT models. These findings are in contrast to a prior study that used second harmonic generation images collected in the longitudinal plane to measure collagen orientation. In those images, collagen appeared to be primarily aligned with muscle fibers with no significant differences between *mdx* and WT tissue.[126] However, it is difficult to visualize complex 3-D geometries with 2-D images, especially when collected in the longitudinal plane where any components to collagen direction out of the plane (IE: transverse to the fiber direction) would not be perceived. Furthermore, our findings do align with our previous measurements in the epimuscular ECM, which is more suited for 2-D imaging due to its sheet-like nature and thus more detailed characterization was possible with SEM imaging.[127] Additional studies show a helical arrangement of collagen fibers surrounding muscle fibers within the intramuscular ECM.[25–27] Lastly, all of the imaging studies require tissue preparation and sectioning, which likely impacts collagen microstructure. Through calibrating the distribution of intramuscular collagen fibers using our mechanical testing measurements we were able to extract the collagen alignment without the need to section or modify the structures within the sample.

It is important to acknowledge the limitations of our framework. Our experiments and models focused on tissue properties at low strains (<5%). While we selected these values based on *in vivo* strains seen in diaphragm muscle,[64] it is important to consider the role of collagen microstructure further in the linear region of the passive force length curve. Additionally, we did not directly measure collagen fiber organization within the intramuscular ECM; further 3-D imaging would increase confidence in model predictions. Our intramuscular models utilized Voronoi tessellation methods to estimate muscle fiber geometries and had a relatively coarse mesh; therefore, the models are best poised for investigating the effects of ECM microstructure and not detailed fiber geometry. To better replicate muscle fiber geometries increased mesh density is required but would decrease computational efficiency.

There was a large range in our experimental data; therefore, we did not detect significant differences in tissue properties between *mdx* and WT mice. However, our models were calibrated with multiple experiments and predicted disease dependent differences in tissue anisotropy (cross- relative to along-muscle fiber properties). This highlights the need to characterize the behavior of biological tissues, which are highly variable between animals, during multiple distinct loading states, as well as the advantage of our coupled framework to minimize errors from experimental measurements alone. Previous studies characterized anisotropic muscle tissue properties through uniaxial testing in multiple directions,[134–136] or biaxial testing with equivalent along- and cross-muscle fiber lengthening strains.[64,137] Our model predictions reflected trends measured in diaphragm muscle tissue, with higher cross- relative to along-muscle fiber stiffness under uniaxial loading [61–63] and higher cross-muscle fiber stiffness in *mdx* relative to WT models during equibiaixal lengthening.[64] Previous *in vivo* experiments in the diaphragm muscle measured cross-muscle fiber lengthening and along-muscle fiber shortening strains during tidal breathing, with lower strains in *mdx* relative to WT mice.[64] Thus, our *in vivo* condition allows us to contextualize passive tissue properties during *in vivo* loads, and the higher stresses predicted in the *mdx* relative to WT models are implicated on the lower diaphragm muscle strains seen in *mdx* relative to WT mice. [64]

Our framework allowed us to validate the coupled models with measurements of bulk tissue properties, while predicting local properties that cannot be measured experimentally. Previous studies extrapolate the ECM's contribution to passive muscle properties by comparing measurements before and after muscle decellularization,[42,60,138] and predicted that the ECM accounts for 60-70% of diaphragm muscle tissue stiffness, with no significant differences in stiffness between dystrophic and healthy ECM.[60] Our models also highlight the ECM's contribution to passive properties and provide the unique ability to predict properties in distinct ECM regions while accounting for the contribution of muscle fibers. During the biax simulation, higher cross-muscle fiber stresses were seen in the epimuscular compared with intramuscular ECM (**Fig 4.8A**), while higher along-muscle fiber stresses were seen in the intramuscular compared with epimuscular ECM (**Fig 4.8B**). From our sensitivity analyses, we also found that both along- and cross-muscle fiber stiffness decreased with an increase in the ratio of intramuscular to epimuscular sample areas (**Fig 4.10C**). This analysis highlights nonuniformity in the stiffness of ECM layers and suggests that an accumulation of collagen within the epimuscular ECM, as compared with the intramuscular ECM, has a larger influence on bulk tissue properties. Further, we predicted differences in our *mdx* and WT models that may not have been reflected in uniaxial measurements of decellularized matrices.[60] During the *in vivo* simulations, 1st principal strains were primarily oriented in the cross-muscle fiber direction (**Fig 4.9**), and *in vitro* studies show that cells orient parallel to the direction of stretch,[139,140] with fibroblasts observed to deposit collagen in the direction of local alignment. Taken together, these findings suggest that *in vivo* ECM strains cause collagen fibers to be deposited in the cross-muscle fiber direction, providing an explanation for our model predictions of cross-muscle fiber collagen alignment.

By tightly coupling experiments and finite element models, our framework addresses limitations of previous micromechanical models that were not directly validated[15,76] or relied on integrating measurements from several studies.[74,75,128] Here we collected images and conducted mechanical testing in the same subset of *mdx* and WT mice; thus, our models were developed, calibrated, and validated with experimental data specific to *mdx* and WT diaphragm muscle tissue. To our knowledge, this is the first framework to account for distinct layers of the ECM and examine the role of collagen microstructure on muscle tissue properties. Additionally, we provided novel insights into collagen's complex role on passive muscle properties. We found that the primary orientation of collagen fibers relative to muscle fibers explains anisotropic tissue properties observed in the diaphragm muscle, and that the distribution of collagen fibers explains discrepancies between measurements of collagen amounts and tissue stiffness. These methods can be applied to the multitude of disorders involving fibrosis, as well as in additional muscle groups[110,125] and soft tissues[50,141,142] where changes in collagen microstructure are observed. To do so, we also highlight (1) the need to consider collagen's 3-D microstructure and *in vivo* biaxial loads sustained by specific muscle tissues to measure relevant structure-function relationships, (2) the capability of multiscale mechanical modeling to fill gaps from experimental measurements alone, and (3) that when characterizing collagens' contribution to passive muscle tissue properties, it is far beyond the amount that counts.

Acknowledgeents

Funding for this work was provided by NIH grant #U01AR06393 and #5T32GM136615 (UVA Biotechnology Training Program). We would also like to thank Steve Maas for support with FeBio and the Advanced Microscopy Facility at the University of Virginia for support for the imaging conducted in this study.

Make a plan. Set a goal. Work toward it,
but every now and then look around.

Drink it in, 'cause this is it.

—Meredith Grey

Chapter 5 : Conclusion

5.1 Summary

I began my PhD with what seemed like a straightforward question- *is there something about the organization of collagen fibers that can help explain surprising model predictions and experimental findings that collagen amount and tissue stiffness do not correlate in dystrophic muscle?*[14,16,17] While this question has remained the overarching direction of my research, it has untangled into several others along the way.

To begin exploring collagen organization we first had to establish methods to visualize collagen structure in healthy and diseased skeletal muscle. I was inspired by the diaphragm muscle, which is severely weakened in Duchene muscular dystrophy[37–39] and contributes to respiratory insufficiency, a leading cause of death.[7] Skeletal muscle is often imaged in the plane perpendicular to muscle fibers, characterizing fibrosis by an accumulation of intramuscular ECM surrounding muscle fibers and fascicles.[25–27] The diaphragm has a unique muscle architecture that is thin and sheet like, which led me to become interested in the outermost layer of ECM - *the epimysium*. I adapted methods to image collagen architecture from decellularized muscle tissue samples using scanning electron microscopy, imaging in the surface plane of the diaphragm muscle. This allowed us to visualize collagen fibers in the epimysium and provided a new angle from which to view the ECM.

Surprisingly, I began to notice that collagen fibers had a preferred orientation that was transverse to muscle fibers. The ECM is often assumed to be isotropic or have collagen fibers aligned with muscle fibers,[15,16] so this initial finding challenged some of our own assumptions about skeletal muscle. From imaging both *mdx* and WT tissue, I observed differences in collagen arrangement across samples, highlighting the need for rigorous methods to characterize collagen fiber organization in skeletal muscle. I then developed an image processing framework to measure the local variability in collagen fiber directions and found increased collagen fiber alignment, as well as straightness in the *mdx* tissue compared with WT. This confirmed that indeed, there were differences in collagen organization in dystrophic muscle tissue that must be considered.

However, as muscle modelers, this raised more questions for us than it answered. Specifically, I became curious about how the orientation and alignment of collagen fibers contributed to ECM stiffness in both the muscle fiber direction, as well as the transverse direction. To explore these questions, I developed an image-based finite-element modeling pipeline to automatically assign local fiber directions in the model based on the collagen fiber directions measured from the SEM images. I then simulated biaxial stretch to predict tissue stiffnesses in the longitudinal/along-muscle fiber direction and transverse/cross-muscle fiber direction. An increase in transverse relative to longitudinal stiffness was predicted in all of the models, with increased transverse stiffness in the *mdx* models compared with the WT models. As diaphragm muscle tissue is well documented to be anisotropic, with increased stiffness in the transverse relative to longitudinal direction,[61,62,106] this highlighted a role of collagen organization in regulating tissue anisotropy. It also suggested that previous measurements of diaphragm muscle stiffness from uniaxial along-muscle fiber lengthening experiments did not capture the effects of collagen reorganization.[14]

While I became fascinated by the complexity of the skeletal muscle ECM, my motivation remained in understanding how the development of fibrosis contributes to muscle dysfunction in DMD. This led to another key question of my PhD- *how do changes in collagen microstructure at the ECM-level influence mechanical properties at the muscle tissue-level?*

Previous micromechanical models from our lab had been developed to study the role of muscle-fascicle microstructure on tissue-level properties,[15,16] but were two-dimensional and focused on shear deformations. Models of *mdx* lower limb muscle highlighted the importance of ECM stiffness on macroscopic tissue properties,[17] but assumed that the ECM was transversely isotropic and aligned with muscle fibers. Before extending this framework to examine the role of collagen microstructure on biaxial tissue properties, we had to develop methods to create three-dimensional models that accounted for collagen distribution within the ECM. In seeking to balance computational efficiency with creating physically relevant model geometries, I had to rethink our previous model generation pipelines.

I focused on the intramuscular region of the diaphragm muscle and developed a framework to automatically create finite element models from segmented histology images. This framework leveraged Voronoi tessellation[71,74,75] to generate periodic geometries and Delaunay triangulation to create a surface mesh. The surface mesh was then extruded along the muscle fiber direction, generating pentahedral elements representing muscle and ECM regions. I then assigned a mixture material to the ECM elements to account for the distribution of collagen fibers within the ground matrix. While these models provided a framework to represent complex collagen microstructures and loading scenarios, their purpose was to contextualize the role of collagen on bulk muscle tissue properties.

This required a way to couple predictions from the epimuscular and intramuscular models and characterize bulk muscle tissue properties across loading scenarios. Previous experiments from the lab had revealed greater tissue stiffness in *mdx* relative to WT diaphragm muscle during equibiaxial along- and cross-muscle fiber lengthening.[64] *In vivo* sonomicrometry experiments also found lower strains in *mdx* relative to WT mice, but demonstrated that the diaphragm muscle lengthens in the cross-muscle fiber direction while it shortens in the along-muscle fiber direction.[64] This raised new questions about differences in tissue properties during *in vivo* conditions and inspired us to design a new series of biaxial experiments.

We first simulated *in vivo* strains by varying the ratio of along-muscle fiber shortening and cross-muscle fiber lengthening based on the range of measurements in *mdx* and WT samples (0.5,1,1.5), and then performed equibiaxial lengthening and uniaxial along- and cross-muscle fiber lengthening tests. Additionally, we collected images of picrosirius red stained cross-sections from the muscle samples to characterize the tissue microstructure. Similar to previous studies, we found an increase in ECM area fraction in the *mdx* images compared with the WT, but significant differences in tissue properties were not observed.

While this caused us to circle back to our original question, I now had a framework to couple the mechanical models and experiments to explain why collagen amount and tissue stiffness are not well correlated. From the histology images, I measured the relative amounts of the epimuscular and intramuscular diaphragm muscle regions, allowing us to calculate bulk tissue properties assuming these layers act in parallel during axial loading.[131] I then utilized the biaxial experiment data to calibrate and validate the bulk model predictions. To fit the experimental data, collagen fibers within the intramuscular ECM had to align in the cross-muscle fiber direction with increased alignment predicted in the *mdx* model compared with the WT model. This opposed recent findings in the literature where collagen was observed to primarily align with muscle fibers in the intramuscular ECM of diaphragm muscle.[60] However, this aligned with our findings in the epimuscular ECM where more detailed characterization was possible with scanning electron microscopy.

With this framework I was also able to isolate the effects of ECM area fraction and collagen fiber organization on tissue stiffness. We found that the distribution of collagen fibers had a greater influence on passive tissue properties than the amount of ECM and explained the variation across samples. Further, we found that tissue properties were more nonuniform during cross-muscle fiber loading and that collagen organization explained the increased cross- relative to along-muscle fiber stiffness observed in diaphragm muscle.

Overall, my findings suggest that the distribution of collagen fibers has a greater influence on passive tissue properties than collagen amount, and that collagen reorganization rather than accumulation may provide an effective target for therapeutics. By coupling experiments and mechanical models we also highlighted gaps left from predicting structure function relationships with experiments alone. I found that collagen orientation relative to muscle fiber orientation regulates the direction that tissue has greater passive stiffness in, highlighting the importance of characterizing biaxial tissue properties and considering *in vivo* loads sustained by specific muscle tissues to measure relevant tissue properties. Additionally, we must consider collagen's three-dimensional microstructure in muscle tissue and account for both epimuscular and intramuscular ECM. Finally, we measured changes in collagen organization during disease progression and provided a framework to examine how microstructural variations influence macroscopic tissue properties that can be applied to hypothesize new experiments and intervention targets.

5.2 Contributions

1. Detailed characterization of skeletal muscle epimysium and changes in collagen fiber organization during DMD.

We developed methods to image the epimuscular ECM of muscle tissue and characterize collagen fiber organization. We found that collagen fibers had a preferred orientation that was surprisingly transverse to muscle fibers in the diaphragm muscle. To our knowledge, this had not been previously reported and has implications for additional muscle groups. We also found significant age and disease effects on collagen organization, with increased collagen alignment and straightness in *mdx* samples compared with WT at 3 and 6 months. Collagen reorganization had not been previously characterized in diaphragm muscle tissue and is implicated in several other conditions involving weakening of the diaphragm muscle.

2. Development of a framework to predict mechanical implications of changes in collagen organization with disease.

We developed an image-based modeling pipeline to automatically generate finite element models from scanning electron microscopy images. These models allowed us to account for variations in local collagen fiber directions and predict mechanical properties at the extracellular matrix level. We predicted an increase in transverse relative to along muscle fiber direction stiffness in all models, with increased transverse stiffness in the 3- and 6-month *mdx* models compared with the WT models. This suggested that local changes in collagen alignment during disease increase tissue stiffness, which is implicated on cellular dynamics during fibrosis.

3. Creation of a multiscale modeling framework to predict how collagen microstructure influences bulk muscle tissue properties.

We developed a framework to couple micromechanical models of the epimuscular and intramuscular regions of the diaphragm muscle and predict bulk muscle tissue properties. To our knowledge, this is the first framework to account for distinct layers of the extracellular matrix and examine the role of collagen microstructure on muscle tissue properties. We also designed biaxial mechanical testing experiments to characterize along- and cross-muscle fiber direction tissue properties across different loading scenarios. We measured passive tissue properties while simulating *in vivo* along-muscle fiber shortening and cross-muscle fiber lengthening strain, which had not been previously characterized. We calibrated and validated the models directly using the biaxial experiments, overcoming limitations of previous models that rely on integrating measurements from several studies across different skeletal muscle groups.

4. Insights into collagen's complex role on passive muscle properties.

We found that the primary orientation of collagen fibers relative to muscle fibers explained anisotropic tissue properties of the diaphragm muscle. This highlights the importance of considering *in vivo* loads sustained by specific muscle tissues to measure relevant tissue properties. We also found that collagen organization had significant effects on bulk tissue properties, highlighting the need consider collagen's three-dimensional microstructure in muscle tissue. Our findings also challenge assumptions of transverse isotropy in skeletal muscle tissue suggesting that instead the organization of collagen fibers regulates the amount of anisotropy.

5. Characterization of effects of changes in collagen organization during fibrosis.

While previous studies have shown that increased collagen levels in fibrotic tissue do not correlate with an increase in passive muscle tissue stiffness, an explanation as to why has remained unresolved. We found that the organization of collagen fibers had a greater influence on tissue stiffness than collagen amount, with increased collagen alignment during disease implicated in increased tissue stiffness. This suggests that collagen reorganization rather than accumulation may provide an effective target for therapeutics.

5.3 Additional Applications

1. Collagen's role on passive tissue properties

The straightening and aligning of collagen fibers regulates the toe-region of the passive muscle force length curve, implicating our SEM image-based measurements on the length of the toe region of diaphragm muscle tissue. In a subset of mice from which we collected SEM images of the epimysium, equibiaxial mechanical testing was also performed before and after enzymatically digesting collagen.[64] To examine relationships between collagen organization and measured tissue stiffnesses, we performed regression analyses. In the *mdx* mice (n=4 6-month-old, n=4 12-month-old) we found significant relationships between collagen fiber straightness and along-muscle fiber stiffness, as well as the ratio of cross- to along-muscle fiber straightness (**Fig. 5.1**). These relationships aligned with our epimuscular model predictions[127] and highlight the important role of the epimysium, despite its relatively low proportion to the intramuscular ECM. This also suggests that increased collagen straightness would decrease the length of the toe region and thus passive force production would begin at shorter muscle lengths. To explore the relationship between collagen fiber straightness and toe region length, future experiments can be performed where collagen fiber straightness is measured at distinct points in the force length curve and the length of the toe region is measured from mechanical tests.

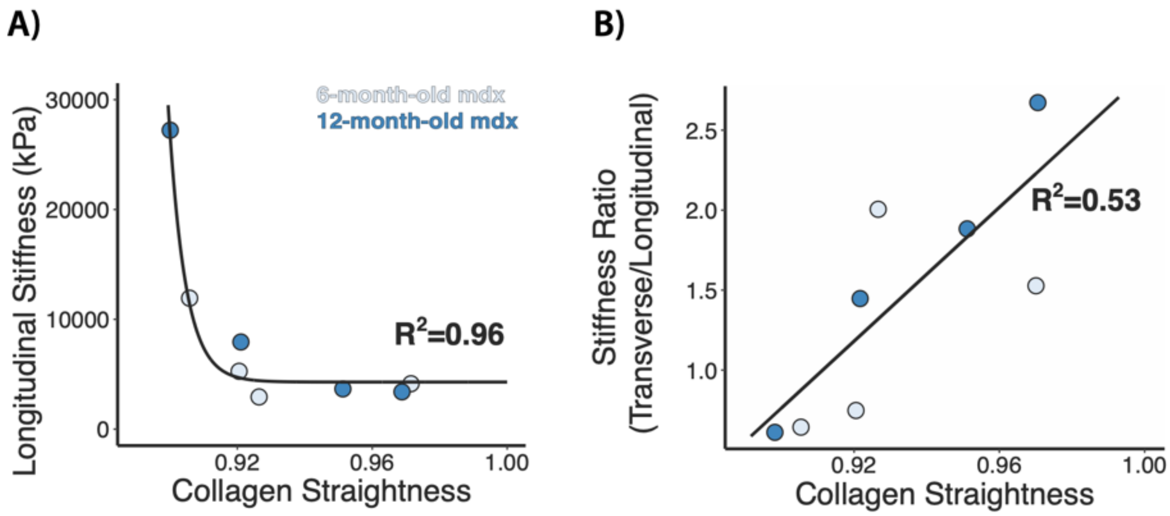

Figure 5.1 Relationships between collagen fiber straightness and longitudinal stiffness (A) and the ratio of transverse to longitudinal stiffness (B).

2. Further characterization of diaphragm muscle ECM

While our framework focused on collagen microstructure, we did not account for differences in collagen subtypes, or directly quantify intramuscular collagen architecture. In our models, we used a single fiber material to represent collagen within the ECM, but the ratio of type I/III collagen is implicated in fibrosis.[55] In our SEM imaging we characterized epimuscular collagen organization, but our coupled modeling framework highlighted the importance of intramuscular collagen organization. Thus, it would be impactful to directly quantify collagen microstructure within the intramuscular ECM (endo/perimysium) and the distribution of key fibrillar collagens (type I and III).

***Intramuscular collagen microstructure*.** Previous studies in diaphragm muscle, did not find a significant difference in intramuscular collagen fiber alignment between *mdx* and WT mice from images in the longitudinal/along-muscle fiber direction plane.[126] We were initially interested in visualizing the intramuscular ECM from the transverse plane, but our preliminary studies highlighted several challenges. From SEM images of intact tissue samples, we saw that collagen fibers were organized in layers surrounding muscle fibers as expected, but it was difficult to discern collagen and muscle fibers to quantify their structure without digesting muscle fibers, as performed for imaging the epimysium (**Fig. 5.2A**). Previous SEM imaging has shown collagen fiber organization in the transverse plane of muscle samples but was performed in much larger muscles from larger animal models.[25,26] However, due to the thin nature of the diaphragm muscle tissue our samples lost their 3-D integrity after the decellularization. We also performed transmission electron microscopy on some diaphragm muscle samples and saw collagen fibers both in and out of the plane (**Fig. 5.2B**). Thus, we tried to image in the longitudinal plane with SEM by sectioning along the muscle fiber direction, but issues with contrast between the resin and digested tissue made it difficult to visualize fibers. We also applied second harmonic generation in intact tissue samples, aiming to image both muscle fibers and collagen fibers through the full thickness of the samples. While we saw similar collagen arrangements in the epimysium to what we measured from SEM (**Fig. 5.2C**), signal was lost through the sample thickness. Thus, future studies can focus on applying more advanced multiphoton imaging techniques used to visualize three dimensional structures[143,144] or leverage additional imaging techniques such as micro-computed tomography to characterize collagen distribution.[145]

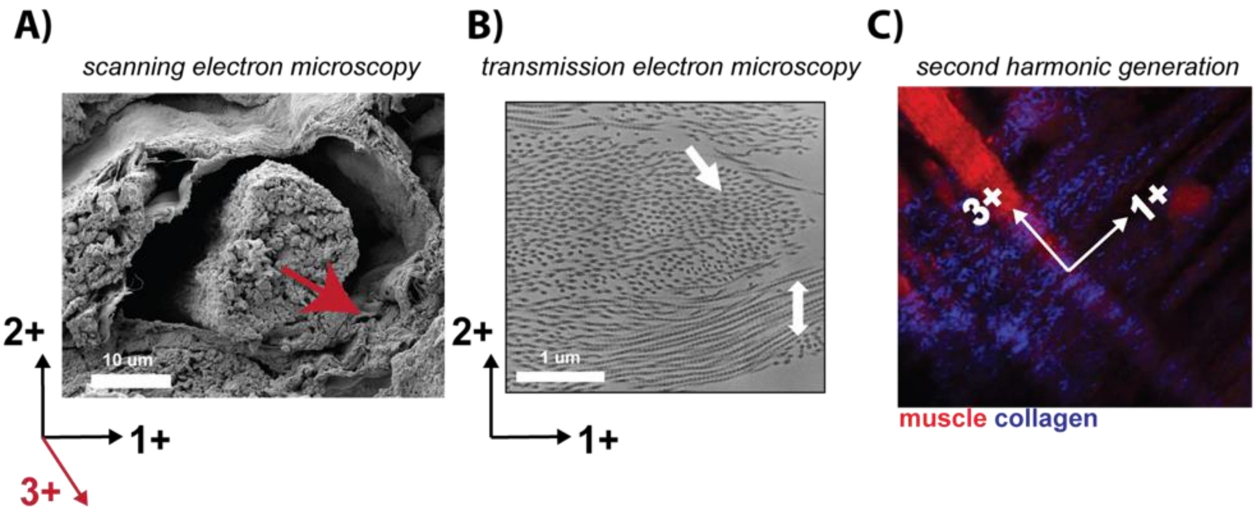

Figure 5.2: A) Preliminary imaging to characterize intramuscular collagen fibers in diaphraghm mucle tissue. A) Scanning electron microsocpy (SEM) of intact muscle samples shows collagen surrounding muscle fibers. B) Transmission electron microscopy (TEM) shows collagen fibers both in and out of the imaging plane. C) Second harmonic generation (SHG) of tissue surface shows collagen fibers oriented transverse to muscle fibers.

Collagen fiber types: Polarized light imaging has been used to visualize collagen fibers from picrosirius red stained imaging, due to collagen's natural birefringence. Further, differences in color are often used to estimate the density or type of collagen fibers, with red regions corresponding with more type I/densely packed collagen and green regions corresponding with more type III/loosely packed collagen. Thus, to estimate collagen type/density we imaged the picrosirius red stained cross-sections from chapter four under polarized light (**Fig. 5.3A**). From those images, we measured the amount of red and green pixels to calculate the percentages of collagen (total, red, green) within the total sample area and each ECM layer (epimuscular, intramuscular). We found greater percentages of total red collagen in the *mdx* images compared with the WT, similar to the ECM area fractions calculated from the brightfield images. This trend was also seen in the intramuscular region (**Fig. 5.3B**). However, differences in the green collagen percentages were not observed (**Fig. 5.3C**). This suggests that collagen within the diaphragm muscle

ECM is more densely packed, with increased densely packed collagen in *mdx* tissue. However, polarized light imaging can be highly sensitive to changes in polarizer angle[146,147] and this analysis had a low sample size (n=3 *mdx* images, n=4 WT images). To increase confidence in our findings, more samples are required, and further studies should be done to specifically stain for collagen type using immunohistochemistry[57] or measure mRNA levels from tissue samples.[56]

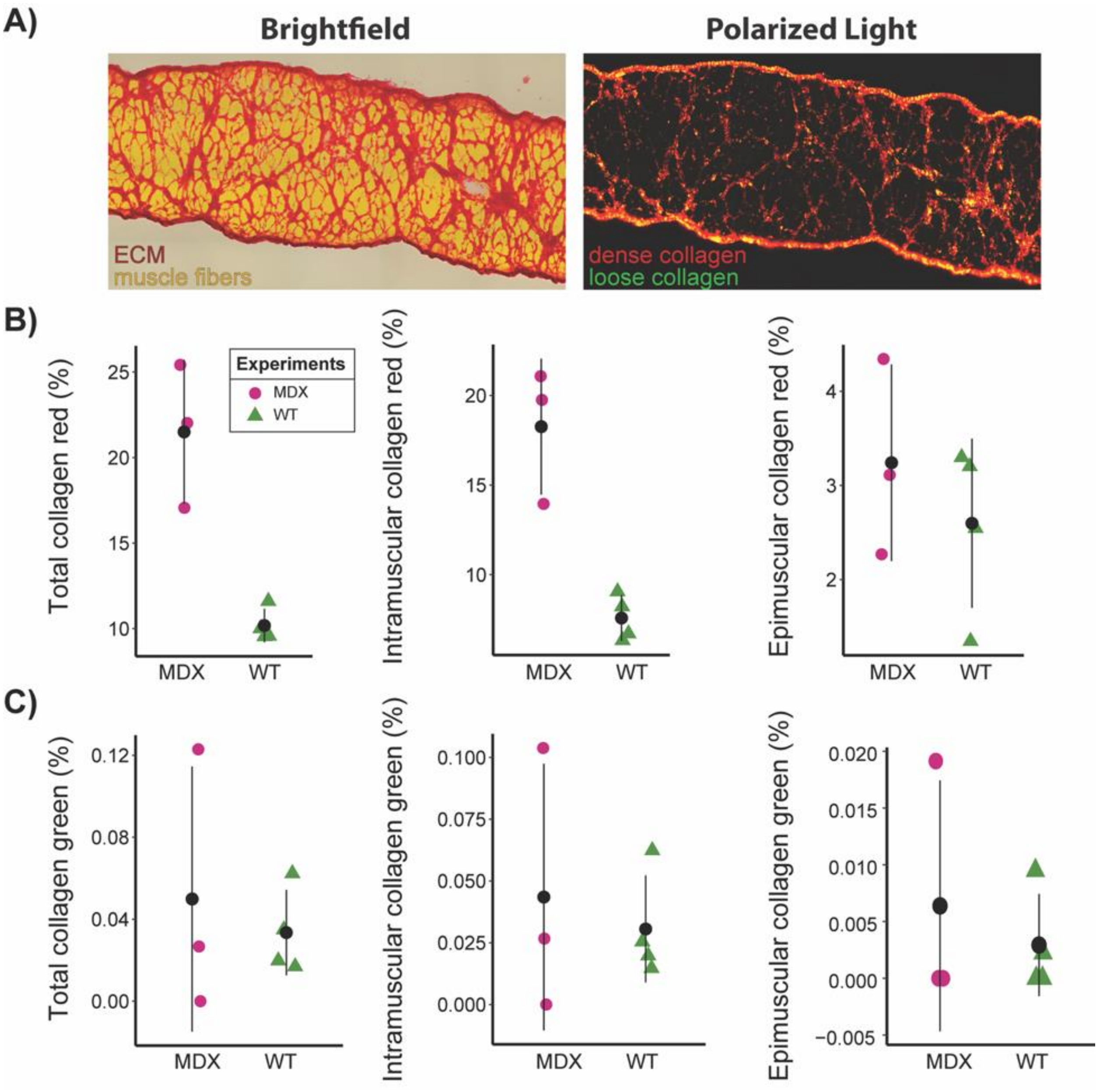

Figure 5.3: A) 6-month mdx mouse diaphraghm muscle cross-section stained with picrosirius red and imaged under brightfield (left) and polarized light (right). B) Measurements of dense/red collagen in total sample (left), intramuscular area (middle) and epimuscular area (right). C) Measurements of loose/green collagen in total sample (left), intramuscular area (middle) and epimuscular area (right).

3. Extensions to intramuscular modeling framework

A challenge with micromechanical modeling at the tissue level is validating model predictions with measurements at a higher scale. Now that our intramuscular model predictions are validated, we can incorporate additional features to refine our representation of collagen fiber microstructure and probe specific questions about the role of the ECM on force generation.

Collagen fiber directions**:** In the intramuscular models in chapter four, we accounted for the distribution of collagen fibers but assigned the primary orientation in the muscle fiber direction for all ECM elements. However, our models suggest that collagen primarily aligns in the cross-muscle fiber direction and previous studies show a helical arrangement of collagen surrounding muscle fibers.[25,26] By assigning individual fiber directions within each ECM element we can further examine the effects of variations in collagen fiber directions on tissue properties. In previous skeletal muscle models, computational fluid dynamics has been used to assign muscle fiber directions,[148] and a similar technique was applied for collagen fiber directions in micromechanical models.[74] To apply these methods in our intramuscular models, we defined inlet and outlet surfaces on ECM elements on opposing surfaces and prescribed a dilation to the inlet, with zero dilation assigned to the outlet. Newtonian materials were assigned to the muscle and ECM elements, with the bulk modulus of the muscle elements set several orders of magnitude greater than the ECM elements to guide fluid flow through the ECM. After the fluid dynamics simulation, fluid velocities were output for each ECM element and used to determine the magnitude and orientation (**Fig. 5.4A**). The fluid velocities were then used to assign material axes within each ECM element (**Fig. 5.4B**). With the inlet and outlet surfaces assigned on the +1 and -1 faces of the model, collagen fiber directions replicated a helical distribution seen in the literature. By varying the inlet and outlet surfaces we can then account for variation along the muscle fiber direction (+3) and compare the effects on tissue stresses and strains.

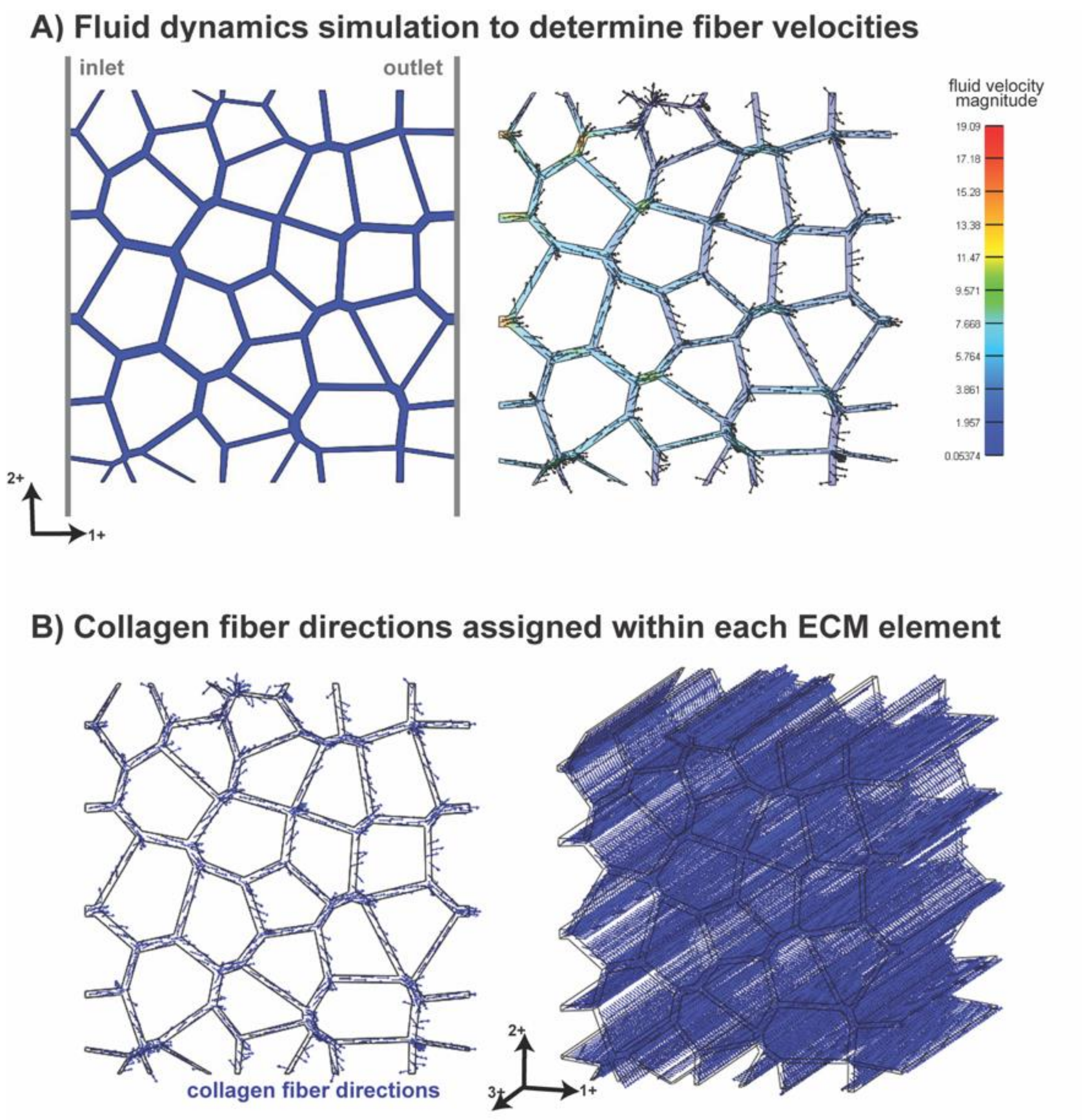
A) Fluid dynamics simulation to determine fiber velocities

B) Collagen fiber directions assigned within each ECM element

Figure 5.4: Fluid velocities within ECM elements from fluid dynamics simulation (A) used to assign individual collagen fiber directions (B).

***Transmembrane linkages*:** In previous micromechanical models, springs were used to account for transmembrane protein linkages between muscle fibers and ECM.[16] To model the loss of dystrophin in DMD, springs were then randomly deleted and the influence of transmembrane protein density on macroscopic shear properties was dependent on the stiffness of the ECM.[16] Our models account for more complexity within the ECM, allowing us to now examine the interplay between collagen microstructure and membrane damage. With our framework we can also simulate complex loading scenarios and test the effects of dystrophin loss on bulk tissue properties. We implemented springs in our intramuscular models by repeating nodes shared between ECM and muscle elements, assigning one node to either element, and connecting them with a linear spring (**Fig. 5.5A**). We used discrete element sets to define the spring pairs and the force-displacement relationships governing their behaviour, scaling the spring stiffness to match the validated tissue level properties in the intramuscular models. By measuring the displacements between spring node pairs, we can then calculate the change in length of the spring to determine membrane strains.[16] From preliminary equibiaixal simulations we saw that the springs primarily lengthened in the cross-muscle fiber direction (+1) (**Fig. 5.5B**). This suggests that transmembrane proteins primarily contribute to cross-muscle fiber properties, which is where we saw differences in *mdx* and WT tissue properties. Thus, the loss of dystrophin in DMD may contribute to these differences in cross-muscle fiber properties due to impact of membrane weakening on cross-muscle fiber strains. To further investigate this, we can examine the role of transmembrane protein density in both our *mdx* and WT models under distinct loading conditions (**Fig. 5.5C**).

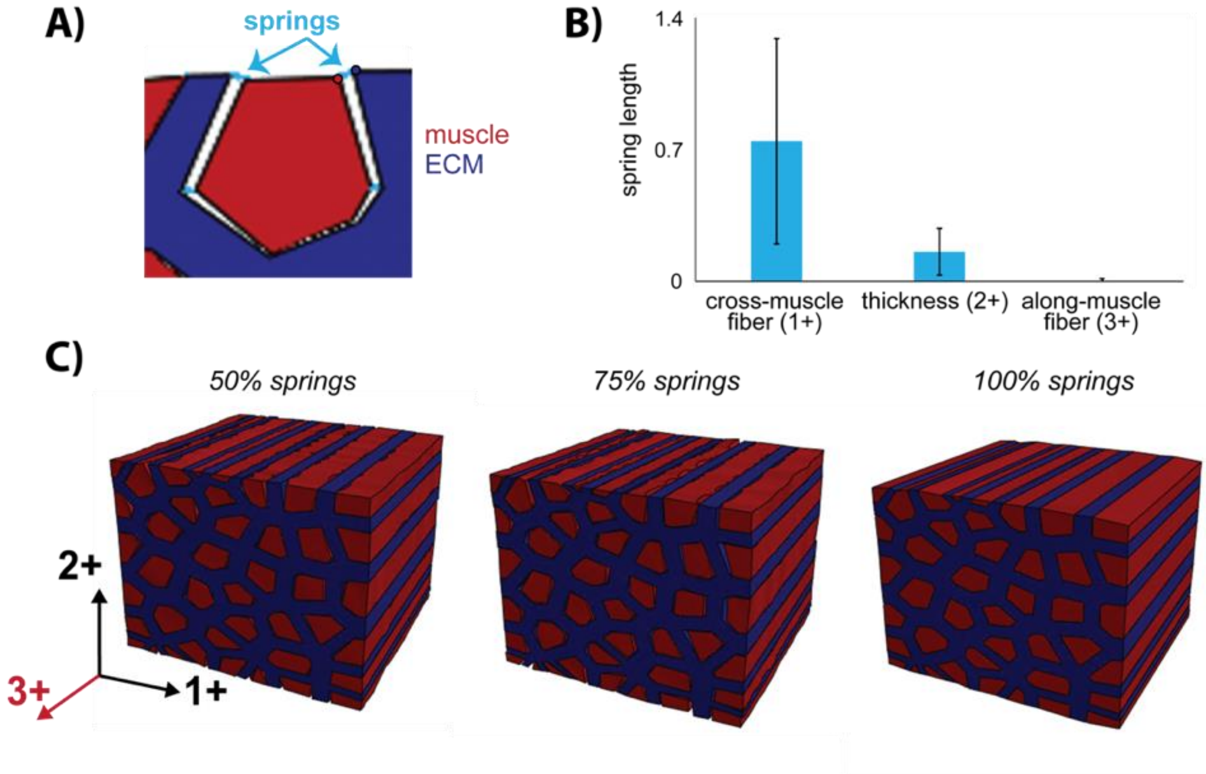

Figure 5.5 A) Springs connecting ECM and muscle nodes. B) Spring length during equibiaxial simulations. C) Variation in density of transmembrane proteins.

Shear loading**:** The ECM is essential for transmitting forces laterally through shearing between muscle fibers and ECM.[113–115] Lateral force transmission is severely impaired in *mdx* mice[114] and previous micromechanical models focused on examining the role of tissue microstructure on macroscopic shear properties. These models revealed transversely anisotropic behavior at the muscle fascicle level,[15] and found that the effect of structural changes such as increased ECM area fraction was highly dependent on the stiffness of the ECM.[76] By simulating shear loading with our updated framework, we can now examine how collagen microstructure influences transverse isotropy. To do so, we implemented periodic boundary conditions based on the shear macroscopic deformation gradient (Equation 5.1). Additionally, we can simulate shear loading while varying the transmembrane protein density to examine how transmembrane proteins influence lateral force transmission. From preliminary simulations we see higher shear strains within the ECM regions compared with muscle regions, and when accounting for transmembrane linkages we see sliding between muscle and ECM regions (**Fig. 5.6**). Further analysis can focus on characterizing how changes in microstructure influence strain distributions.

$$F_{1-3}^{macro} = \begin{bmatrix} 1 & 0 & 0 \\ 0 & 1 & 0 \\ -k & 0 & 1 \end{bmatrix}$$

Equation 5.1

$$u_3^{face^{1+}} = -k\ell_3 + u_3^{face^{1-}}, u_3^{face2+} = u_3^{face2-}, u_3^{face1+} = u_3^{face1-}$$

Equation 5.2

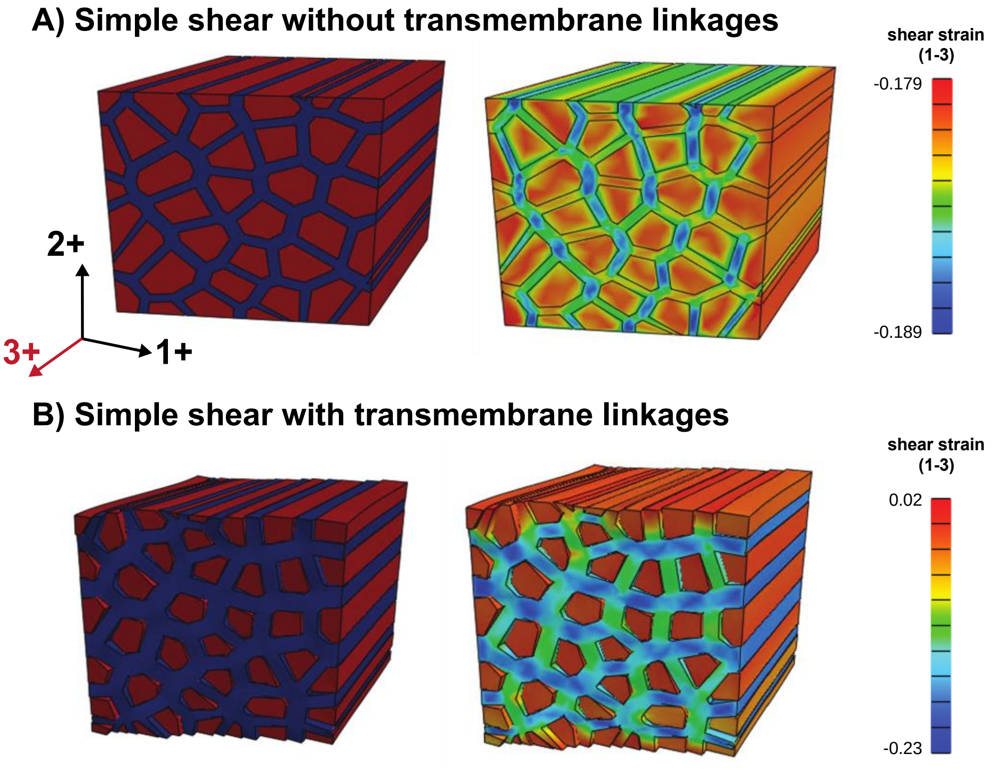

*Figure 5.6**:** A) 1-3 simple shear loading simulation. B) Shear loading with transmembrane proteins connecting muscle and ECM nodes.*

5.4 Future Directions

The development of fibrosis has deleterious impacts in skeletal muscle from the cellular to whole muscle levels. While my research has focused on the tissue level, our findings raise interesting questions about the role of collagen microstructure on complex cellular dynamics during fibrosis (1) and alterations in force generation during muscle dysfunction (2). Thus, exciting future directions could focus on the multiscale implications of collagen organization and seek to answer the following:

1. How does collagen organization influence the progression of fibrosis?

Structural, mechanical, and chemical properties of the ECM contribute to a feed-forward cycle in fibrosis, where fibroblast and myofibroblast behaviors are dependent on local cues.[25,35,46,52,53] Our current framework allows us to predict mechanical properties such as strains and stiffness but does not account for dynamic cellular responses to these stimuli. To address questions at the cellular/biomechanical interface and examine how collagen microstructure contributes to the progression of fibrosis we can leverage agent-based modeling techniques. Agent-based models (ABMs) allow us to simulate the recruitment and cellular behaviors of key inflammatory cells and their interactions with native muscle cells,[149,150] and previous 2-D models of *mdx* lower limb muscle found that increased ECM stiffness was not explained by total amount of collagen alone.[17] However, previous models did not account for structural parameters within the ECM or mechanosensitive behaviors.

To examine the role of collagen microstructure on cellular dynamics we could couple our intramuscular micromechanical models with ABMs that match their 3-D geometries. Agent behaviors from previous ABMs of DMD could be adapted[150] with ECM elements now storing **mechanical parameters:** 1st principle strain (magnitude and direction) and effective stiffness, **structural parameters**: collagen alignment, orientation, straightness, and crosslinking, and **compositional parameters:** collagen I/III density, residual ground matrix density (elastins, PGs/GAGs). Fibroblast and myofibroblast behaviors would then scale based on mechanical cues, with collagen deposited in the local strain direction. The ABM and micromechanical models would then be coupled to simulate disease progression. The micromechanical model would simulate *in vivo* contraction and output local strains and effective stiffness in each ECM element. The ABM would simulate remodeling and predict new microstructure (collagen alignment, direction, density of each ECM component) (**Fig. 5.7**). With this framework we could track the progression of diaphragm muscle fibrosis with more specific metrics beyond collagen amount (i.e. collagen alignment, orientation, cross-linking) and predict relationships between fibrotic tissue structure and muscle dysfunction. Further, we could conduct *in silico* experiments to predict the role of biochemical and mechanical stimuli on respiratory insufficiency and therapies. For example, we can modify *in vivo* strains, simulating mechanical intervention by altering the boundary conditions in the mechanical model and simulate the effects of anti-fibrotic drug therapies by decreasing pro-inflammatory cytokine levels in the ABM. These perturbations would allow us to compare the relative impacts of mechanical and chemical cues on regeneration and fibrosis and predict an optimal timing for intervention.

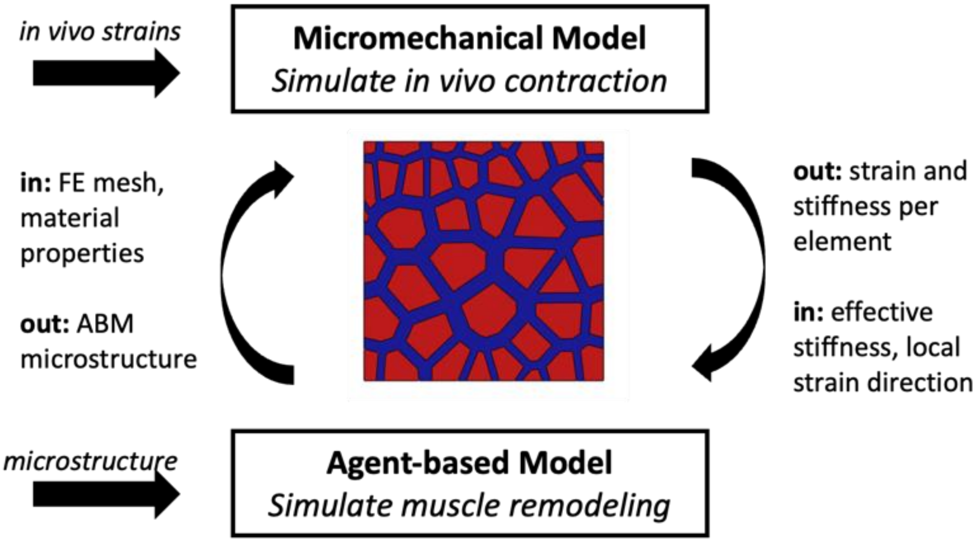

*Figure 5.7**:** Coupled modeling framework where micromechanical model simulates in vivo contraction and agent based model simulates muscle remodeling.*

2. How does collagen organization influence muscle function?

The development of fibrosis contributes to muscle dysfunction and decreases mobility and quality of life across a range of neurological impairments. The ECM's contribution to passive muscle properties is well established[123] and recent studies highlight its role in mediating active forces by regulating intramuscular pressure.[151] Thus, we must consider how noncontractile fibrotic tissue alters the generation of both passive and active muscle forces to improve treatment and rehabilitation programs. While our framework focused on changes in tissue-level properties, we can apply similar methods to bridge gaps between tissue-level measurements and whole-muscle level function.

To investigate how collagen microstructure contributes to force generation we could first measure *in vivo* passive and active force-length relationships in whole muscle.[152,153] After live experiments, the whole muscle could be explanted to perform *ex vivo* uniaxial tests before and after digesting muscle cells to estimate the contribution of the ECM to passive force.[138] The digested muscle could be used to image ECM microstructure (collagen fiber direction, alignment),[127,154] with the intact contralateral muscle used to image muscle architecture (3D geometry, muscle fiber directions)[67,69] Finite element models could be generated to replicate the 3D muscle geometry, with the material properties accounting for local fiber directions and distributions based on our imaging. We could then simulate deformations from the mechanical tests and utilize our data for model calibration and validation. This framework would allow us to examine how microstructural parameters (collagen orientation, alignment) contribute to regional variations in tissue properties (stress, strains) at the muscle level and predict relationships between muscle architecture and collagen microstructure. We could then apply these methods in other muscle groups and animal models of fibrosis to predict relationships between alterations in collagen microstructure and muscle function.[155] Further, we could perform *in silico* experiments to identify therapeutic targets by simulating changes in microstructure (ie. collagen amount, alignment) and mechanical interventions (ie. passive stretch) and compare their influence on model outputs (ie. stiffness).

5.5 Final Remarks

While I may be ending with my PhD with more questions than I began with, we found that, indeed, the complex organizational structure of collagen fibers helps explain the lack of correlation between collagen amount and tissue stiffness in dystrophic muscle.[14,16,17] My investigations into the role of collagen microstructure on passive muscle mechanics have also highlighted the importance of considering collagen organization within distinct ECM layers and *in vivo* loads sustained by specific muscle groups. By coupling multiscale mechanical models with experiments, we also show the capability of modeling to contextualize previous experimental findings, predict properties that cannot be measured, and propose new hypotheses. This framework can be applied to further examine collagens' role in passive muscle mechanics during additional impairments, in other muscle groups, and across scales. In sum, I have certainly learned that the journey from structure to function is complex and can be wavy at times, but it is also filled with exciting findings and new directions.

Be strong, be fearless, be beautiful.

And believe that anything is possible when you
have the right people there to support you.

—Misty Copeland

Appendices

Chapter 3 Supplemental Materials

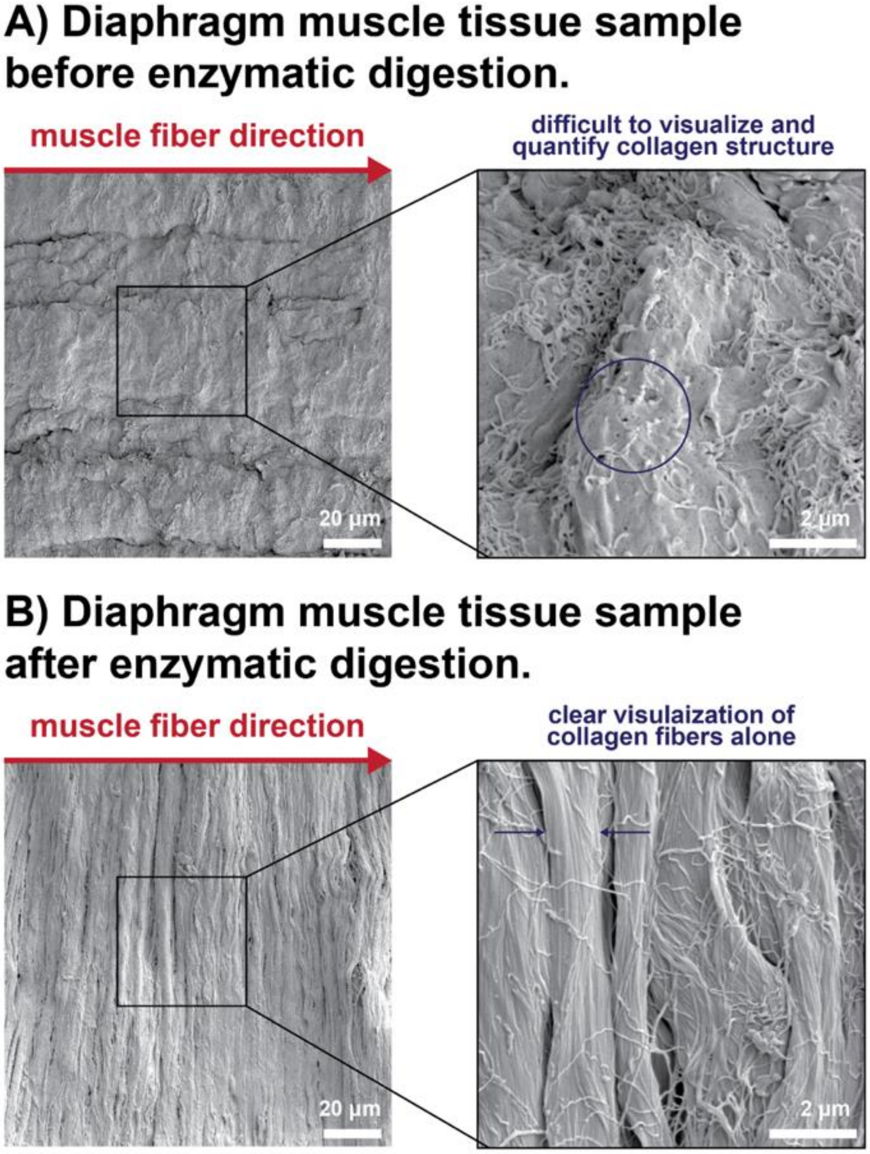

Supplemental Materials 3.1: (A) Sample of intact diaphragm muscle tissue excised from 3-month-old *mdx* mouse and prepared for Scanning Electron Microscopy (SEM) imaging. SEM images of the surface of the sample corresponding to the epimysium at 1kX (left) and 15kX (right) show that it is difficult to visualize collagen structure. (B) Sample of diaphragm muscle tissue excised from the same 3-month-old *mdx* mouse as in A after enzymatic digestion to eliminate muscle fibers and additional ECM components. SEM images of the surface of the sample corresponding to the epimysium at 1kX (left) and 15kX (right) show that the collagen fibers can be clearly visualized after.

A) Test images varying collagen fiber direction (0°<cfd<90°) with strength of alignment held constant (SA=1).

B) Test images varying strength of alignment (0.92<SA<0.99) with collagen fiber direction held constant (cfd=90°).

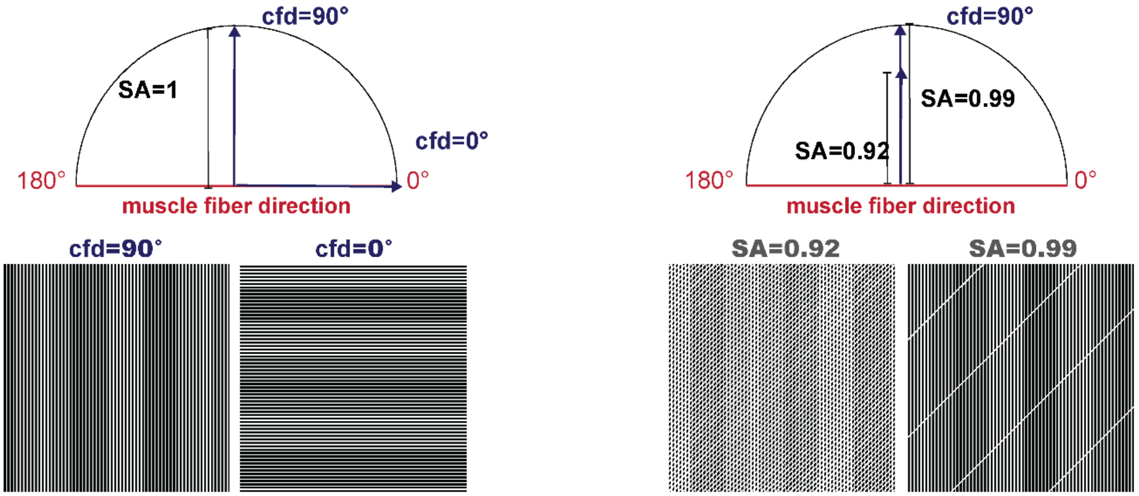

C) Error in collagen fiber direction when varying the number of image windows.

D) Error in strength of alignment when varying the number of image windows.

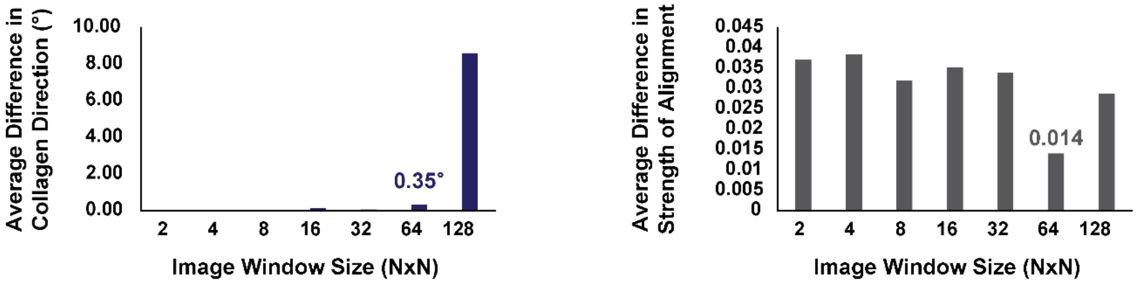

Supplemental Figure 3.2: To validate the image processing algorithm and determine the appropriate subregion size, we first used our image processing algorithm with two manually-generated sets of test images of dark lines that approximated collagen fibers. (A) In the first image set, we varied collagen (line) direction over the range *0-90°* while holding strength of alignment constant ($SA_{known}=1$). (B) In the second set, we varied strength of alignment over the range *0.92-0.99* with collagen direction constant ($cpd_{known}=90°$). To test the sensitivity of our algorithm to the image subregion size, we also varied the number of image subregions (*2x2*) and calculated the error between the known collagen direction and strength of alignment in our test images vs. the values determined by our image processing algorithm. (C) As we increased the number of image subregions, error in collagen direction increased. (D) Error in strength of alignment was minimized at the *64x64* subregion size. Based on this analysis, we selected the *64x64* subregion size, which yielded a collagen direction error of *0.35°* and a strength of alignment error of *0.014*.

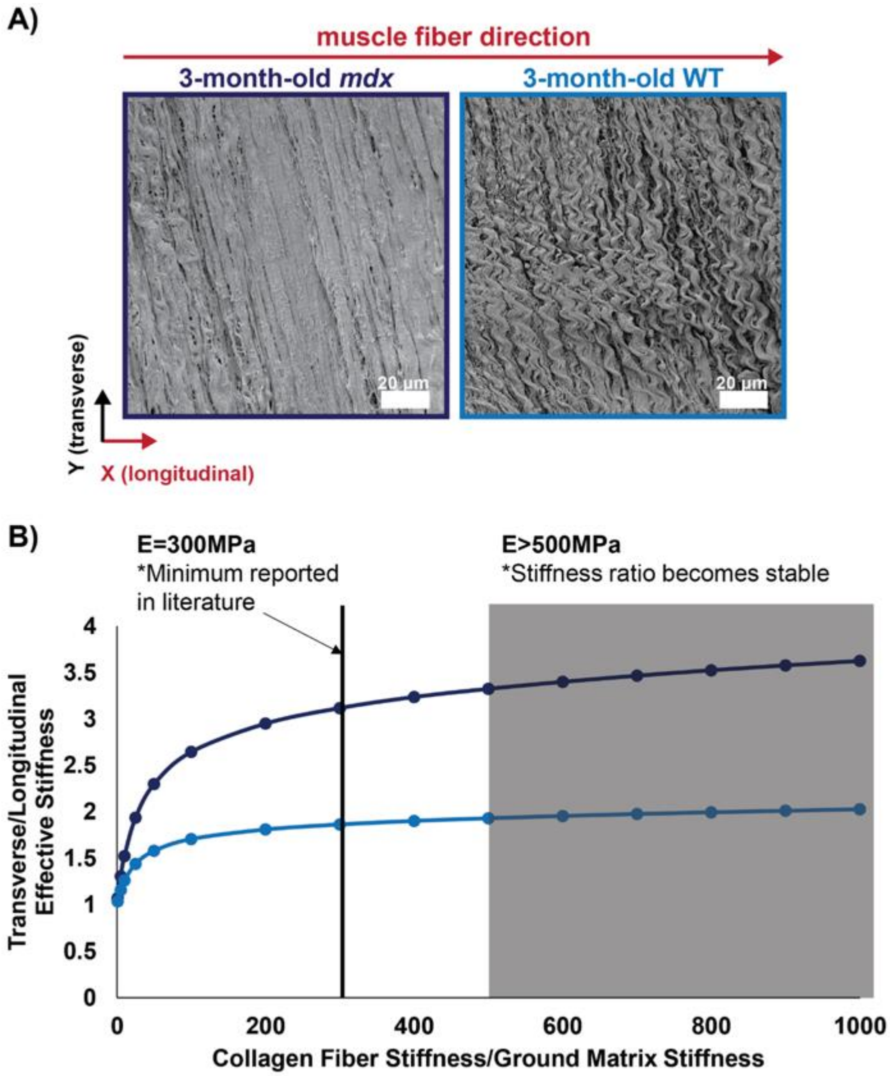

Supplemental Materials 3.3: A wide range of values for collagen fiber stiffness are reported in the literature, varying from 300 MPa-12 GPa[156–158] and are dependent on the mechanical testing conditions. Estimates for ground matrix stiffness also have a wide range, varying from 0.01-1 MPa.[107,159] These material parameters are often fit to experimental data. In this study we were specifically interested in the influence of collagen fiber organization on tissue level properties alone. Therefore, we varied collagen fiber stiffness relative to ground matrix stiffness to determine the sensitivity of our model outputs to the ratio of E/c_1. We held ground matrix stiffness and bulk modulus constant ($c_1=1$ MPa, $k=100{,}000$ MPa) and varied the collagen fiber modulus relative to the ground matrix stiffness ($1<E/c_1<1000$). We used FE models generated from scanning electron microscopy (SEM) images of 3-month-old *mdx* and 3-month-old WT mice (A) to test the sensitivity of the models to collagen fiber stiffness and compared the model output of effective stiffness ratio (*transverse/longitudinal effective stiffness*) (B). As we increased $E/c1$, the difference in effective stiffness ratio between the models increased. However, at approximately $E/c_1=500$ the influence of collagen fiber stiffness on effective stiffness ratio stabilized. Therefore, we selected $E/c_1=800$ which is within the range of reported values and where the influence of collagen fiber stiffness stabilizes.

A) Simplified images varying collagen fiber direction (0°<cfd<85°) with collagen fiber straightness held constant (Ps=1,0.85).

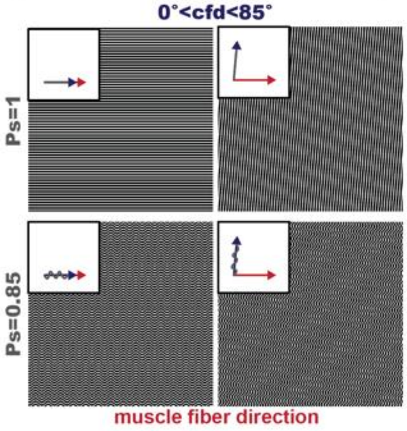

B) Simplified images varying collagen fiber straightness (0.589<Ps<0.997) with collagen fiber direction held constant (cfd=90°,70°).

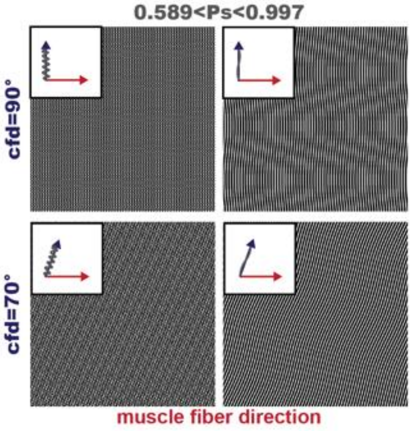

C) Simplified imaged based FE model reveals exponential relationships between collagen direction and tissue stiffness.

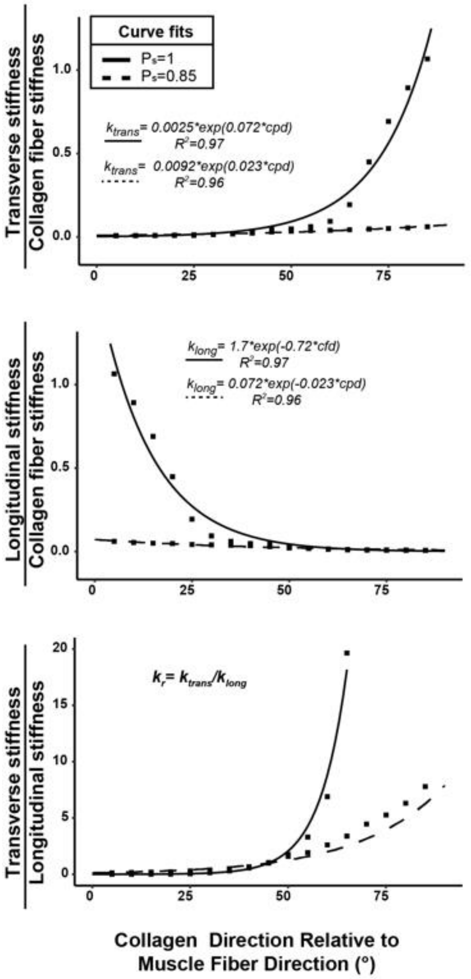

D) Simplified image based FE model reveals power law relationships between collagen straightness and tissue stiffness.

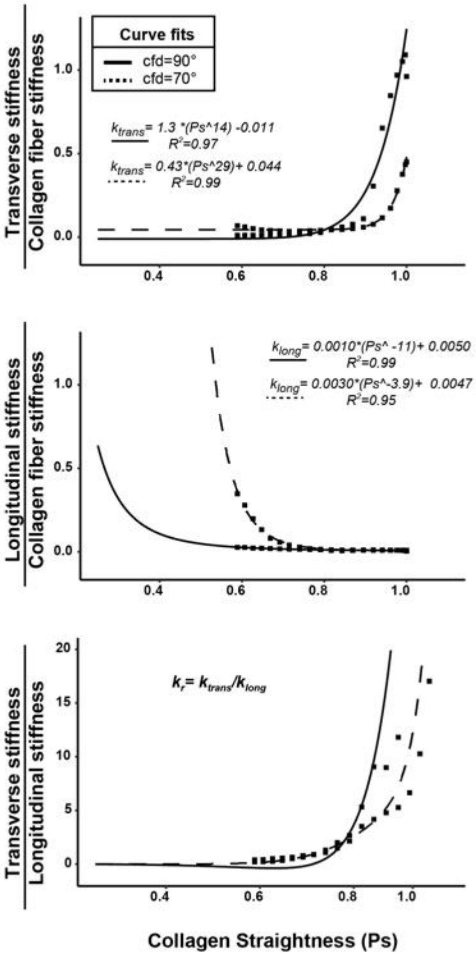

Supplemental Materials 3.4: (A) First, we varied collagen fiber direction ($0° < cfd < 85°$), with collagen fiber straightness constant at 1.0 and then 0.85, since the straightness parameters from SEM images fell within this range. (B) Next, we varied collagen fiber straightness ($0.589 < Ps < 0.997$) while holding fiber direction constant at $90°$ and then $70°$, since the collagen fiber directions from SEM images fell within this range. (C) We generated FE models from each simplified image in A and plotted effective transverse stiffness vs. collagen fiber direction (top), effective longitudinal stiffness vs. collagen fiber direction (middle), and effective stiffness ratio vs. collagen fiber direction (bottom). We fit exponential relationships for effective transverse and longitudinal stiffness with $Ps=1$ and $Ps=0.85$ and then divided the curve fits for transverse and longitudinal stiffness for the effective stiffness ratio. (D) We generated FE models from each simplified image in B and plotted effective transverse stiffness vs. collagen fiber straightness (top), effective longitudinal stiffness vs. collagen fiber straightness (middle), and effective stiffness ratio vs. collagen fiber straightness (bottom). We fit power law relationships for effective transverse and longitudinal stiffness with $cfd=90°$ and $cfd=70°$, and then divided the curve fits for transverse and longitudinal stiffness for the effective stiffness ratio. *The following material properties were held constant for all simplified image-based models: $(E=800MPa,\ c1=1MPa,\ K=100\ MPa\ \beta=3,\ \lambda_0=1.01)$.

Chapter 4 Supplemental Materials

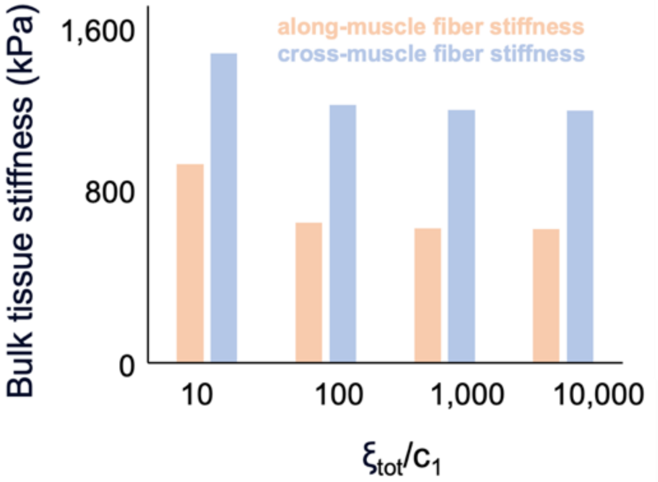

Supplemental Fig 4.1: Analysis of the effects of the ratio of total collagen fiber stiffness to ground matrix stiffness (ξ_{tot} /c_1) within the ECM material. Model predictions of bulk tissue stiffness during along-muscle fiber lengthening, cross-muscle fiber lengthening (ALCL) simulation were compared with varying ξ_{tot} /c_1. The effects of the ratio of total collagen fiber stiffness to ground matrix stiffness stabilized when (ξ_{tot} =1000c_1) and was maintained for all simulations.

Supplemental Table 4.1: Experimentally measured tissue properties used to narrow down parameter values during model calibration (biax, *in vivo*, uniax cross) and validate model predictions (uniax along)

Loading scenario	**Experiment measurements**		**Model parameters**
Biax: *Along-muscle fiber lengthening, cross-muscle fiber lengthening*	*mdx*	k_{11}=1.2e3 ± 8.2e2 kPa k_{33}= 5.8e2 ± 3.4e2 kPa k_{11}/k_{33} = 2.4 ±1.4	200kPa<k^{coll}<800kPa 0.1<$cfdist^{intra}$ <0.8
	WT	k_{11}= 4.6e2 ± 4.4e2 kPa k_{33}= 4e2 ± 1.4e2 kPa k_{11}/k_{33} = 1.1 ± 0.90	100kPa<k^{coll}<600kPa 0.1< $cfdist^{intra}$ <0.7
In vivo: *Along-muscle fiber shortening, cross-muscle fiber lengthening*	*mdx*	σ_{11}= 3.8 ± 0.79 kPa σ_{33}= -1.5 ± 0.82 kPa	200kPa<k^{coll} <300kPa 0.1< $cfdist^{intra}$ <0.2
	WT	σ_{11}= 2.5 ± 2.9 kPa σ_{33}= -1.5 ± 0.82 kPa	k^{coll} =200kPa 0.2< $cfdist^{intra}$ <0.7
Uniax cross: *Cross-muscle fiber lengthening*	*mdx*	k_{11}= 1.2e3 ± 5.8e2 kPa	k^{coll}=200kPa 0.125< $cfdist^{intra}$ <0.175
	WT	k_{11}= 1.1e3 ± 1.4e3 kPa	k^{coll}=200kPa 0.2< $cfdist^{intra}$ <0.7
Uniax along: *Along-muscle fiber lengthening*	*mdx*	k_{33}= 4.1e2 ± 2e2 kPa	k^{coll}=200kPa 0.125< $cfdist^{intra}$ <0.175
	WT	k_{33}= 4.6e2 ± 2.5e2 kPa	k^{coll}=200kPa 0.2< $cfdist^{intra}$ <0.7

Bibliography

1. Emery, A. E. H., Muntoni, F. & Quinlivan, R. C. M. *Duchenne Muscular Dystrophy*. (OUP Oxford, 2015).
2. Hoffman, E. P., Brown, R. H. & Kunkel, L. M. Dystrophin: the protein product of the Duchenne muscular dystrophy locus. *Cell* **51**, 919–928 (1987).
3. Koenig, M. *et al.* Complete cloning of the Duchenne muscular dystrophy (DMD) cDNA and preliminary genomic organization of the DMD gene in normal and affected individuals. *Cell* **50**, 509–517 (1987).
4. Koenig, M., Monaco, A. P. & Kunkel, L. M. The complete sequence of dystrophin predicts a rod-shaped cytoskeletal protein. *Cell* **53**, 219–228 (1988).
5. Monaco, A. P. *et al.* Isolation of candidate cDNAs for portions of the Duchenne muscular dystrophy gene. *Nature* **323**, 646–650 (1986).
6. Rahimov, F. & Kunkel, L. M. The cell biology of disease: cellular and molecular mechanisms underlying muscular dystrophy. *J. Cell Biol.* **201**, 499–510 (2013).
7. Berlowitz, D. J., Wadsworth, B. & Ross, J. Respiratory problems and management in people with spinal cord injury. *Breathe* **12**, 328–340 (2016).
8. Kinnear, W. *et al.* Long-term non-invasive ventilation in muscular dystrophy. *Chron. Respir. Dis.* **14**, 33–36 (2017).
9. Goligher, E. C. *et al.* Mechanical Ventilation–induced Diaphragm Atrophy Strongly Impacts Clinical Outcomes. *Am. J. Respir. Crit. Care Med.* **197**, 204–213 (2017).
10. Hamada, S. *et al.* Indicators for ventilator use in Duchenne muscular dystrophy. *Respir. Med.* **105**, 625–629 (2011).

11. Ciafaloni, E. *et al.* Delayed diagnosis in duchenne muscular dystrophy: data from the Muscular Dystrophy Surveillance, Tracking, and Research Network (MD STARnet). *J. Pediatr.* **155**, 380–385 (2009).
12. Stedman, H. H. *et al.* The mdx mouse diaphragm reproduces the degenerative changes of Duchenne muscular dystrophy. *Nature* **352**, 536–539 (1991).
13. Impaired respiratory function in mdx and mdx/utrn(+/-) mice - PubMed. https://pubmed.ncbi.nlm.nih.gov/21254093/.
14. Smith, L. R. & Barton, E. R. Collagen content does not alter the passive mechanical properties of fibrotic skeletal muscle in mdx mice. *Am. J. Physiol. - Cell Physiol.* **306**, C889–C898 (2014).
15. Sharafi, B. & Blemker, S. S. A micromechanical model of skeletal muscle to explore the effects of fiber and fascicle geometry. *J. Biomech.* **43**, 3207–3213 (2010).
16. Virgilio, K. M., Martin, K. S., Peirce, S. M. & Blemker, S. S. Multiscale models of skeletal muscle reveal the complex effects of muscular dystrophy on tissue mechanics and damage susceptibility. *Interface Focus* **5**, (2015).
17. Virgilio, K. M. *et al.* Computational Models Provide Insight into In Vivo Studies and Reveal the Complex Role of Fibrosis in mdx Muscle Regeneration. *Ann. Biomed. Eng.* (2020) doi:10.1007/s10439-020-02566-1.
18. Bloch, R. J. & Gonzalez-Serratos, H. Lateral force transmission across costameres in skeletal muscle. *Exerc. Sport Sci. Rev.* **31**, 73–78 (2003).

19. Huijing, P. A. Epimuscular myofascial force transmission: a historical review and implications for new research. International Society of Biomechanics Muybridge Award Lecture, Taipei, 2007. *J. Biomech.* **42**, 9–21 (2009).
20. Passerieux, E., Rossignol, R., Letellier, T. & Delage, J. P. Physical continuity of the perimysium from myofibers to tendons: Involvement in lateral force transmission in skeletal muscle. *J. Struct. Biol.* **159**, 19–28 (2007).
21. Birk, D. E. & Mayne, R. Localization of collagen types I, III and V during tendon development. Changes in collagen types I and III are correlated with changes in fibril diameter. *Eur. J. Cell Biol.* **72**, 352–361 (1997).
22. Fridén, J. & Lieber, R. L. Spastic muscle cells are shorter and stiffer than normal cells. *Muscle Nerve* **27**, 157–164 (2003).
23. Lieber, R. L., Runesson, E., Einarsson, F. & Fridén, J. Inferior mechanical properties of spastic muscle bundles due to hypertrophic but compromised extracellular matrix material. *Muscle Nerve* **28**, 464–471 (2003).
24. Ward, S. R. *et al.* Passive mechanical properties of the lumbar multifidus muscle support its role as a stabilizer. *J. Biomech.* **42**, 1384–1389 (2009).
25. Purslow, P. P. & Trotter, J. A. The morphology and mechanical properties of endomysium in series-fibred muscles: variations with muscle length. *J. Muscle Res. Cell Motil.* **15**, 299–308 (1994).
26. Purslow, P. P. Muscle fascia and force transmission. *J. Bodyw. Mov. Ther.* **14**, 411–417 (2010).
27. CiNii Articles - The intramuscular connective tissue matrix and cell/matrix interactions in relation to meat toughness. https://ci.nii.ac.jp/naid/10021226700/.

28. Borg, T. K. & Caulfield, J. B. Morphology of connective tissue in skeletal muscle. *Tissue Cell* **12**, 197–207 (1980).
29. Beekman, C. *et al.* A Sensitive, Reproducible and Objective Immunofluorescence Analysis Method of Dystrophin in Individual Fibers in Samples from Patients with Duchenne Muscular Dystrophy. *PLOS ONE* **9**, e107494 (2014).
30. Lieber, R. L. & Ward, S. R. Cellular mechanisms of tissue fibrosis. 4. Structural and functional consequences of skeletal muscle fibrosis. *Am. J. Physiol. Cell Physiol.* **305**, C241-252 (2013).
31. Lacourpaille, L. *et al.* Effects of Duchenne muscular dystrophy on muscle stiffness and response to electrically-induced muscle contraction: A 12-month follow-up. *Neuromuscul. Disord.* **27**, 214–220 (2017).
32. Murphy, M. M., Lawson, J. A., Mathew, S. J., Hutcheson, D. A. & Kardon, G. Satellite cells, connective tissue fibroblasts and their interactions are crucial for muscle regeneration. *Dev. Camb. Engl.* **138**, 3625–3637 (2011).
33. Jiang, C. *et al.* Notch signaling deficiency underlies age-dependent depletion of satellite cells in muscular dystrophy. *Dis. Model. Mech.* **7**, 997–1004 (2014).
34. Crone, M. & Mah, J. K. Current and Emerging Therapies for Duchenne Muscular Dystrophy. *Curr. Treat. Options Neurol.* **20**, 31 (2018).
35. Guiraud, S. & Davies, K. E. Pharmacological advances for treatment in Duchenne muscular dystrophy. *Curr. Opin. Pharmacol.* **34**, 36–48 (2017).
36. Khirani, S. *et al.* Respiratory muscle decline in Duchenne muscular dystrophy. *Pediatr. Pulmonol.* **49**, 473–481 (2014).

37. Pennati, F. *et al.* Diaphragm Involvement in Duchenne Muscular Dystrophy (DMD): An MRI Study. *J. Magn. Reson. Imaging* **51**, 461–471 (2020).

38. Mauro, A. L. *et al.* Abdominal volume contribution to tidal volume as an early indicator of respiratory impairment in Duchenne muscular dystrophy. *Eur. Respir. J.* **35**, 1118–1125 (2010).

39. Laviola, M., Priori, R., D'Angelo, M. G. & Aliverti, A. Assessment of diaphragmatic thickness by ultrasonography in Duchenne muscular dystrophy (DMD) patients. *PLoS ONE* **13**, (2018).

40. Schepens, T. *et al.* The course of diaphragm atrophy in ventilated patients assessed with ultrasound: a longitudinal cohort study. *Crit. Care* **19**, (2015).

41. Beck, J. *et al.* Diaphragmatic function in advanced Duchenne muscular dystrophy. *Neuromuscul. Disord.* **16**, 161–167 (2006).

42. Gillies, A. R., Smith, L. R., Lieber, R. L. & Varghese, S. Method for Decellularizing Skeletal Muscle Without Detergents or Proteolytic Enzymes. *Tissue Eng. Part C Methods* **17**, 383–389 (2011).

43. Paxton, S., Peckham, M. & Knibbs, A. The Leeds Histology Guide. (2003).

44. CHAFFEY, N. Alberts, B., Johnson, A., Lewis, J., Raff, M., Roberts, K. and Walter, P. Molecular biology of the cell. 4th edn. *Ann. Bot.* **91**, 401 (2003).

45. Henry, C. C. *et al.* Spatial and age-related changes in the microstructure of dystrophic and healthy diaphragms. *PLOS ONE* **12**, e0183853 (2017).

46. Hinz, B. *et al.* Recent Developments in Myofibroblast Biology. *Am. J. Pathol.* **180**, 1340–1355 (2012).

47. Petroll, W. M. & Ma, L. Direct, dynamic assessment of cell-matrix interactions inside fibrillar collagen lattices. *Cell Motil.* **55**, 254–264 (2003).
48. Dickinson, R. B., Guido, S. & Tranquillo, R. T. Biased cell migration of fibroblasts exhibiting contact guidance in oriented collagen gels. *Ann. Biomed. Eng.* **22**, 342–356 (1994).
49. El-Mohri, H., Wu, Y., Mohanty, S. & Ghosh, G. Impact of matrix stiffness on fibroblast function. *Mater. Sci. Eng. C* **74**, 146–151 (2017).
50. Tisler, M. *et al.* Analysis of fibroblast migration dynamics in idiopathic pulmonary fibrosis using image-based scaffolds of the lung extracellular matrix. *Am. J. Physiol.-Lung Cell. Mol. Physiol.* **318**, L276–L286 (2020).
51. Hinz, B. The extracellular matrix and transforming growth factor-β1: Tale of a strained relationship. *Matrix Biol.* **47**, 54–65 (2015).
52. Dittmore, A. *et al.* Internal strain drives spontaneous periodic buckling in collagen and regulates remodeling. *Proc. Natl. Acad. Sci.* **113**, 8436–8441 (2016).
53. Mechanical Strain Stabilizes Reconstituted Collagen Fibrils against Enzymatic Degradation by Mammalian Collagenase Matrix Metalloproteinase 8 (MMP-8). https://journals.plos.org/plosone/article?id=10.1371/journal.pone.0012337.
54. Smith, L. R., Hammers, D. W., Sweeney, H. L. & Barton, E. R. Increased collagen cross-linking is a signature of dystrophin-deficient muscle. *Muscle Nerve* **54**, 71–78 (2016).
55. Shoemaker, C. T., Reiser, K. M., Goetzman, B. W. & Last, J. A. Elevated ratios of type I/III collagen in the lungs of chronically ventilated neonates with respiratory distress. *Pediatr. Res.* **18**, 1176–1180 (1984).

56. Goldspink, G., Fernandes, K., Williams, P. E. & Wells, D. J. Age-related changes in collagen gene expression in the muscles of mdx dystrophic and normal mice. *Neuromuscul. Disord.* **4**, 183–191 (1994).

57. A role for collagen in the pathogenesis of muscular dystrophy? | Nature. https://www.nature.com/articles/284470a0.

58. Drifka, C. *et al.* Periductal stromal collagen topology of pancreatic ductal adenocarcinoma differs from that of normal and chronic pancreatitis. *Mod. Pathol. Off. J. U. S. Can. Acad. Pathol. Inc* **28**, (2015).

59. Brashear, S. E., Wohlgemuth, R. P., Gonzalez, G. & Smith, L. R. Passive stiffness of fibrotic skeletal muscle in mdx mice relates to collagen architecture. *J. Physiol.* **n/a**,.

60. Wohlgemuth, R. P. *et al.* The extracellular matrix of dystrophic mouse diaphragm accounts for the majority of its passive stiffness and is resistant to collagenase digestion. *Matrix Biol. Plus* **18**, 100131 (2023).

61. Boriek, A. M., Kelly, N. G., Rodarte, J. R. & Wilson, T. A. Biaxial constitutive relations for the passive canine diaphragm. *J. Appl. Physiol.* **89**, 2187–2190 (2000).

62. Boriek, A. M., Rodarte, J. R. & Reid, M. B. Shape and tension distribution of the passive rat diaphragm. *Am. J. Physiol.-Regul. Integr. Comp. Physiol.* **280**, R33–R41 (2001).

63. Lopez, M. A. *et al.* Mechanics of dystrophin deficient skeletal muscles in very young mice and effects of age. *Am. J. Physiol. - Cell Physiol.* **321**, C230–C246 (2021).

64. Wallace, C. H. Novel experimental-modeling coupled framework to elucidate the impact of collagen on diaphragm muscle mechanics in Duchenne muscular dystrophy. (University of Virginia).

65. Zajac, F. E. Muscle and tendon: properties, models, scaling, and application to biomechanics and motor control. *Crit. Rev. Biomed. Eng.* **17**, 359–411 (1989).

66. Rajagopal, A. *et al.* Full-Body Musculoskeletal Model for Muscle-Driven Simulation of Human Gait. *IEEE Trans. Biomed. Eng.* **63**, 2068–2079 (2016).

67. Blemker, S. S., Pinsky, P. M. & Delp, S. L. A 3D model of muscle reveals the causes of nonuniform strains in the biceps brachii. *J. Biomech.* **38**, 657–665 (2005).

68. C. Criscione, J., S. Douglas, A. & C. Hunter, W. Physically based strain invariant set for materials exhibiting transversely isotropic behavior. *J. Mech. Phys. Solids* **49**, 871–897 (2001).

69. Knaus, K. R., Handsfield, G. G. & Blemker, S. S. A 3D model of the soleus reveals effects of aponeuroses morphology and material properties on complex muscle fascicle behavior. *J. Biomech.* **130**, 110877 (2022).

70. Fiorentino, N. M. & Blemker, S. S. Musculotendon variability influences tissue strains experienced by the biceps femoris long head muscle during high-speed running. *J. Biomech.* **47**, 3325–3333 (2014).

71. Spyrou, L. A., Brisard, S. & Danas, K. Multiscale modeling of skeletal muscle tissues based on analytical and numerical homogenization. *J. Mech. Behav. Biomed. Mater.* **92**, 97–117 (2019).

72. Spyrou, L. A., Agoras, M. & Danas, K. A homogenization model of the Voigt type for skeletal muscle. *J. Theor. Biol.* **414**, 50–61 (2017).

73. Computational modeling of damage in the hierarchical microstructure of skeletal muscles | Elsevier Enhanced Reader. https://reader.elsevier.com/reader/sd/pii/S1751616122002946?token=B986343D99461C2DF5D6F68C4D4C2F8AB207004929BD6AB89E88EFD405538CA0E3E78BDCE4C63686067DDCC59B400AAC&originRegion=us-east-1&originCreation=20230320215318 doi:10.1016/j.jmbbm.2022.105386.

74. Kuravi, R., Leichsenring, K., Böl, M. & Ehret, A. E. 3D finite element models from serial section histology of skeletal muscle tissue – The role of micro-architecture on mechanical behaviour. *J. Mech. Behav. Biomed. Mater.* **113**, 104109 (2021).

75. He, X. *et al.* Multiscale modeling of passive material influences on deformation and force output of skeletal muscles. *Int. J. Numer. Methods Biomed. Eng.* **38**, e3571 (2022).

76. Virgilio, K. M., Martin, K. S., Peirce, S. M. & Blemker, S. S. Multiscale models of skeletal muscle reveal the complex effects of muscular dystrophy on tissue mechanics and damage susceptibility. *Interface Focus* **5**, 20140080 (2015).

77. Hollingsworth, K. G., Garrood, P., Eagle, M., Bushby, K. & Straub, V. Magnetic resonance imaging in duchenne muscular dystrophy: Longitudinal assessment of natural history over 18 months. *Muscle Nerve* **48**, 586–588 (2013).

78. Ratnovsky, A., Elad, D. & Halpern, P. Mechanics of respiratory muscles. *Respir. Physiol. Neurobiol.* **163**, 82–89 (2008).

79. Impaired respiratory function in mdx and mdx/utrn+/− mice - Huang - 2011 - Muscle & Nerve - Wiley Online Library. https://onlinelibrary.wiley.com/doi/full/10.1002/mus.21848.

80. Ishizaki, M. *et al.* Mdx respiratory impairment following fibrosis of the diaphragm. *Neuromuscul. Disord. NMD* **18**, 342–348 (2008).

81. Louboutin, J. P., Fichter-Gagnepain, V., Thaon, E. & Fardeau, M. Morphometric analysis of mdx diaphragm muscle fibres. Comparison with hindlimb muscles. *Neuromuscul. Disord.* **3**, 463–469 (1993).

82. Boubaker, B., Pato, M. & Pires, E. A finite element model of skeletal muscle. *Virtual Phys. Prototyp.* **1**, 159–170 (2006).

83. van Leeuwen, J. *et al.* Finite element modelling of contracting skeletal muscle. *Philos. Trans. R. Soc. Lond. B. Biol. Sci.* **358**, 1453–1460 (2003).

84. A Framework for Structured Modeling of Skeletal Muscle: Computer Methods in Biomechanics and Biomedical Engineering: Vol 7, No 6. https://www.tandfonline.com/doi/abs/10.1080/10255840412331317398.

85. Otsu, N. A Threshold Selection Method from Gray-Level Histograms. *IEEE Trans. Syst. Man Cybern.* **9**, 62–66 (1979).

86. Lim, Jae S., Two-Dimensional Signal and Image Processing, Englewood Cliffs, NJ, Prentice Hall, 1990, pp. 42-45. in.

87. Bracewell, Ronald N., Two-Dimensional Imaging, Englewood Cliffs, NJ, Prentice Hall, 1995, pp. 505-537. in.

88. Jafari-Khouzani, K. & Soltanian-Zadeh, H. Radon Transform Orientation Estimation for Rotation Invariant Texture Analysis. *IEEE Trans. Pattern Anal. Mach. Intell.* **27**, 1004–1008 (2005).
89. Krause, M., Hausherr, J. M. & Krenkel, W. Computing the fibre orientation from Radon data using local Radon transform. *Inverse Probl. Imaging* **5**, 879 (2011).
90. Schaub, N., Gilbert, R. & Kirkpatrick, S. Electrospun fiber alignment using the Radon Transform. in (2011). doi:10.1117/12.875019.
91. Berens, P. CircStat: A MATLAB Toolbox for Circular Statistics. *J. Stat. Softw.* **31**, 1–21 (2009).
92. Maas, S. A., Ellis, B. J., Ateshian, G. A. & Weiss, J. A. FEBio: finite elements for biomechanics. *J. Biomech. Eng.* **134**, 011005 (2012).
93. Eleswarapu, S. V., Responte, D. J. & Athanasiou, K. A. Tensile Properties, Collagen Content, and Crosslinks in Connective Tissues of the Immature Knee Joint. *PLOS ONE* **6**, e26178 (2011).
94. Hurschler, C., Loitz-Ramage, B. & Vanderby, R. A structurally based stress-stretch relationship for tendon and ligament. *J. Biomech. Eng.* **119**, 392–399 (1997).
95. Reese, S. P., Maas, S. A. & Weiss, J. A. Micromechanical models of helical superstructures in ligament and tendon fibers predict large Poisson's ratios. *J. Biomech.* **43**, 1394–1400 (2010).
96. Weiss, J. A., Gardiner, J. C. & Bonifasi-Lista, C. Ligament material behavior is nonlinear, viscoelastic and rate-independent under shear loading. *J. Biomech.* **35**, 943–950 (2002).

97. Rigby, B. J., Hirai, N., Spikes, J. D. & Eyring, H. The Mechanical Properties of Rat Tail Tendon. *J. Gen. Physiol.* **43**, 265–283 (1959).

98. Muench, J. R., Thelen, D. G. & Henak, C. R. Interfibrillar shear behavior is altered in aging tendon fascicles. *Biomech. Model. Mechanobiol.* **19**, 841–849 (2020).

99. Weiss, J. A., Maker, B. N. & Govindjee, S. Finite element implementation of incompressible, transversely isotropic hyperelasticity. *Comput. Methods Appl. Mech. Eng.* **135**, 107–128 (1996).

100. Hurschler, C., Provenzano, P. P. & Vanderby, R. Scanning electron microscopic characterization of healing and normal rat ligament microstructure under slack and loaded conditions. *Connect. Tissue Res.* **44**, 59–68 (2003).

101. Hansen, K. A., Weiss, J. A. & Barton, J. K. Recruitment of tendon crimp with applied tensile strain. *J. Biomech. Eng.* **124**, 72–77 (2002).

102. Lake, S. P., Miller, K. S., Elliott, D. M. & Soslowsky, L. J. Effect of fiber distribution and realignment on the nonlinear and inhomogeneous mechanical properties of human supraspinatus tendon under longitudinal tensile loading. *J. Orthop. Res. Off. Publ. Orthop. Res. Soc.* **27**, 1596 (2009).

103. Stender, C. J. *et al.* Modeling the effect of collagen fibril alignment on ligament mechanical behavior. *Biomech. Model. Mechanobiol.* **17**, 543–557 (2018).

104. Curve Fitting Toolbox User's Guide. 804.

105. Hakim, C. H. *et al.* An improved method for studying mouse diaphragm function. *Sci. Rep.* **9**, 19453 (2019).

106. Margulies, S., Lei, G., Farkas, G. & Rodarte, J. Finite-element analysis of stress in the canine diaphragm. *J. Appl. Physiol.* (1994) doi:10.1152/JAPPL.1994.76.5.2070.

107. Gao, Y., Waas, A. M., Faulkner, J. A., Kostrominova, T. Y. & Wineman, A. S. Micromechanical modeling of the epimysium of the skeletal muscles. *J. Biomech.* **41**, 1–10 (2008).
108. Eisenberg, B. R. & Mobley, B. A. Size changes in single muscle fibers during fixation and embedding. *Tissue Cell* **7**, 383–387 (1975).
109. Purslow, P. P. Strain-induced reorientation of an intramuscular connective tissue network: implications for passive muscle elasticity. *J. Biomech.* **22**, 21–31 (1989).
110. Gillies, A. R. *et al.* High resolution three-dimensional reconstruction of fibrotic skeletal muscle extracellular matrix. *J. Physiol.* **595**, 1159–1171 (2017).
111. Gao, Y., Kostrominova, T. Y., Faulkner, J. A. & Wineman, A. S. Age-related changes in the mechanical properties of the epimysium in skeletal muscles of rats. *J. Biomech.* **41**, 465–469 (2008).
112. Functional importance of a highly elastic ligament on the mammalian diaphragm. *Proc. R. Soc. Lond. B Biol. Sci.* **249**, 199–204 (1992).
113. Street, S. F. Lateral transmission of tension in frog myofibers: A myofibrillar network and transverse cytoskeletal connections are possible transmitters. *J. Cell. Physiol.* **114**, 346–364 (1983).
114. Ramaswamy, K. S. *et al.* Lateral transmission of force is impaired in skeletal muscles of dystrophic mice and very old rats. *J. Physiol.* **589**, 1195–1208 (2011).
115. Sharafi, B. & Blemker, S. S. A mathematical model of force transmission from intrafascicularly terminating muscle fibers. *J. Biomech.* **44**, 2031–2039 (2011).
116. Huijing, P. A. Muscle as a collagen fiber reinforced composite: a review of force transmission in muscle and whole limb. *J. Biomech.* **32**, 329–345 (1999).

117. Huijing, P., Baan, G. C. & Rebel, G. T. Non-myotendinous force transmission in rat extensor digitorum longus muscle. *J. Exp. Biol.* **201**, 683–691 (1998).

118. Maas, H., Baan, G. C. & Huijing, P. A. Intermuscular interaction via myofascial force transmission: effects of tibialis anterior and extensor hallucis longus length on force transmission from rat extensor digitorum longus muscle. *J. Biomech.* **34**, 927–940 (2001).

119. Boriek, A. M., Zhu, D., Zeller, M. & Rodarte, J. R. Inferences on force transmission from muscle fiber architecture of the canine diaphragm. *Am. J. Physiol.-Regul. Integr. Comp. Physiol.* **280**, R156–R165 (2001).

120. Stuelsatz, P., Keire, P., Almuly, R. & Yablonka-Reuveni, Z. A Contemporary Atlas of the Mouse Diaphragm. *J. Histochem. Cytochem.* **60**, 638–657 (2012).

121. Cardiomyopathy in DMD: Lisinopril vs. Losartan - Study Results - ClinicalTrials.gov. https://clinicaltrials.gov/ct2/show/results/NCT01982695.

122. Lee, E.-M. *et al.* Chronic effects of losartan on the muscles and the serologic profiles of mdx mice. *Life Sci.* **143**, 35–42 (2015).

123. Gillies, A. R. & Lieber, R. L. Structure and function of the skeletal muscle extracellular matrix. *Muscle Nerve* **44**, 318–331 (2011).

124. Huang, P. *et al.* Impaired respiratory function in mdx and mdx/utrn+/− mice. *Muscle Nerve* **43**, 263–267 (2011).

125. Brashear, S. E., Wohlgemuth, R. P., Gonzalez, G. & Smith, L. R. Passive stiffness of fibrotic skeletal muscle in mdx mice relates to collagen architecture. *J. Physiol.* **599**, 943–962 (2021).

126. Brashear, S. E. *et al.* Collagen cross-links scale with passive stiffness in dystrophic mouse muscles, but are not altered with administration of a lysyl oxidase inhibitor. *PLOS ONE* **17**, e0271776 (2022).
127. Sahani, R., Wallace, C. H., Jones, B. K. & Blemker, S. S. Diaphragm muscle fibrosis involves changes in collagen organization with mechanical implications in Duchenne muscular dystrophy. *J. Appl. Physiol.* **132**, 653–672 (2022).
128. Lamsfuss, J. & Bargmann, S. Computational modeling of damage in the hierarchical microstructure of skeletal muscles. *J. Mech. Behav. Biomed. Mater.* **134**, 105386 (2022).
129. Boriek, A. M., Miller, C. C. & Rodarte, J. R. Muscle fiber architecture of the dog diaphragm. *J. Appl. Physiol. Bethesda Md 1985* **84**, 318–326 (1998).
130. Ramesh Raghupathy,. Form from Function: Generalized Anisotropic Inverse Mechanics for Soft Tissues. (University of Minnesota, 2011).
131. Voigt, W. Ueber innere Reibung fester Körper, insbesondere der Metalle. *Ann. Phys.* **283**, 671–693 (1892).
132. Schneidereit, D. *et al.* Optical prediction of single muscle fiber force production using a combined biomechatronics and second harmonic generation imaging approach. *Light Sci. Appl.* **7**, 79 (2018).
133. Ateshian, G. A., Rajan, V., Chahine, N. O., Canal, C. E. & Hung, C. T. Modeling the Matrix of Articular Cartilage Using a Continuous Fiber Angular Distribution Predicts Many Observed Phenomena. *J. Biomech. Eng.* **131**, (2009).

134. Takaza, M., Moerman, K. M., Gindre, J., Lyons, G. & Simms, C. K. The anisotropic mechanical behaviour of passive skeletal muscle tissue subjected to large tensile strain. *J. Mech. Behav. Biomed. Mater.* **17**, 209–220 (2013).
135. Morrow, D. A., Haut Donahue, T. L., Odegard, G. M. & Kaufman, K. R. Transversely isotropic tensile material properties of skeletal muscle tissue. *J. Mech. Behav. Biomed. Mater.* **3**, 124–129 (2010).
136. Wheatley, B. B., Odegard, G. M., Kaufman, K. R. & Donahue, T. L. H. How does tissue preparation affect skeletal muscle transverse isotropy? *J. Biomech.* **49**, 3056–3060 (2016).
137. Wheatley, B. B. Investigating Passive Muscle Mechanics With Biaxial Stretch. *Front. Physiol.* **11**, (2020).
138. Reyna, W. E., Pichika, R., Ludvig, D. & Perreault, E. J. Efficiency of skeletal muscle decellularization methods and their effects on the extracellular matrix. *J. Biomech.* **110**, 109961 (2020).
139. Lee, E. J., Holmes, J. W. & Costa, K. D. Remodeling of Engineered Tissue Anisotropy in Response to Altered Loading Conditions. *Ann. Biomed. Eng.* **36**, 1322–1334 (2008).
140. Matsumoto, T. *et al.* Three-Dimensional Cell and Tissue Patterning in a Strained Fibrin Gel System. *PLOS ONE* **2**, e1211 (2007).
141. Pursell, E. R., Vélez-Rendón, D. & Valdez-Jasso, D. Biaxial Properties of the Left and Right Pulmonary Arteries in a Monocrotaline Rat Animal Model of Pulmonary Arterial Hypertension. *J. Biomech. Eng.* **138**, (2016).

142. Narice, B. F., Green, N. H., MacNeil, S. & Anumba, D. Second Harmonic Generation microscopy reveals collagen fibres are more organised in the cervix of postmenopausal women. *Reprod. Biol. Endocrinol. RBE* **14**, 70 (2016).
143. Provenzano, P. P., Eliceiri, K. W. & Keely, P. J. Multiphoton microscopy and fluorescence lifetime imaging microscopy (FLIM) to monitor metastasis and the tumor microenvironment. *Clin. Exp. Metastasis* **26**, 357–370 (2009).
144. Schenke-Layland, K. Non-invasive multiphoton imaging of extracellular matrix structures. *J. Biophotonics* **1**, 451–462 (2008).
145. Nieminen, H. J. *et al.* Determining collagen distribution in articular cartilage using contrast-enhanced micro-computed tomography. *Osteoarthritis Cartilage* **23**, 1613–1621 (2015).
146. Rittié, L. Method for Picrosirius Red-Polarization Detection of Collagen Fibers in Tissue Sections. in *Fibrosis: Methods and Protocols* (ed. Rittié, L.) 395–407 (Springer, 2017). doi:10.1007/978-1-4939-7113-8_26.
147. Greiner, C. *et al.* Robust quantitative assessment of collagen fibers with picrosirius red stain and linearly polarized light as demonstrated on atherosclerotic plaque samples. *PLOS ONE* **16**, e0248068 (2021).
148. Inouye, J., Handsfield, G. & Blemker, S. Fiber Tractography for Finite-Element Modeling of Transversely Isotropic Biological Tissues of Arbitrary Shape Using Computational Fluid Dynamics. 6.
149. Martin, K. S., Virgilio, K. M., Peirce, S. M. & Blemker, S. S. Computational Modeling of Muscle Regeneration and Adaptation to Advance Muscle Tissue Regeneration Strategies. *Cells Tissues Organs* **202**, 250–266 (2016).

150. Virgilio, K. M., Martin, K. S., Peirce, S. M. & Blemker, S. S. Agent-based model illustrates the role of the microenvironment in regeneration in healthy and mdx skeletal muscle. *J. Appl. Physiol.* **125**, 1424–1439 (2018).

151. Sleboda, D. A. & Roberts, T. J. Internal fluid pressure influences muscle contractile force. *Proc. Natl. Acad. Sci.* **117**, 1772–1778 (2020).

152. Bernabei, M., Lee, S. S. M., Perreault, E. J. & Sandercock, T. G. Shear wave velocity is sensitive to changes in muscle stiffness that occur independently from changes in force. *J. Appl. Physiol.* **128**, 8–16 (2020).

153. Cui, L., Perreault, E. J., Maas, H. & Sandercock, T. Modeling Short-Range Stiffness of Feline Lower Hindlimb Muscles. *J. Biomech.* **41**, 1945–1952 (2008).

154. Purslow, P. P. The Structure and Role of Intramuscular Connective Tissue in Muscle Function. *Front. Physiol.* **11**, 495 (2020).

155. Chapman, M. A., Mukund, K., Subramaniam, S., Brenner, D. & Lieber, R. L. Three distinct cell populations express extracellular matrix proteins and increase in number during skeletal muscle fibrosis. *Am. J. Physiol.-Cell Physiol.* **312**, C131–C143 (2017).

156. Liu, Y., Ballarini, R. & Eppell, S. J. Tension tests on mammalian collagen fibrils. *Interface Focus* **6**, (2016).

157. Yamamoto, N. Tensile Strength of Single Collagen Fibrils Isolated from Tendons. *Eur. J. Biophys.* **5**, 1 (2017).

158. Wenger, M. P. E., Bozec, L., Horton, M. A. & Mesquida, P. Mechanical Properties of Collagen Fibrils. *Biophys. J.* **93**, 1255–1263 (2007).

159. Ault, H. K. & Hoffman, A. H. A composite micromechanical model for connective tissues: Part II--Application to rat tail tendon and joint capsule. *J. Biomech. Eng.* **114**, 142–146 (1992).